

# Bachelorarbeit

aus der Physik

---

***Magnetic Resonance Spectroscopy at 7 T With and Without J-Difference Editing***

---

Johanna Link

Betreuende: Dr. Angelika Mennecke, Prof. Dr. Moritz Zaiss

---

Abgabedatum: 02. Oktober 2025

---

## **Abstract**

In this project, I investigated several  $^1\text{H}$ -magnetic resonance spectroscopy ( $^1\text{H}$ -MRS) measurement methods at 7 T, both in phantoms and in vivo, focusing on quantifying total N-acetylaspartic acid (tNAA), total creatine (tCr), and total choline (tCho), the key resonances in the human brain, and the harder-to-detect J-coupled metabolites  $\gamma$ -aminobutyric acid (GABA) and 2-hydroxyglutarate (2HG). At 7 T, the increased signal-to-noise ratio (SNR) and chemical shift dispersion enable improved spectral separation, at the cost of stronger field inhomogeneities, a higher specific absorption rate (SAR), and a larger chemical shift displacement error (CSDE). Because phantom relaxation and macro-molecular backgrounds were unknown, I used a simple peak model (two-step phase, smooth baseline, Voigt peaks) with measured longitudinal relaxation time ( $T_1$ ) and transverse relaxation time ( $T_2$ ) corrections. First, measurement and quantification methods were tested with Phantom studies; in vivo single voxel spectroscopy (SVS) gave realistic ratios comparable to literature values, with GABA detected through J-difference-editing, though overestimated. 2HG was visible in the phantom without editing but underestimated; chemical shift imaging (CSI) was SNR-limited. The simple model worked well for core metabolites. For edited or overlapping targets a basisset-based approach might give more exact quantification results.

# Contents

<b>1</b>	<b>Introduction</b>	<b>8</b>
<b>2</b>	<b>Theory</b>	<b>10</b>
2.1	Metabolites of Interest . . . . .	10
2.1.1	Total N-Acetylaspartic Acid . . . . .	10
2.1.2	Total Creatine . . . . .	11
2.1.3	Total Choline . . . . .	11
2.1.4	$\Gamma$ -Aminobutyric Acid . . . . .	12
2.1.5	2-Hydroxy-Glutarate . . . . .	13
2.2	Fundamentals of Nuclear Magnetic Resonance . . . . .	13
2.2.1	Nuclear Spin in a Magnetic Field . . . . .	13
2.2.2	Bloch Equations . . . . .	14
2.2.3	Scalar Coupling . . . . .	14
2.2.4	Free Induction Decay and Fourier Transformation . . . . .	15
2.2.5	Magnetic Resonance Imaging and Magnetic Resonance Spectroscopy . . . . .	15
2.2.6	Chemical Shift . . . . .	16
2.3	Relaxation . . . . .	16
2.3.1	Longitudinal Relaxation . . . . .	16
2.3.2	Ernst Angle . . . . .	17
2.3.3	Transverse Relaxation . . . . .	17
2.3.4	Relaxation in Phantoms . . . . .	18
2.4	Line Shape . . . . .	20
2.5	Radiofrequency Pulses . . . . .	21
2.5.1	Square Pulsesshape . . . . .	21
2.5.2	Frequency Selection . . . . .	22
2.5.3	Adiabatic Pulse Shape . . . . .	23
2.6	Single Volume Localization . . . . .	23
2.6.1	Chemical Shift Displacement . . . . .	24
2.6.2	PRESS . . . . .	24
2.6.3	LASER . . . . .	24
2.6.4	Semi-LASER . . . . .	25
2.7	Chemical Shift Imaging . . . . .	26
2.8	Water Suppression . . . . .	26
2.8.1	CHESS . . . . .	26
2.8.2	WET . . . . .	27
2.8.3	VAPOR . . . . .	27
2.8.4	Presaturation . . . . .	27

2.8.5 MEGA Suppression . . . . .	27
2.9 J-Difference Editing . . . . .	28
<b>3 Experimental Methods</b>	<b>30</b>
3.1 Phantom Construction . . . . .	30
3.1.1 Phantom 1 . . . . .	30
3.1.2 Phantom 2 – The GABA Phantom . . . . .	31
3.1.3 Phantom 3 – The 2HG Phantom . . . . .	31
3.2 Measurement Procedure . . . . .	32
3.3 Water Suppression . . . . .	32
3.4 Temperature Dependence of the Water Resonance Frequency . . . . .	33
<b>4 Data Processing</b>	<b>35</b>
4.1 Fitting Routine . . . . .	35
4.2 Baseline . . . . .	35
4.2.1 Chebychev-polynomial Baseline . . . . .	36
4.2.2 Cubic-spline Baseline . . . . .	36
4.3 Peak Modeling . . . . .	36
4.4 Phase Correction . . . . .	38
4.5 Parallelization . . . . .	39
4.6 T <sub>1</sub> Decay Correction . . . . .	39
4.7 T <sub>2</sub> Decay Correction . . . . .	39
4.8 Signal-to-Noise Ratio . . . . .	39
4.9 Quality of the Fit . . . . .	40
4.10 Comparison to LCModel . . . . .	40
<b>5 Measurements</b>	<b>42</b>
5.1 Estimation of the Chemical Shift Displacement Error in Field Direction . . . . .	42
5.2 Phantom Measurements . . . . .	45
5.2.1 Measurement Challenges in the 2HG Phantom . . . . .	45
5.2.2 Longitudinal Relaxation . . . . .	46
5.2.3 Transverse Relaxation . . . . .	48
5.2.4 SVS of NAA, Cr and Cho . . . . .	49
5.2.5 SVS J-Difference Editing of GABA . . . . .	50
5.2.6 SVS of 2HG . . . . .	52
5.3 In Vivo Measurements . . . . .	53
5.3.1 SVS of NAA, Cr and Cho . . . . .	53
5.3.2 J-Difference Editing of GABA . . . . .	55
5.3.3 CSI of NAA, Cr and Cho . . . . .	55
5.3.4 CSI of GABA . . . . .	57
<b>6 Conclusion and Outlook</b>	<b>58</b>
<b>List of Figures</b>	<b>62</b>
<b>List of Tables</b>	<b>63</b>
<b>A Individual Fits</b>	<b>67</b>
<b>Declaration of Tools Used</b>	<b>82</b>



# List of Abbreviations

**<sup>1</sup>H-MRS** <sup>1</sup>H-magnetic resonance spectroscopy. 1, 5–7, 9–11, 19, 24, 25

**2HG** 2-hydroxyglutarate. 1, 3, 5, 6, 8, 10, 11, 15, 16

**AFP** adiabatic full passage. 3, 5, 21, 23, 24

**BPP** Bloemberg - Percell - Pound. 5, 16

**CEST** chemical exchange saturation tranfer. 5

**CHESS** Chemical Shift Selective. 5, 24, 25

**Cho** choline. 5, 6, 9, 15

**Cr** creatine. 5, 6, 9

**Cr-CH<sub>2</sub>** the methylene creatine resonance at 3.93 ppm. 5, 25

**Cr-CH<sub>3</sub>** the methyl creatine resonance at 3.03 ppm. 5

**CRLB** Cramér-Rao Lower Bounds. 5

**CSDE** chemical shift displacement error. 1, 5, 19, 21–23

**CSI** chemical shift imaging. 1, 5, 24

**FID** free induction decay. 5, 13, 18, 24

**FOV** field of view. 5

**FWHM** full width half maximum. 5, 13, 18, 19

**GABA**  $\gamma$ -aminobutyric acid. 1, 5, 6, 8, 10, 11, 13, 15, 16, 26

**GM** grey matter. 5, 15

**GPC** glycerophosphorylcholine. 5, 9

**HWHM** half width half maximum. 5, 18

**IDH** isocitrate dehydrogenase. 5, 10

**LASER** Localization by Adiabatic Selective Refocusing. 3, 5, 22–24

**MEGA** Mescher-Garwood. 4, 5, 13, 26

**mPRESS** MEGA PRESS. 5, 25, 26

**MR** magnetic resonance. 5

**MRI** magnetic resonance imaging. 5, 8, 11, 13, 17

**MRS** magnetic resonance spectroscopy. 5–8, 11–14, 16, 19–21, 26

**MRSI** magnetic resonance spectroscopic imaging. 5, 24

**MSE** mean squared error. 5

**msLASER** MEGA semi-LASER. 5, 26

**NAA** N-acetylaspartic acid. 1, 5, 6, 8, 9, 11, 15, 16

**NAAG** N-acetylaspartyglutamate. 5, 9

**NMR** nuclear magnetic resonance. 5, 8, 11–14

**OVS** outer volume suppression. 5, 22

**PBS** phosphate-buffered saline. 5

**PC** phosphorylcholine. 5, 9

**pCr** phosphocreatine. 5, 9

**ppm** parts-per-million. 5, 14

**PRESS** point resolved spectroscopy. 4, 5, 13, 22–24, 27

**RF** radiofrequency. 3, 5, 12–14, 19–26

**RSMD** root mean squared deviation. 3, 5, 19

**SAR** specific absorption rate. 1, 5, 20, 22

**sLASER** semi-LASER. 4, 5, 27

**SLR** Shinnar-Le Roux. 5, 20

**SNR** signal-to-noise ratio. 1, 5, 6, 15, 16

**SVS** single voxel spectroscopy. 1, 5, 21, 24

**T<sub>1</sub>** longitudinal relaxation time. 1, 5, 7, 12, 14–17, 25, 26

**T<sub>2</sub>** transverse relaxation time. 1, 5, 7, 12, 13, 15–18

. 5

**tCho** total choline. 1, 5, 8, 9, 15, 16

**tCr** total creatine. 1, 5, 8, 9, 15, 16

**tCr-CH<sub>2</sub>** the methylene total creatine resonance at 3.93 ppm. 5, 9, 15, 16

**tCr-CH<sub>3</sub>** the methyl total creatine resonance at 3.03 ppm. 5, 9, 15, 16

**TE** echo time. 5, 6, 16, 18, 26

**TMS** tetramethylsilane. 5, 14

**TR** repetition time. 5, 14, 15, 25

**VAPOR** Variable Pulse Power and Optimal Relaxation Delays. 5, 25

**WET** Water Suppression Enhanced Through T<sub>1</sub> Effects. 5, 25

**WM** white matter. 5, 15

# Chapter 1

## Introduction

One of the most fundamental approaches in physics is the study of how radiation interacts with matter, a field known as spectroscopy. In many spectroscopic techniques, absorption or emission occurs when the radiation energy matches the difference between quantized energy levels. In magnetic resonance spectroscopy (MRS), this principle manifests as resonance between nuclear spins and radiofrequency fields. Among the many spectroscopic techniques, MRS stands out because it relies on nuclear magnetic rather than electric properties. This means that no tissue-damaging radiation is involved and heat deposition is minimized, which is why it can safely be applied *in vivo*. The technique exploits the magnetic properties of atomic nuclei: when placed in a strong external magnetic field, certain nuclei resonate at characteristic frequencies. These frequencies are influenced by the chemical environment, leading to chemical shifts that provide information about molecular structure and composition. [1, chap. 1]

The human brain is a complex biochemical system, and many neurological and psychiatric disorders are associated with subtle changes in its metabolism. Non-invasive methods to detect and quantify such changes are therefore of great clinical interest.  $^1\text{H}$ -magnetic resonance spectroscopy ( $^1\text{H}$ -MRS), which specifically targets the abundant  $^1\text{H}$  nuclei – consisting of a single proton in water and metabolites – is particularly important. The high natural abundance leads to strong signals and allows the reliable detection of a broad range of neurochemicals. This is why  $^1\text{H}$ -MRS has become a standard approach for *in vivo* spectroscopy of the human brain, which is the focus of this project. [1, chap. 2]

All measurements were performed at a field strength of 7 T. Compared to lower field strengths, 7 T offers higher resolution and improved signal-to-noise ratio (SNR). At the same time, however, it introduces stronger field inhomogeneities and shorter transverse relaxation times ( $T_2$ s), which make the measurements more challenging. [1, chap. 1]

The overall goal of this work was to explore the feasibility of MRS at 7 T for quantifying key brain metabolites. In particular, I aimed to measure the prominent singlet resonances of N-acetylaspartic acid (NAA), creatine (Cr), and choline (Cho) from conventional spectra, and the smaller, clinically relevant signals of  $\gamma$ -aminobutyric acid (GABA) and 2-hydroxyglutarate (2HG) using J-difference editing. The motivation for measuring 2HG was its established role as a biomarker in brain tumors. [1, chap. 2]

To achieve this goal, I first performed systematic phantom experiments. These allowed me to comprehensively test and calibrate acquisition and analysis methods under controlled conditions, and to optimize different sequence parameters before proceeding to *in vivo* measurements.

For quantification, I deliberately avoided a fully model-based approach (e.g., LCModel), where metabolite behavior in a given sequence is simulated to form basis sets for spectral fitting. Such methods can produce excellent results, but the unknown relaxation constants and molecular background in my phantoms would have limited their accuracy. [1, chap. 9]

Instead, I developed a simple peak-modeling approach, consisting of two-step phase correction on the complex spectrum, a smooth baseline, and individual Voigt peaks for each resonance. This design allowed me to explicitly control assumptions and later incorporate longitudinal relaxation time ( $T_1$ ) and  $T_2$  corrections once measured. A central aim in this project was therefore to test how far such a simple, well-constrained model could be taken at 7 T – both in phantoms and *in vivo* – in the crowded  $^1\text{H}$ -MRS spectrum of the human brain, and to evaluate its feasibility for detecting challenging metabolites such as GABA and 2HG.

In this report, I will start by introducing relevant properties of the metabolites I measured and the theoretical background of MRS in chapter 2. In chapter 3, I will focus on phantom construction and general experimental methods that were common to all measurements. Chapter 4 then presents the analysis methods used to quantify metabolites, and the detailed measurements along with a discussion of the results follow in chapter 5.

# Chapter 2

## Theory

This chapter provides the theoretical foundations. First, relevant properties of the metabolites I detected are discussed, followed by an overview of the fundamentals of nuclear magnetic resonance (NMR) relevant both to MRS and magnetic resonance imaging (MRI). After outlining the difference between the two fields, concrete techniques of MRS will be introduced.

### 2.1 Metabolites of Interest

I focused on a set of metabolites that are particularly relevant in the human brain and in the context of brain tumors. The metabolites I examined are total N-acetylaspartic acid (tNAA), total creatine (tCr), total choline (tCho), GABA, and 2HG. I chose these compounds because they serve as key markers of neuronal integrity, energy metabolism, membrane turnover, and neurotransmission, and thus provide valuable information both under healthy conditions and in pathological alterations such as tumors. Unless noted otherwise, notations and arguments are taken from de Graaf [1, chap. 2].

#### 2.1.1 Total N-Acetylaspartic Acid

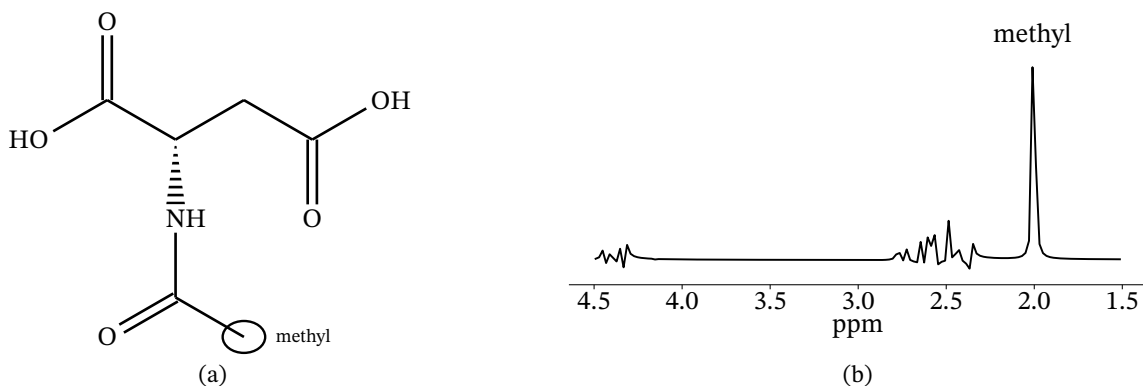


Figure 2.1: **NAA:** (a) Line-angle formula sketched with chemfig after de Graaf [1, chap. 2] with the methyl group causing the 2.01 ppm resonance circled and (b) simulated basisset at  $TE = 30$  ms by Landheer, Swanberg, and Juchem [2].

The most prominent resonance apart from water in healthy brain tissue originates from NAA ( $C_6H_9NO_5$ , molar mass 175.4 g/mol). In spite of this, the exact function of NAA remains a topic of discussion. As shown by Taylor et al. [3], NAA may act as an osmolyte, while D'Adamo and Yatsu [4] and D'Adamo and D'Adamo [5] proposed a role as an acetyl reservoir or transport intermediate for lipid synthesis. Blakely and Coyle [6]

provide a more detailed discussion, considering that NAA might play a metabolic role or be a precursor to N-acetylaspartylglutamate (NAAG).

In vivo, the resonance at 2.01 ppm represents the combined signal of NAA and its derivative NAAG and is therefore usually reported as tNAA. For simplicity, I will refer to this signal as NAA throughout, except in phantom experiments where only pure NAA is present.

A consistent finding is that its concentration varies with age and neuron type, with an expected concentration of 8 – 11 mM in white matter and 6 – 9 mM in gray matter. The NAA resonance can be used as a marker of neural density, as a lower intensity is observed in tissue affected by neuronal loss. Therefore, concentration is usually much lower (around 1.5 mM) in gliomas. Among many smaller resonances appearing as doublet or doublets, a very strong resonance at 2.01 ppm (see figure 2.1b) originates from the methyl group circled in figure 2.1a.

### 2.1.2 Total Creatine

tCr refers to the combination of Cr ( $C_4H_9N_3O_2$ , molar mass 131.1 g/mol) and phosphocreatine (pCr), whose resonances are nearly indistinguishable in  $^1H$ -MRS. Both Cr and pCr play a role in cellular energy metabolism. Figure 2.2 shows the line-angle formula of Cr and its resonances. pCr differs from Cr only by an N-phosphoryl group on the guanidino nitrogen; the backbone is otherwise identical.

Both molecules have two singlet resonances: the methyl creatine resonance at 3.03 ppm ( $Cr-CH_3$ ) and the methylene creatine resonance at 3.93 ppm ( $Cr-CH_2$ ). The resonances and the proton groups they originate from are shown in figure 2.2. The brain concentrations of tCr are relatively constant, with 4.0 – 5.5 mM for pCr and 4.5 – 6.0 mM for Cr. This makes it an ideal candidate for internal concentration referencing.

In vivo, the measured resonance is not uniquely attributable to either Cr or pCr, which is why I report ratios relative to tCr. In the phantoms, however, pCr was not included, so the reference is unambiguously Cr. For simplicity, I will refer to both as Cr.

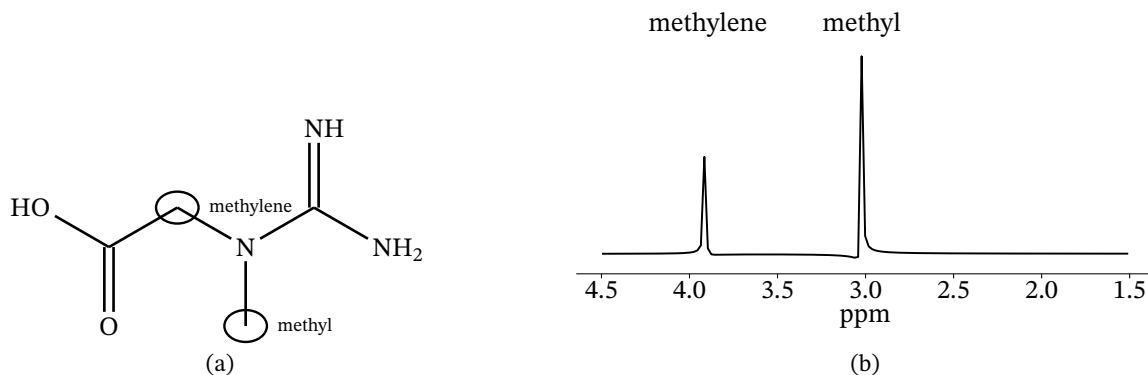


Figure 2.2: **Cr:** (a) Line-angle formula sketched with chemfig after de Graaf [1, chap. 2] with the methyl and methylene group causing the 3.03 ppm and 3.93 ppm resonances circled and (b) simulated basisset at  $TE = 30$  ms by Landheer, Swanberg, and Juchem [2].

### 2.1.3 Total Choline

tCho gives the third most prominent resonance in  $^1H$ -MRS in the brain after NAA and Cr. It is located at 3.2 ppm and arises from the three identical methyl groups marked in figure 2.3a with the resulting spectrum in figure 2.3b. The contributions come from free Cho, phosphorylcholine (PC) with an additional phosphoryl group at the terminal (primary-alcohol) oxygen, and glycerophosphorylcholine (GPC) with a glycerol moiety attached via a phosphodiester linkage.

In the human brain, free Cho is well below the  $^1H$ -MRS detection limit, so PC and GPC are the main contributors that cannot be separated based on the methyl protons. A tCho concentration of 1 – 2 mM is to be expected in

a non-uniform distribution. Choline-containing compounds are a marker of membrane turnover as they play a role in phospholipid synthesis and degradation. Therefore, an increase in the tCho concentration is expected in gliomas.

Free Cho ( $C_5H_{14}NO$ ), which is what I used in my phantoms, has a molar mass of 139.63 g/mol. In the following, I will refer to both tCho (in vivo) and pure Cho (in phantoms) as Cho for consistency.

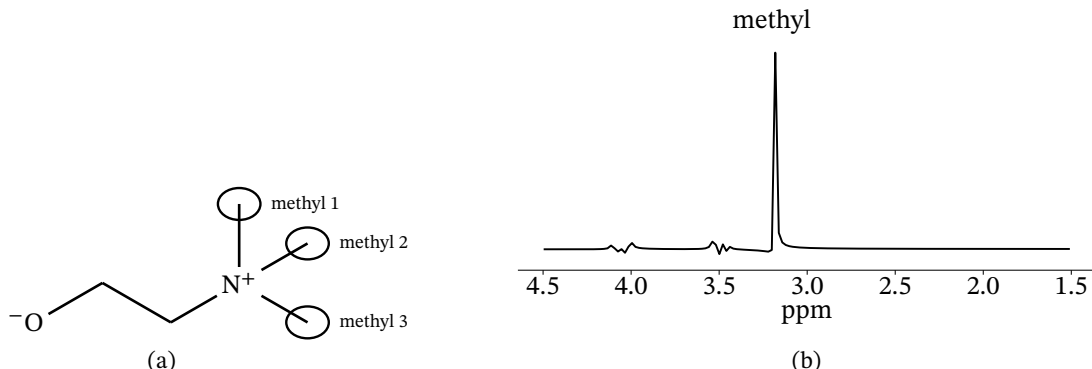


Figure 2.3: **Cho:** (a) Line-angle formula sketched with chemfig after de Graaf [1, chap. 2] with the three methyl groups causing the 3.2 ppm resonance circled and (b) simulated basisset at  $TE = 30$  ms by Landheer, Swanberg, and Juchem [2].

## 2.1.4 $\Gamma$ -Aminobutyric Acid

Another brain metabolite visible with  $^1H$ -MRS is GABA ( $C_4H_9NO_2$ , molar mass 103.12 g/mol), an inhibitory neurotransmitter. It has a brain concentration of approximately 1 mM that might vary due to the menstrual cycle, alcohol and substance abuse, psychiatric diseases, and other factors. This motivates the great number of scientific studies on the metabolite.

GABA has three methylene groups that give an observable  $^1H$ -MRS signal, forming an  $A_2MM'XX'$  spin system. This results in triplet resonances for GABA-H2 at 2.28 ppm and for GABA-H4 at 3.00 ppm and a quintet for GABA-H3 at 1.89 ppm, with all three resonances overlapping with other, stronger signals. Therefore, GABA is typically detected with spectral editing (see section 2.9). Figure 2.4 shows the line-angle formula of GABA with the  $^1H$ -MRS visible proton groups circled along with the resulting spectrum.

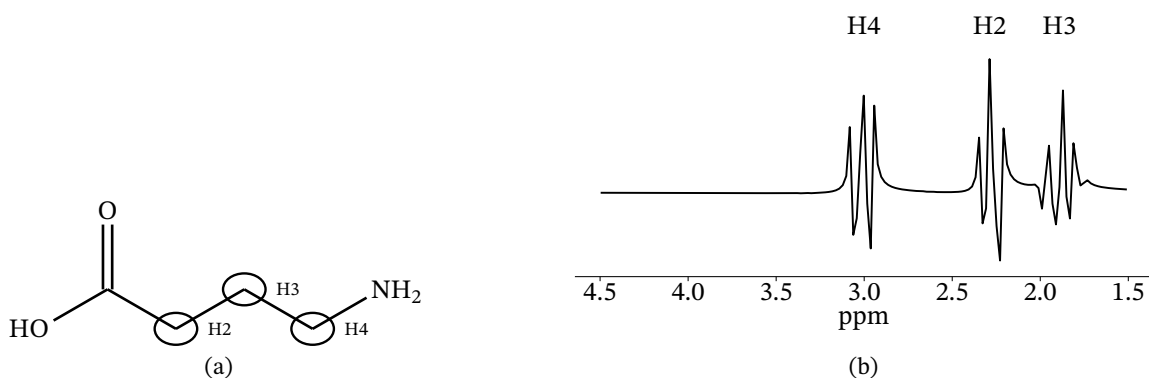


Figure 2.4: **GABA:** (a) Line-angle formula sketched with chemfig after de Graaf [1, chap. 2] with the three methylene groups causing the 2.28 ppm, 3.00 ppm and 1.89 ppm resonances circled and (b) simulated basisset at  $TE = 30$  ms by Landheer, Swanberg, and Juchem [2].

### 2.1.5 2-Hydroxy-Glutamate

An important marker in brain tumor classification is 2HG ( $C_5H_8O_5$ , molar mass 148.1 g/mol). In healthy brain tissue, its concentration is below the  $^1H$ -MRS detection limit, but in gliomas bearing a mutation in isocitrate dehydrogenase (IDH) 1 and 2, the D-isomer of 2HG can reach a concentration of up to 10 mM.

These mutations are associated with characteristic changes in tumor biology, prognosis and therapeutic response. Patients with IDH-mutated gliomas generally show a more favorable overall survival compared to those with wild-type tumors, and treatment strategies are increasingly guided by molecular classification.

In figure 2.5a, the three  $^1H$ -MRS relevant proton groups are marked and in figure 2.5b the corresponding spectrum is shown. They produce complex multiplet resonances at 4.01 ppm, 1.90 ppm and 2.25 ppm overlapping among others with resonances from NAA and GABA molecules.

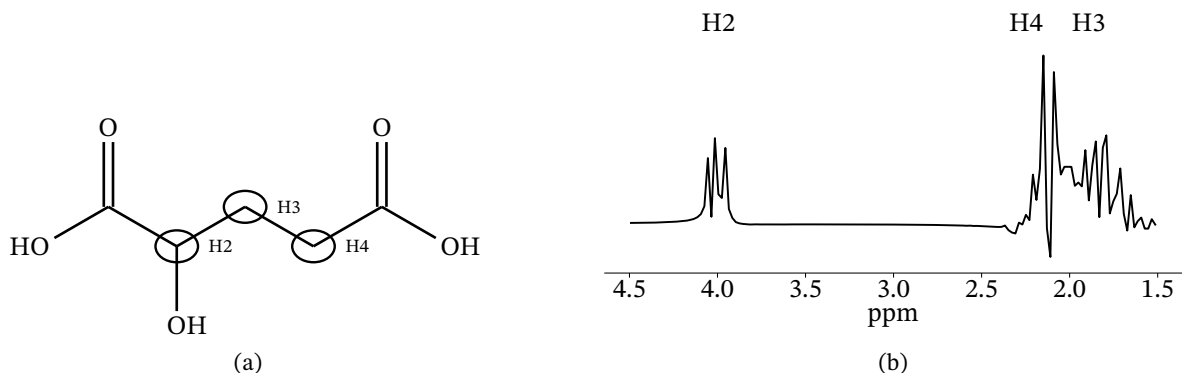


Figure 2.5: **2HG:** (a) Line-angle formula sketched with chemfig after de Graaf [1, chap. 2] with the three proton groups causing the 4.01 ppm, 1.90 ppm and 2.25 ppm resonances circled and (b) simulated basisset at  $TE = 30$  ms by Landheer, Swanberg, and Juchem [2].

## 2.2 Fundamentals of Nuclear Magnetic Resonance

NMR provides the physical basis for both MRI and MRS. In this section, I will introduce the basic principles of NMR relevant to MRS following de Graaf [1, chap. 1, 3 and 8].

### 2.2.1 Nuclear Spin in a Magnetic Field

Atomic nuclei are composed of protons and neutrons, which are quantum particles carrying intrinsic angular momentum, known as spin. This is a purely quantum mechanical property without a direct classical analogue, but it can be pictured as if the nucleus behaved like a tiny rotating electric charge, giving rise to its magnetic properties. Nuclei with a nonzero net spin quantum number  $I \neq 0$  possess the intrinsic magnetic moment

$$\mu = \gamma I, \quad (2.1)$$

where  $\gamma$  is the gyromagnetic ratio, a nucleus-specific constant describing the coupling strength to a magnetic field, and  $I$  denotes the spin. The hydrogen nucleus that I focused on has a gyromagnetic ratio of  $267.522 \text{ rad} \cdot \text{MHz}^{-1} \text{T}^{-1}$  and spin  $I = \frac{1}{2}$ . When placed in a static external magnetic field  $B_0$ , the nuclear magnetic moments interact with the field and experience a torque that leads to precession around the field axis and breaks the degeneracy of the two spin states  $+\frac{1}{2}$  and  $-\frac{1}{2}$ , leading to two distinct energy levels. This is known as the Zeeman effect. The energy difference between the levels is

$$\Delta E = \hbar \omega_0, \quad (2.2)$$

where  $\omega_0$  is the Larmor frequency describing the precession of the nuclear spins around the  $z$ -axis. It is given by

$$\omega_0 = \gamma B_0. \quad (2.3)$$

This frequency sets the resonance condition: only radiofrequency (RF) pulses that oscillate at  $\omega_0$  are able to induce transitions between the Zeeman levels and excite the spins. At thermal equilibrium, the populations of the two energy levels follow the Boltzman distribution.

Although the population difference is small (in the order of a few parts per million at clinical field strengths), it is sufficient to generate a measurable macroscopic magnetization vector  $M_0$  aligned along  $B_0$ . This net magnetization forms the basis of the detectable magnetic resonance signal.

## 2.2.2 Bloch Equations

The dynamics of macroscopic magnetization in a magnetic field  $B(t)$  can be described semi-classically with the Bloch equations. Not considering relaxation, the time evolution is governed by the torque equation

$$\frac{dM(t)}{dt} = \gamma M(t) \times B(t), \quad (2.4)$$

which expresses the precession of  $M(t)$  around  $B_0$  at the Larmor frequency.

$B = (B_x, B_y, B_z)$  consists of the static magnetic field  $B_z = B_0$  and the oscillatory magnetic field of a time-varying RF pulse with components  $B_x$  and  $B_y$ .

In practice, relaxation processes must also be considered. Longitudinal relaxation (characterized by the time constant  $T_1$ ) describes the return of  $M_z$  to its equilibrium value  $M_0$ , whereas transverse relaxation (characterized by  $T_2$ ) accounts for the decay of  $M_x$  and  $M_y$  due to dephasing of individual spins. Including both effects, the full Bloch equations are given by

$$\frac{dM_x}{dt} = \gamma (M \times B)_x - \frac{M_x}{T_2}, \quad (2.5)$$

$$\frac{dM_y}{dt} = \gamma (M \times B)_y - \frac{M_y}{T_2}, \quad (2.6)$$

$$\frac{dM_z}{dt} = \gamma (M \times B)_z - \frac{M_z - M_0}{T_1}. \quad (2.7)$$

These coupled differential equations provide a complete phenomenological description of the magnetization dynamics of homogeneous NMR experiments involving RF pulses and relaxation on a sample of non-interacting spins. However, effects that cannot be explained semi-classically are ignored. One such effect relevant in MRS is scalar coupling.

## 2.2.3 Scalar Coupling

Two nuclear spins are scalar coupled when the spin state of one influences the resonance frequency of the other. As a result, the single resonance appears as a multiplet in the spectrum. The interaction arises from an indirect coupling mechanism mediated by the bonding electrons between the nuclei.

It is a quantum phenomenon that cannot be described in the semi-classical picture of the Bloch equations. Due to the influence of its coupling partner, a J-coupled spin does not precess at a single frequency but instead oscillates between slightly shifted frequencies, leading to the appearance of multiplets. For a simple two-spin system with coupling constant  $J$ , the transverse magnetization evolves as

$$M_{xy}(t) \propto \cos(\pi J t), \quad (2.8)$$

inverting the signal periodically with a period of  $1/J$ .

This interaction is actually much weaker than dipolar interaction. However, due to rapid molecular tumbling, the spatial averaging of dipolar interactions reduces their net effect on the spectral frequency to zero, while scalar coupling gives a non zero net contribution.

This is exploited in J-difference editing (see section 2.9) by applying frequency-selective editing pulses that either suppress the J-modulation or leave it unaffected. Subtraction of the resulting spectra cancels uncoupled resonances while retaining the isolated coupled metabolite signal.

The echo time is chosen such that the J-modulation is at a maximum difference ( $TE \approx (2J)^{-1}$ ), which ensures efficient editing contrast for the metabolite of interest.

However, as J-modulation is only partly refocused by the frequency-selective refocusing pulses, the detectable concentration is inherently limited. Harris et al. [7] states that for example in Mescher-Garwood (MEGA)-point resolved spectroscopy (PRESS), the detectable GABA signal is reduced to roughly 50% of the real concentration.

## 2.2.4 Free Induction Decay and Fourier Transformation

The frequency required to excite the nuclear spin states is in the RF range. When an RF excitation pulse is applied, the net magnetization is tipped into the transverse plane. The precessing transverse magnetization induces a voltage in the receive coil. As the spins relax into their equilibrium position, the oscillating signal decays, producing the free induction decay (FID).

Considering only one Larmor frequency  $\omega_0$ , the FID is a complex function described by

$$M(t) = M_0 e^{i\omega_0 t + \phi} e^{-t/T_2}, \quad (2.9)$$

where  $\phi$  denotes the phase of the transverse magnetization with respect to the x-axis and  $T_2$  accounts for dephasing of the spins in the transverse plane due to spin-spin interaction. In the presence of multiple metabolites, the FID is a superposition of oscillations at different frequencies and amplitudes.

The fast Larmor oscillation is removed by the scanner electronics, so the stored FID no longer contains the carrier frequency. The resulting FID can then be separated into its different spectral components with a Fourier transformation:

$$F(\nu) = \int_{-\infty}^{\infty} f(t) e^{-2i\pi\nu t} dt, \quad (2.10)$$

for a given time-domain signal  $f(t)$ , in this case given by equation (2.9), with the carrier frequency removed. This yields a Lorentzian peak for each metabolite, the full width half maximum (FWHM) of which is determined by  $T_2$  dephasing. This is again a complex function, consisting of the absorption and dispersion spectrum. When the phase  $\phi$  disappears, the real spectrum becomes the pure absorption spectrum. As the dispersive component is responsible for broad tails that complicate quantification, this phase is commonly removed with a zero-order phase correction.

What makes NMR powerful as a spectroscopic tool is the direct proportionality between  $M_0$  and the number of excited spins. Under ideal circumstances,  $M_0$  can be calculated from the absorption spectrum as the area under the curve for each peak.

## 2.2.5 Magnetic Resonance Imaging and Magnetic Resonance Spectroscopy

Thus far, the discussion concerns both MRS and MRI. They are based on the same physical principles of NMR and both use the FID as a starting point. However, they differ in processing and interpretation of the signal.

In MRI, spatial encoding gradients are applied during and after excitation to encode position into the frequency and phase of the detected signal. Fourier transformation then yields an image of spin density distribution in space. The main focus of MRI is anatomical and functional imaging, with contrast mechanisms based on relaxation times, proton density and flow effects.

In MRS, the subject of this work, the emphasis is not on spatial encoding but rather the spectral content of the FID. The aim is to resolve small frequency differences that identify metabolites. The key to this specificity is the chemical shift.

### 2.2.6 Chemical Shift

Chemical shift arises because surrounding electrons partially shield the nucleus, altering the local magnetic field and shifting its Larmor frequency. Consequently, the exact resonance frequency depends on the chemical environment, enabling distinction among resonating proton groups, both within the molecule and across different molecules.

As the Larmor frequency depends on the external magnetic field, it is convenient to express the chemical shift not in terms of Hz but in parts-per-million (ppm) relative to a referencing compound with Larmor frequency  $\nu_{ref}$ . A chemical shift difference of 1 ppm corresponds to the center frequency (approximately 298 MHz at 7 T) divided by  $10^6$ .

Due to its strong singlet resonance largely independent of external factors, tetramethylsilane (TMS) is a popular reference, and therefore defines the origin of the ppm scale. The chemical shift is then given by

$$\delta = \frac{\nu - \nu_{tms}}{\nu_{tms}} \times 10^6. \quad (2.11)$$

With this definition, the water resonance is at 4.7 ppm at body temperature. Unfortunately, TMS is often an unsuitable reference as it is not present in vivo. In practice, the scanner therefore chooses water as a reference and encodes all other resonance frequencies with respect to water at 0 Hz. The ppm scale is thus offset by the chemical shift of water, which has to be added back to give the true chemical shift scale. The chemical shift axis is thus calculated from the frequency axis as follows:

$$\delta = \delta_{H_2O} - \frac{\nu}{\nu_{center}} \times 10^6. \quad (2.12)$$

The disadvantage of this method is the strong dependence of the water resonance frequency on temperature. This causes an apparent shift of other metabolites to lower ppm values when the temperature is below body temperature, where standard MRS values are recorded. While the chemical shift scale increases with frequency, it is conventional to invert the axis to go from higher values on the left to lower values on the right. This is a historic artifact from when NMR was recorded by sweeping the magnetic field at fixed RF frequency.

## 2.3 Relaxation

After an RF pulse tips the net magnetization vector away from its equilibrium, the spin system does not remain in this unperturbed state. Instead, it returns to its thermal equilibrium through processes collectively referred to as relaxation. Essentially, there are two processes to be considered: the recovery of longitudinal magnetization along the external field and the loss of coherence of transverse magnetization in the plane perpendicular to it. Throughout this section, I follow de Graaf [1, chap. 1, chap. 3], unless indicated otherwise.

### 2.3.1 Longitudinal Relaxation

After the excitation through an RF pulse with a flip angle  $\alpha$ , the net magnetization vector is flipped into the xy-plane where it rotates. In time, the protons transfer their energy to the surroundings and the magnetization recovers along the z-axis. The recovery of the longitudinal magnetization follows an exponential function that can be derived from the Bloch equations:

$$M_z(\alpha, TR) = M_0 \frac{1 - e^{-TR/T_1}}{1 - \cos \alpha e^{-TR/T_1}}, \quad (2.13)$$

governed by  $T_1$ , with the longitudinal magnetization  $M_z$ , the flip angle  $\alpha$ , and the equilibrium magnetization  $M_0$ . If the repetition time (TR) is below 3 – 5 times  $T_1$ , the longitudinal magnetization does not fully recover before the next excitation. This is particularly relevant in MRS, as  $T_1$  relaxation times are metabolite-specific. To avoid quantification errors through  $T_1$  decay, either TR must be chosen sufficiently long to minimize  $T_1$  weighting, or post-processing corrections must be applied to account for incomplete recovery.

The  $T_1$  relaxation times in vivo at 7 T of the metabolites I measured are listed in table 2.1. For NAA, Cr and Cho, the in vivo measurements in white matter (WM) and grey matter (GM) were taken from Xin et al. [8]. Due to the challenging SNR and editing loss (see subsection 2.1.4), the longitudinal relaxation times of GABA and 2HG have not yet been reliably determined at 7 T. For GABA,  $T_1$  can be inferred from the result at 3 T: According to Li et al. [9], in vivo metabolite  $T_1$  values increase by roughly 20 – 30% when going from 3 T to 7 T (e.g., Cr +25%, NAA +31%, Cho +17%) in human brain white matter. With  $T_1 = 1.31 \pm 0.16$  s [10] measured at 3 T, I assume a longitudinal relaxation of  $1.63 \pm 0.2$  s for in vivo measurements. For 2HG, I adopted the common proxy approach using glutamate to approximate the relaxation behavior of 2HG, as the two are similar in size, motional regime, and coupling behavior.

Table 2.1:  **$T_1$  in vivo relaxation times:** Literature values at 7 T in occipital WM and GM.

Metabolite	WM (s)	GM (s)	Ref
Water	$1.55 \pm 0.07$	$2.00 \pm 0.12$	[8]
NAA	$1.90 \pm 0.06$	$1.83 \pm 0.05$	[8]
Cr-CH <sub>3</sub>	$1.78 \pm 0.04$	$1.74 \pm 0.06$	[8]
Cr-CH <sub>2</sub>	$1.10 \pm 0.06$	$1.13 \pm 0.04$	[8]
Cho	$1.32 \pm 0.06$	$1.51 \pm 0.11$	[8]
GABA*	$1.63 \pm 0.2$	-	[10]
2HG†	$1.75 \pm 0.04$	$1.61 \pm 0.09$	[8]

\* 7T estimate derived from the 3 T value  $1.31 \pm 0.16$  ([10]), assuming a ~20–30% increase; no distinction between brain regions; source given for the 3 T value.

† Assumed similar to glutamate due to size, motional regime, and heavily J-coupled methylene/methyl protons; source given for the glutamate value.

### 2.3.2 Ernst Angle

Due to time constraints, it is not always possible to choose TR long enough for a full recovery. In that case, the flip angle should be adjusted for maximal signal intensity. The optimal flip angle for a given TR and  $T_1$  is the angle for which the steady-state transverse magnetization is maximal, so

$$\frac{dM_{xy}}{d\alpha}(\alpha, TR) = 0. \quad (2.14)$$

In the steady state, the transverse relaxation is given by  $M_{xy}(\alpha, TR) = M_z(\alpha, TR) \cdot \sin \alpha$ . Using equation (2.13), this gives:

$$\frac{\partial M_{xy}}{\partial \alpha} = M_0 \frac{(1 - e^{-TR/T_1}) (\cos \alpha - e^{-TR/T_1})}{(1 - e^{-TR/T_1} \cos \alpha)^2}, \quad (2.15)$$

which disappears for

$$\alpha_E = \arccos e^{-TR/T_1}. \quad (2.16)$$

### 2.3.3 Transverse Relaxation

In addition to  $T_1$  recovery, another relaxation process must be considered: the decay of transverse magnetization, known as  $T_2$  relaxation. This process reflects the loss of phase coherence among spins in the x-y-plane due to spin-spin interactions. Unlike  $T_1$ , which involves energy exchange with the surroundings,  $T_2$  relaxation results

from interaction between the spins themselves and does not involve net energy loss from the system. The decay function is given by

$$M_{xy}(t) = M_{xy}(0) \cdot e^{-t/T_2} \quad (2.17)$$

In practice, there is an additional decay component due to macroscopic magnetic field inhomogeneities. This decay is complex but often modeled by an exponential function, resulting in an effective relaxation time  $T_2^*$ , which is shorter than the intrinsic  $T_2$ :

$$\frac{1}{T_2^*} = \frac{1}{T_2} + \frac{1}{T_{inhom}} \quad (2.18)$$

In order to eliminate  $T_2^*$  effects, spin-echo based sequences are used in MRS. Here, refocusing pulses are applied to rephase the spins, giving rise to a spin echo the maximum of which occurs at the echo center. When the signal is sampled at this maximum, only  $T_2$  decay has to be considered.

Choosing the optimal echo time (TE) can improve SNR significantly and several factors have to be considered: On the one hand, long TE causes greater signal loss due to  $T_2$  decay. This decay is metabolite-specific, meaning that metabolites with shorter  $T_2$  values will lose signal more rapidly.

On the other hand, this effect also leads to a cleaner baseline for longer TE, since macro-molecules and lipids generally have short  $T_2$ s and decay quickly. To obtain accurate metabolite concentrations, I therefore chose an intermediate TE and performed  $T_2$  correction in post-processing.

For the transverse relaxation times of NAA, Cr, Cho and GABA at 7T in vivo, reliable measurement values have been established (see table 2.2). However, as with  $T_1$ , I could find no source for the transverse relaxation time of 2HG. Following the approach in subsection 2.3.1 for the longitudinal relaxation time, I therefore assume the transverse relaxation time of 2HG to be similar to glutamate.

Table 2.2:  **$T_2$  relaxation times at:** Literature values in the occipital lobe and motor cortex at 7 T.

Metabolite	Occipital Lobe (ms)	Motor Cortex (ms)	Ref
Water	$47.1 \pm 6$	$47.1 \pm 6$	[11]
NAA	$132 \pm 6$	$168 \pm 6$	[11]
Cr-CH <sub>2</sub>	$84 \pm 4$	$108 \pm 5$	[11]
Cr-CH <sub>3</sub>	$95 \pm 3$	$113 \pm 2$	[11]
Cho	$152 \pm 3$	$139 \pm 9$	[11]
GABA	$63 \pm 19^*$	-	[12]
2HG <sup>†</sup>	$93 \pm 4$	$98 \pm 4$	[11]

\* No distinction between brain regions

<sup>†</sup> Assumed similar to glutamate as with  $T_1$  due to similar size, motional regime, and heavily J-coupled methylene/methyl protons; source given for glutamate.

### 2.3.4 Relaxation in Phantoms

While many studies have been carried out to quantify relaxation times of water and metabolites in vivo, there is a lack of sources for liquid water-based phantoms. Unfortunately, several factors cause the decay constants to differ considerably from those observed in vivo.

Relaxation is mainly governed by rotational dynamics, a relation described by the Bloemberg - Percell - Pound (BPP) theory [13]. According to this model,  $T_1$  is shortest when the molecular tumbling rate is close to the Larmor frequency. Faster or slower tumbling causes the interaction with the lattice to be less efficient.  $T_2$  progressively increases with the molecular tumbling rate. The tumbling rate is influenced by several factors that will be discussed in the following. In vivo, this simple picture is complicated by restricted motion and interactions, leading to additional effects. These have to be considered when starting from well-known in vivo values and working back toward the simpler behavior in phantoms.

**Temperature** On the one hand, my phantom is measured at room temperature or cooled after storage in the fridge at  $4 - 6^\circ\text{C}$ . Lower temperature slows molecular tumbling. In vivo, the small molecules I measured and water are in the fast motion regime, where the tumbling frequency is higher than the Larmor frequency. This shortens both  $T_1$  and  $T_2$  of water relative to a  $37^\circ\text{C}$  sample; at sufficiently low temperature,  $T_1$  increases again. According to the BPP model, this minimum of  $T_1$  is reached when the molecular correlation satisfies  $\omega_0\tau_c \approx 1$ . At 7 T, this corresponds to a correlation time of  $\tau_c \approx 5 \times 10^{-10} \text{ s}$ . Based on Qvist et al. [14], such a slow tumbling rate can only be reached in the super-cooled regime (approximately  $-50^\circ\text{C}$  at 1 bar), which is not experimentally accessible as water cannot stay liquid at that temperature and pressure. This shows that in our temperature range, the system remains in the fast-motion regime.

This effect is strongest for water and decreases with molecule size.

**Magnetization Transfer** On the other hand, while in my liquid phantom water molecules move freely, the behavior in vivo is better described with a two-pool picture [15]: one pool consists of free water protons that generate the conventional magnetic resonance (MR) signal, whereas the other comprises restricted protons that are bound to proteins and other macromolecules. Free water molecules rotate rapidly and have very long  $T_1$ s and  $T_2$ s, while bound molecules have relaxation times that are so short they do not directly contribute to the MR signal. However, they are linked to free protons through magnetization transfer, which lowers the apparent  $T_1$  and  $T_2$  of free water protons in vivo. This second, stronger effect leads to an increase in water  $T_1$  and  $T_2$  in my phantoms compared to in vivo. Other metabolites in vivo are restricted to specific cellular compartments, which also leads to a similar exchange between multiple pools, which increases the apparent  $T_1$  and  $T_2$  in my phantoms compared to in vivo.

**Susceptibility Gradients** Another effect that mainly affects  $T_2$  is susceptibility gradients induced by microstructures in vivo. As water molecules diffuse through these gradients, they accumulate random phase shifts, accelerating dephasing and thereby shortening  $T_2$ . This further increases the apparent water  $T_2$  in my phantoms compared to in vivo. The effect of susceptibility gradients is again expected to be strongest for water and to decrease with metabolite size.

**Molecular Crowding** Specific to metabolites other than water is molecular crowding. In vivo, metabolites diffuse in a dense cytosolic environment full of proteins, lipids, and nucleic acids. Transient binding and dipolar coupling with these macromolecules strongly shorten  $T_2$  (especially  $T_2^*$ ) and moderately shorten  $T_1$ . Again, this increases both  $T_1$  and  $T_2$  in my phantoms compared to established in vivo values. [16]

**Relaxation Agents** Additionally, there exist several relaxation agents that reduce the relaxation time in phantoms compared to pure water. In my third phantom, I added 0.1 mM copper sulfate ( $\text{CuSO}_4$ ) to prevent microbial growth (see subsection 3.1.3), which also acts as a paramagnetic relaxation agent. Due to the low concentration, the effect is of course weak.

How efficiently a paramagnetic agent accelerates relaxation is quantified by the relaxivity. According to Thangavel and Saritas [17], the longitudinal relaxivity of copper sulfate is  $0.602 \text{ mM}^{-1}\text{s}^{-1}$  and the transverse relaxivity  $0.73 \text{ mM}^{-1}\text{s}^{-1}$  at 3 T, which means that it shortens the  $T_2$  of nearby water molecules by an additional 10 – 15 % (depending on  $T_1$  and  $T_2$  prior to the addition of copper sulfate).

While the effect of copper sulfate at 7 T has not been quantified yet, it stands to reason that the  $T_1$  relaxation time will be less efficiently shortened while the  $T_2$  relaxivity will be stronger, as is the case for gadolinium-based shortening agents [18].

The relaxation agent also impacts the relaxation times of other metabolites, albeit with a weaker effect, unless the metabolite can bind ions.

**Expectation** With all of these effects, I expect the relaxation times in my phantoms to be longer than in vivo, with water more strongly affected than other metabolites. However, this general behavior might differ considerably between molecules, depending on its interaction with the environment. To improve the accuracy of quantification, it is therefore necessary to determine the relaxation times in my phantoms experimentally.

## 2.4 Line Shape

The transverse relaxation also determines the line shape of the peaks in the spectrum. In the ideal limit of an undamped signal ( $T_2^* \rightarrow \infty$ ), Fourier transformation of each metabolite signal would yield a delta function at the resonance frequency. In practice, the FID decays and the spectrum acquires finite width [16, 19]. In spin-echo-localized spectroscopy, static dephasing ( $T_{inhom}$ ) is refocused up to TE, so the echo amplitude is primarily  $T_2$ -weighted. In a perfectly homogeneous field, this yields an absorption line that is well described by a Lorentzian,

$$L_\gamma(x) = \frac{\gamma^2}{\gamma^2 + x^2}, \quad (2.19)$$

where  $\gamma > 0$  is the half width half maximum (HWHM) so that the Lorentzian FWHM is  $w_L = 2\gamma$  [20].

For a purely homogeneous decay, the linewidth is proportional to  $1/(\pi T_2)$ .

During acquisition, however, the signal is again subject to  $B_0$  inhomogeneity. Therefore, the linewidth and lineshape are governed by an effective  $T_2^*$  during readout. This additional inhomogeneous broadening is better described by a Gaussian component.

A Gaussian is defined as

$$G_\sigma(x) = \exp\left(-\ln(2) \cdot \frac{x^2}{\sigma^2}\right), \quad (2.20)$$

where  $\sigma$  is the HWHM, giving  $w_G = 2\sigma$  as the FWHM [20].

To account for both homogeneous ( $T_2$ ) and inhomogeneous ( $B_0$ ) broadening, I used a Voigt profile, i.e. the convolution of a Lorentzian and a Gaussian

$$V_{\sigma,\gamma}(x) = (G_\sigma \circledast L_\gamma) = \int_{-\infty}^{\infty} G_\sigma(y) \cdot L_\gamma(x - y) dy, \quad (2.21)$$

where  $\circledast$  denotes the convolution [20].

In python, `scipy.special.wofz` provides a convenient implementation.

The Voigt profile reduces to a Lorentzian for  $\sigma = 0$  and to a Gaussian for  $\gamma = 0$ . This is illustrated in figure 4.1. Because the Voigt profile has no elementary closed form, its FWHM is commonly approximated from  $w_L$  and  $w_G$ , for example with the modified Whiting approximation described in Olivero and Longbothum [21]:

$$w_V = \frac{1}{2} \left[ 1.0692 \cdot (w_L + w_G) + \sqrt{0.86693 \cdot (w_L + w_G)^2 + 4 \cdot w_L \cdot w_G} \right] \quad (2.22)$$

with a relative error below 0.02%.

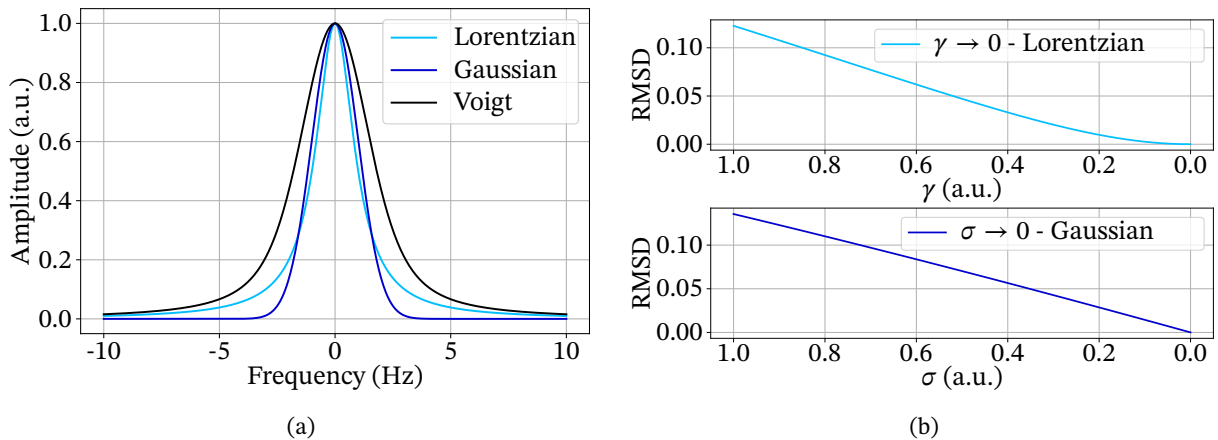


Figure 2.6: **Voigt profile:** (a) Comparison of Gaussian, Lorentzian and Voigt profiles with normalized amplitude,  $\sigma = 1$  and  $\gamma = 1$ ; (b) Convergence of the Voigt Profile to a Lorentzian for  $\sigma \rightarrow 0$  and Gaussian for  $\gamma \rightarrow 0$ ; quantified by the root mean squared deviation (RSMD), calculated as  $RSMD = \sqrt{\frac{1}{N} \sum_{i=1}^N (f_i - g_i)^2}$ , where  $f_i$  and  $g_i$  are the sampled values of the two functions at  $N$  points.

## 2.5 Radiofrequency Pulses

Spin manipulations such as excitation and refocusing are achieved using RF pulses. This refers to a magnetic field rotating at the spin Larmor frequency, which, for  $^1\text{H}$ -MRS, falls in the radiofrequency range of the electromagnetic spectrum. The coils are designed in such a way that the electric component in the near field is minimized and a mainly magnetic field is generated.

When the frequency of the RF pulse coincides with the Larmor frequency of the spins, the pulse is considered to be on-resonance. In MRS, different metabolites resonate at distinct frequencies. As a result, an RF pulse can only be on-resonance for exactly one chosen frequency, while other spins will be off-resonance to some extent. RF pulses can be characterized by the product of bandwidth and pulse duration, the R-value, which is constant for a given RF pulse and nutation angle. The bandwidth corresponds to the FWHM of the pulse. In order to reduce the chemical shift displacement error (CSDE), one should choose a pulse with a high R-value, which will be explained in subsection 2.6.1. The explanation in this section follows de Graaf [1, chap. 5].

### 2.5.1 Square Pulsesshape

The most basic RF pulse is a pulse with a square envelope that is achieved by turning on the current in the RF coil, keeping it on at constant amplitude for a certain duration  $\tau$  and turning it off again. This excites all spins simultaneously, without spatial or frequency selectivity. In the on-resonance case, a square pulse with amplitude  $B_1$  and duration  $\tau$  produces a nutation by the angle

$$\Theta = \gamma B_1 \tau, \quad (2.23)$$

where  $\gamma$  is the gyromagnetic ratio.

An excitation pulse is a  $90^\circ$  RF pulse that completely rotates the longitudinal magnetization  $M_z$  in the transverse plane ( $M_{xy}$ ). An inversion pulse rotates the longitudinal magnetization by  $180^\circ$  from  $M_z$  to  $-M_z$ . For this, the area needs to be doubled, which can be realized by increasing either the duration  $\tau$  or the amplitude  $B_1$ . A special case of the inversion pulse is the refocusing pulse, which rotates the magnetization by  $180^\circ$  within the transverse plane ( $M_{xy}$ ).

The effective magnetic field  $B_e$  for off-resonance spins whose Larmor frequency differs from the carrier frequency

by  $\Delta\nu$  has the amplitude

$$B_e = \sqrt{B_1^2 + \left(\frac{2\pi\Delta\nu}{\gamma}\right)^2} \quad (2.24)$$

and direction

$$\alpha = \arctan\left(\frac{2\pi\Delta\nu}{\gamma}\right). \quad (2.25)$$

Off-resonance excitation reduces the efficiency of transverse magnetization and introduces a phase shift that scales with the frequency offset  $\Delta\nu$ . This linear phase shift can be compensated during post-processing by applying a first-order phase correction.

To achieve non-selective rotations across a broader frequency range, pulses should be kept as short as possible. Shortening the pulse, however, requires a higher  $B_1$  amplitude, which increases RF power deposition in tissue. The underlying cause is that the electric field cannot be completely eliminated and increases with the magnetic field amplitude. This electric field induces currents in conductive samples such as the human body. The corresponding power deposition is given by

$$P = \frac{1}{2} \int_V \sigma |E|^2 dV, \quad (2.26)$$

where  $\sigma$  denotes the tissue conductivity and  $V$  the sample volume. The rate at which RF energy is absorbed by tissue during an MRS experiment is quantified by the specific absorption rate (SAR).

From equation (2.26), it follows that the SAR scales with the square of the residual electric field, which in turn increases approximately with the square of the RF amplitude. In addition, SAR depends on pulse duration, repetition rate, and patient properties such as body weight and tissue composition.

For safety, scanners continuously monitor SAR and limit the maximum RF amplitude or duty cycle, thereby limiting the maximum achievable bandwidth for a given pulse shape and measurement [1, chap. 10].

The optimal choice for a required peak amplitude and power is therefore the square pulse, which does not have good spatial localization. This makes improved selectivity a trade-off against amplitude and power efficiency.

## 2.5.2 Frequency Selection

In principle, frequency selection can be achieved by increasing the pulse duration of a square RF pulse. However, the Fourier transform of a square envelope is a sinc, which leads to the unintended excitation of off-resonance spins.

For reliable frequency selection, a pulse shape with a well-defined, selective frequency profile is required. A natural candidate is the sinc function, whose Fourier transform is a rectangular frequency response. Since the theoretical sinc extends infinitely across the real axis, it must be truncated in practice, which introduces side lobes in the frequency profile.

This drawback does not occur with Gaussian pulses, which transform into another Gaussian in the frequency domain. Gaussian pulses are therefore commonly chosen for applications such as spectral editing and water suppression, as they combine relatively good frequency selectivity with relatively low R-values.

While basic pulse shapes such as square, sinc, and Gaussian remain widely used, they are limited in terms of frequency selectivity and bandwidth per unit power. A more flexible approach is provided by numerical optimization methods based on the Bloch equations. One such solution is the Shinnar-Le Roux (SLR) algorithm, which reformulates RF pulse design in terms of digital filter theory. SLR pulses can be constructed as linear-phase or minimum-phase profiles. The linear phase roll of the linear SLR pulses can be corrected during post-processing, while minimum-phase SLR pulses shift excitation towards the end of the pulse, reducing phase roll and minimizing echo times.

### 2.5.3 Adiabatic Pulse Shape

As mentioned in subsection 2.5.1, it is desirable to choose a pulse with higher bandwidth to achieve excitation over a broader frequency range, as this reduces the CSDE (see subsection 2.6.1). However, shortening the pulse requires increasing the amplitude, which is limited for safety reasons. Additionally, conventional amplitude-modulated pulses are sensitive to  $B_1$  inhomogeneities and frequency offsets.

These problems are addressed by adiabatic RF pulses, which, in addition to amplitude modulation employ frequency – and sometimes phase – modulation such that the magnetization vector follows the effective field throughout the pulse. This requires the fulfillment of the adiabatic condition

$$\left| \frac{d\alpha(t)}{\gamma dt} \right| \ll |B_e(t)|, \quad (2.27)$$

where  $\alpha(t)$  is the angle of the effective field and  $B_e(t)$  is its magnitude. With this condition satisfied, adiabatic pulses produce a uniform spin rotation that is largely insensitive to  $B_1$  inhomogeneities.

The most common forms are adiabatic full passage (AFP) pulses, often realized with hyperbolic secant or tanh modulation. A  $180^\circ$  refocusing pulse can be replaced by an AFP pulse to achieve slice selective refocusing. As the pulse is frequency modulated, this causes a non-linear, position-dependent phase across the slice, which has to be refocused with a second identical AFP. Pairs of AFP pulses can therefore be used as a double spin echo element, which cancels phase errors and enables reliable refocusing.

## 2.6 Single Volume Localization

In order to give the measured signal meaning, a voxel localized in all three spatial directions has to be selected. The following section is based on de Graaf [1, chap. 4, chap. 6].

Localization can be achieved by applying field gradients to make the external field and thereby the Larmor frequency of the protons position-dependent given by

$$\nu(r) = \nu_0 + \left( \frac{\gamma}{2\pi} \right) G \cdot r, \quad (2.28)$$

where  $\nu$  is the Larmor frequency in MHz,  $G$  is the gradient in  $\text{Tm}^{-1}$ , and  $\gamma$  the gyromagnetic ratio. Then a frequency-selective RF-pulse can be applied to excite only spins of atoms in one spatial direction. This is repeated for all three spatial directions to select a voxel. The center of a slice selected by an RF pulse with center frequency  $\nu_{RF}$  is at position

$$r = \frac{2\pi(\nu_{RF} - \nu_0)}{\gamma G}. \quad (2.29)$$

To spoil unwanted coherences, each slice-selective refocusing pulse is flanked by two crusher gradients of equal area and same polarity. These impose a controlled, position-dependent phase given by

$$\phi(r) = \gamma \int G(t)r dt. \quad (2.30)$$

Because the refocusing pulse inverts the sign of the transverse coherence, the desired slice has zero net crusher moment and rephases at TE.

In contrast, unwanted coherences such as stimulated echoes and transverse magnetization from preceding pulses acquire a nonzero net moment and dephase, so they do not contaminate the signal of the selected slice.

### 2.6.1 Chemical Shift Displacement

As MRS relies on the measurement of different metabolites with Larmor frequencies that differ from that of water, this method of single voxel spectroscopy (SVS) is not always exact enough [1, chap. 6]. As the center of the slice selected by an RF pulse depends linearly on the Larmor frequency, a slice of spins with Larmor frequency  $\nu_0 + \Delta\nu$  is shifted by

$$\Delta r = -\frac{2\pi\Delta\nu}{\gamma G} \quad (2.31)$$

This is called the CSDE. The further the Larmor frequency of a metabolite is from water, the stronger this displacement becomes.

Therefore, in phantoms with abrupt concentration changes, slices must be chosen with sufficient margin to avoid contamination of the measured values. In vivo, this potential source of error likewise needs to be taken into account, especially when using outer volume suppression (OVS) or measuring gliomas, where results might be contaminated considerably.

To reduce the error, a stronger gradient with a proportionally increased RF pulse amplitude may be chosen. Equation (2.31) can be rewritten to include the bandwidth  $BW$  explicitly as

$$\Delta r_{CSDE} = -\frac{\Delta\nu}{BW} \cdot \Delta r_{Slice} \quad (2.32)$$

For conventional RF pulses, the bandwidth increases linearly with the RF amplitude. However, the SAR increases roughly with the square of the amplitude. The SAR limit therefore restricts the maximal bandwidth that can be chosen. This may be improved with adiabatic pulses, where the bandwidth increases with the square of the amplitude and can therefore be increased further. The error rises with the  $B_0$  field strength as the chemical shift differences in Hz are directly proportional to the magnetic field strength. It is therefore much more pronounced at 7 T than at 3 T.

### 2.6.2 PRESS

PRESS is a double spin echo localization method introduced in Bottomley [22]. It is the standard localization method employed in the Siemens product sequences I used. It combines a slice-selective excitation pulse with two slice-selective refocusing pulses.

First, a 90° excitation pulse excites only the spins in a plane with the thickness determined by the gradient and the amplitude of the RF pulse. At TE<sub>1</sub>/2, the first 180° pulse is applied, forming a spin echo at TE<sub>1</sub>. This echo only contains signal from the two orthogonal slices selected by the excitation and first refocusing pulse. The second 180° pulse refocuses the spin echo with a delay of TE<sub>2</sub>, so that the final spin echo is formed at TE = TE<sub>1</sub> + TE<sub>2</sub>. This second echo contains the signal only from the intersection of the three planes, the selected voxel. Signal outside the selected voxel is either not excited, not refocused, or dephased by magnetic field gradients in two directions. The timing of RF pulses and gradients is sketched in figure 2.7.

As explained in subsection 2.6.1, this method works well at lower field strengths such as 3 T, but the CSDE increases with  $B_0$ . To sufficiently increase the RF bandwidth, the SAR limit would have to be exceeded. Therefore, localization methods using adiabatic pulses such as Localization by Adiabatic Selective Refocusing (LASER) produce better results at 7 T.

### 2.6.3 LASER

LASER, a sequence developed by Garwood and DelaBarre [24], uses adiabatic excitation and refocusing pulses, specifically pairs of AFP pulses. As explained in subsection 2.5.3, for adiabatic pulses, not only the amplitude but also the frequency is modulated to satisfy the adiabatic condition: the spin magnetization vector remains aligned with the magnetic field if the field changes slowly enough relative to the spin's precession frequency. This makes the pulses more tolerant of  $B_1$  inhomogeneities [1, chap. 5].

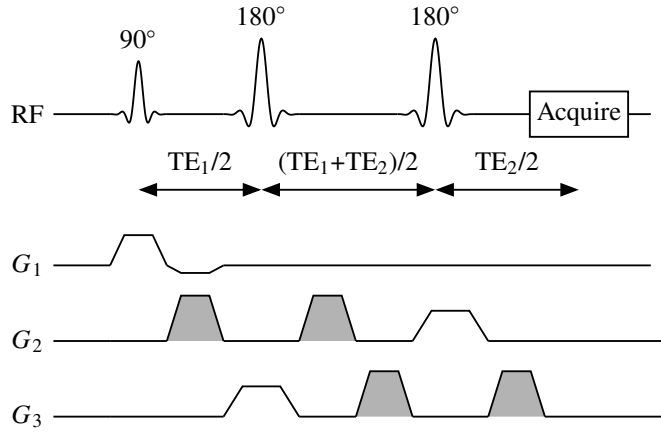


Figure 2.7: **PRESS sequence diagram:** RF pulse outlines with slice-select gradients (white) and crusher gradients (gray), figure created with `mrseqdia` [23] after de Graaf [1, chap. 6]; the spins are excited with a  $90^\circ$  pulse accompanied by a slice-select gradient and refocused with two  $180^\circ$  refocusing pulses, each with a slice-select gradient in one spatial direction and flanked by two crusher gradients in the other.

To localize a slice with LASER, the entire sample is first excited with a nonselective adiabatic excitation pulse, followed by three pairs of AFP pulses to localize the voxel in the three spatial directions. The interplay of magnetic field gradients and RF pulses is shown in figure 2.8.

In addition to being more robust against  $B_1$  inhomogeneities, this method allows for larger bandwidths, which makes the localization edges sharper and reduces the CSDE (see subsection 2.6.1). However, because they use more pulses, LASER sequences have longer acquisition times. In order to reduce the minimum echo time, the semi-LASER method was developed.

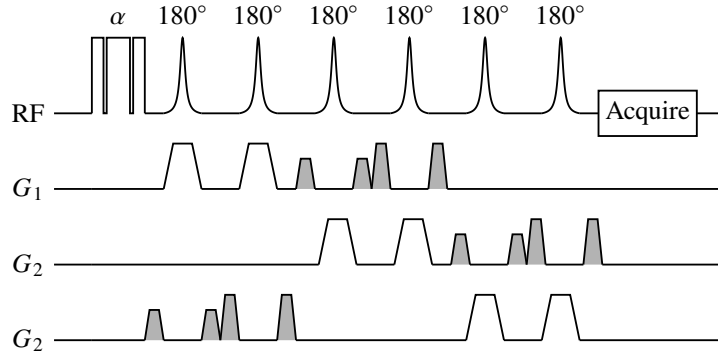


Figure 2.8: **LASER sequence diagram:** RF pulse outlines with slice-select gradients (white) and crusher gradients (gray), figure created with `mrseqdia` [23] after de Graaf [1, chap. 6]; the spins are excited with a nonselective  $90^\circ$  pulse and refocused with two pairs of AFP pulses, each with a slice-select gradient in one spatial direction and flanked by two crusher gradients in another.

#### 2.6.4 Semi-LASER

In order to reduce the minimum TE, and thereby the minimum possible acquisition time, one of the three AFP pairs is replaced with a single slice-selective excitation pulse. This method was first introduced by Scheenen et al. [25]. Figure 2.9 shows the timing of the magnetic field gradients and RF pulses. Although the measurement times are still longer than those for PRESS, this method is best suited for my measurements as it is robust and reliable, even at higher field strengths.

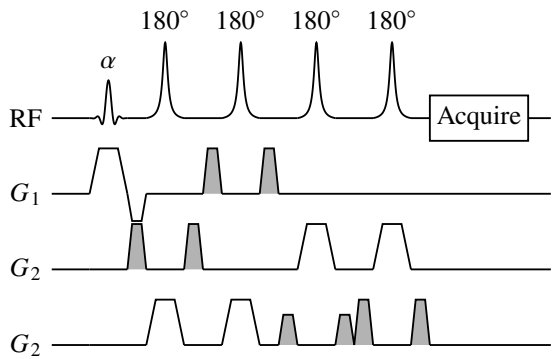


Figure 2.9: **Semi-LASER sequence diagram:** RF pulse outlines with slice-select gradients (white) and crusher gradients (gray), figure created with `mrseqdia` [23] after de Graaf [1, chap. 6]; the spins are excited with a slice selective  $90^\circ$  pulse accompanied by a slice-select gradient and refocused with two pairs of AFP refocusing pulses, each with a slice-select gradient in one spatial direction and flanked by two crusher gradients in the other.

## 2.7 Chemical Shift Imaging

SVS can be extended to yield spectral information for multiple voxels by adding spatial phase encoding to the acquisition [1, chap. 7]. This is referred to as chemical shift imaging (CSI) or magnetic resonance spectroscopic imaging (MRSI).

In practice, a standard SVS sequence like PRESS or LASER is modified to excite a slice-shaped voxel extended in two spatial directions and combined with additional phase encoding gradients that encode the two spatial directions within the slice during one of the free evolution periods. Instead of acquiring a single FID, an array of FIDs is recorded with systematically varied phase-encoding gradients.

After Fourier transformation along the spatial dimensions, this yields a grid of spectra corresponding to multiple voxels within the selected slice. Because phase encoding must be repeated for each spatial step, CSI measurements take significantly longer than SVS, reducing the number of averages possible during the measurement. Additionally, CSI is more sensitive to  $B_0$  inhomogeneities across the volume, which can cause spatial mislocalization within the slice.

## 2.8 Water Suppression

Because of the high water content of mammalian tissue, the spectrum in  $^1\text{H}$ -MRS is dominated by the signal of the two water protons resonating at 4.7 ppm. As the concentration of the metabolites of interest is often more than 1000 times lower than that of water, the water peak causes baseline distortions and vibration-induced signal modulations. This makes the quantification of metabolites unreliable, which is why several methods to suppress the water resonance have been developed. This overview of the methods I used follows de Graaf [1, chap. 6].

### 2.8.1 CHESS

The most straightforward method to suppress the water signal is to excite only the water spins into the transverse plane with a frequency-selective RF pulse and destroy coherence with a crusher gradient.

This was first realized by Haase et al. [26] with Chemical Shift Selective (CHESS) water suppression, a frequency-selective excitation method. Before the main pulse sequence, a frequency-selective RF pulse is applied to excite the water spins into the transverse plane, followed by a magnetic field gradient to destroy coherence.

However, the frequency selective RF pulse does not have sharp edges, which might cause partial suppression of other metabolites that fall within the suppression range. In my case, the Cr-CH<sub>2</sub> peak and the 2HG peak at 4.15 ppm might be particularly affected by an overly broad water suppression bandwidth due to their small

chemical shift difference from water. Usually, a Gaussian line shape is chosen to minimize this effect as it has a relatively sharp cutoff.

The suppression may be improved by applying three successive Gaussian pulses. Nevertheless, the water signal might not be completely suppressed due to  $T_1$  relaxation and inhomogeneous  $B_1$  fields.

### 2.8.2 WET

It is also possible to exploit  $T_1$  relaxation to improve suppression, as demonstrated by Ogg, Kingsley, and Taylor [27] with the Water Suppression Enhanced Through  $T_1$  Effects (WET) sequence. A WET sequence generally consists of four RF pulses, each followed by crusher gradients. In order to compensate for  $T_1$  relaxation between the pulses, the nutation angles of the pulses are optimized accordingly. This is also a frequency-selective method, which again puts resonances close to water at risk of partial suppression.

### 2.8.3 VAPOR

An alternative CHESS-based approach involves optimizing the relaxation delays and adapting pulse power, a technique developed by Tkáč et al. [28] known to as Variable Pulse Power and Optimal Relaxation Delays (VAPOR).

Because water has long  $T_1$ , suppression is improved by timing the excitation pulses to repeatedly interrupt recovery. Usually, seven frequency-selective RF excitation pulses are applied to gradually reduce the longitudinal magnetization of the water spins toward zero.

### 2.8.4 Presaturation

Instead of exciting the water resonance and dephasing the spins in the transverse plane with a crusher gradient, the same effect can theoretically be achieved by applying a long, low-power RF pulse in the order of  $T_1$ . This way, the spins reach the transverse plane at different times and are therefore automatically dephased.

In practice, the saturation is hindered by  $T_1$  relaxation, so complete saturation cannot be achieved. Presaturation is most effective for an irradiation time of 2–3  $T_1$ , but a more practical approach is to first choose the pulse length and then optimize the pulse power for the given TR.

Presaturation yields very good results for liquid phantoms. However, this method presents a higher risk of saturating peaks close to water than other water suppression methods, so the bandwidth has to be chosen carefully. Additionally, metabolite concentrations might be obscured through off-resonance magnetization transfer between  $^1\text{H}$ -MRS-invisible, bound protons and  $^1\text{H}$ -MRS-visible, mobile protons. Another disadvantage for in vivo measurements is the higher heat deposition compared to other water suppression methods.

I used presaturation in the first measurements with the MEGA PRESS (mPRESS) sequence, as the obtained spectra showed a very clean baseline without oscillations around the water peak.

Interestingly, the metabolite peaks were inverted while the residual water was not. This may be because water magnetization is directly saturated and remains aligned with the RF carrier. However, the presaturation pulse is not infinitely selective and applies a small off-resonance  $B_1$  field to other resonances. An off-resonance RF pulse then produces a frequency-dependent rotation of the magnetization vector, causing a global phase shift in the metabolite signal. Despite the visually good performance, I encountered the same problem as described by de Graaf [1, chap. 6]: the partial saturation of  $\text{Cr}-\text{CH}_2$ .

### 2.8.5 MEGA Suppression

Instead of suppressing water before excitation, it is also possible to avoid  $T_1$  relaxation by including suppression during the spin echo period. This increases the minimum TE and is therefore not suitable for short-TE measurements, but can readily be applied in J-difference editing sequences (see section 2.9). These sequences use the

same method to suppress metabolite peaks and are therefore naturally suited to also use it for water suppression. The suppression is achieved by selective refocusing, for example with MEGA [29] (see figure 2.10).

First, a non-selective  $90^\circ$  RF pulse excites all spins to the transverse plane. As before, two crusher gradients are applied on either side of a refocusing pulse.

For unsuppressed metabolites, a broadband  $180^\circ$  refocusing pulse between the gradients rephases their magnetization. For water, however, an additional frequency-selective  $180^\circ$  inversion pulse is applied. Because of this additional inversion, the water signal is not rephased and effectively suppressed by the crusher gradients. MEGA can also be realized with adiabatic pulses, which makes the suppression largely insensitive to  $B_1$  inhomogeneities.

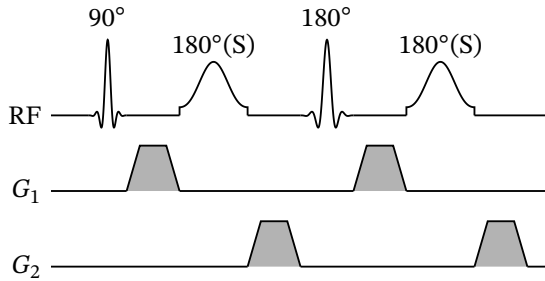


Figure 2.10: **MEGA water suppression:** All metabolites including water are excited with a non-selective  $90^\circ$  excitation pulse and are then subjected to two orthogonal magnetic field gradients. While the other metabolites experience only one refocusing pulse between two equal gradients, an additional frequency-selective refocusing pulse ( $180^\circ$  (S)) dephases only the water magnetization in the transverse plane; figure created with `mrseqdia` [23] after de Graaf [1, chap. 6].

## 2.9 J-Difference Editing

One of the main challenges in  $^1\text{H}$ -MRS is that the resonances of many metabolites overlap strongly in the spectrum. This makes the quantification of multiplet resonances challenging, since they intrinsically have lower amplitudes than singlets and are often hidden underneath stronger peaks. J-difference editing is a technique used to separate these signals, exploiting the scalar coupling mechanism explained in subsection 2.2.3 [1, chap. 8]. In a coupled spin system, the transverse magnetization evolves under J-coupling according to cosine modulation

$$M(t) \propto \cos(\pi Jt). \quad (2.33)$$

This oscillation can either proceed freely or be suppressed by applying a frequency-selective inversion pulse to the coupling partner of the measurement target, referred to as the editing target.

Two acquisitions are performed: an edit-ON with a selective editing pulse that refocuses the coupling partner, thereby suppressing the modulation, and an edit-OFF without this pulse, where J-modulation is not altered. Subtracting the two spectra removes signals from uncoupled metabolites, isolating the difference signal of the measurement target.

To maximize this difference, TE is chosen such that the J-modulation difference is largest, typically  $TE \approx (2J)^{-1}$ , corresponding to the first inversion point of the cosine modulation. For GABA, this corresponds to a TE of 68 ms. The frequency-selective refocusing can be implemented with MEGA (see subsection 2.8.5) in combination with different localization methods. Figure 2.11 shows the implementation for mPRESS. The sequence diagram for MEGA semi-LASER (msLASER) is shown in figure 2.12. In practice, the frequency-selective refocusing pulse is included in both acquisitions, but in the edit-OFF spectrum a frequency range on the other side of the water peak without interesting resonances is chosen.

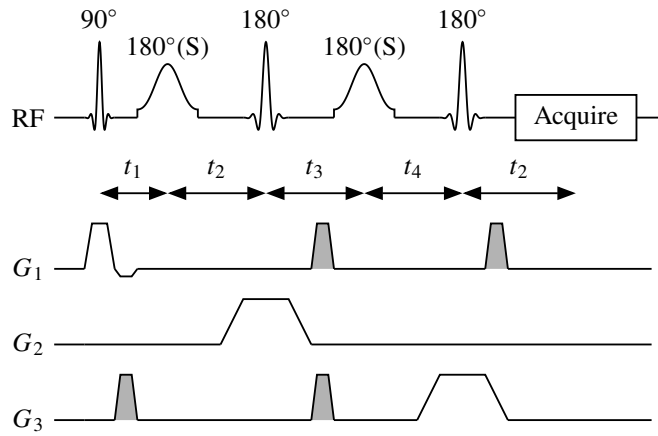


Figure 2.11: **MEGA PRESS sequence diagram:** PRESS sequence with an additional frequency-selective refocusing pulse between each pair of crusher gradients (gray); refocusing cancels only for the selected frequency of the editing target; figure created with `mrseqdia` [23] after de Graaf [1, chap. 8].

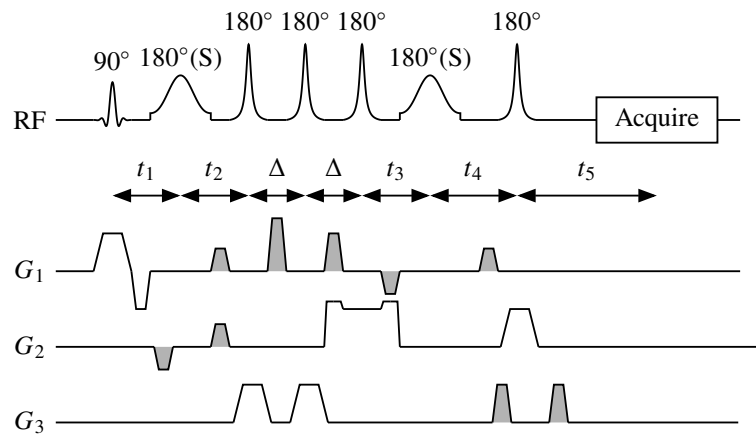


Figure 2.12: **MEGA semi-LASER sequence diagram:** semi-LASER (sLASER) sequence with an additional frequency-selective refocusing pulse between each pair of crusher gradients (gray); refocusing cancels only for the selected frequency of the editing target; figure created with `mrseqdia` [23] after de Graaf [1, chap. 8].

# Chapter 3

## Experimental Methods

I performed all measurements on a MAGNETOM Terra.X 7 T scanner (Siemens Healthineers AG, Erlangen, Germany) with a 32 Rx / 8 Tx-channel head-coil (Nova Medical, Wilmington, USA). First, I scanned phantoms with known metabolite concentrations to optimize post-processing and quantification, and then acquired brain spectra from healthy volunteers. All *in vivo* examinations were approved by the local ethics committee and were performed after obtaining informed written consent from all the subjects.

### 3.1 Phantom Construction

I constructed three phantoms: the first for preliminary experimenting, the second with varying GABA concentrations to specifically measure GABA and the third to measure 2HG.

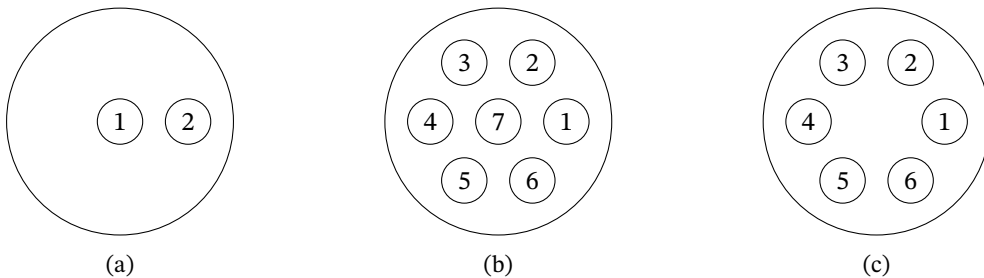


Figure 3.1: **Sketches of my phantoms:** (a) phantom 1 for practicing, (b) phantom 2 for GABA and (c) phantom 3 for 2HG.

#### 3.1.1 Phantom 1

The first phantom I built consisted of a 2 L plastic container in which two 50 ml plastic vials were fixed. I chose phosphate-buffered saline (PBS) as the base to fill the container and dissolve the solid compounds due to its physiological pH and ionic strength. These properties help stabilize the metabolites and reduce pH-induced spectral shifts.

The vials contained NAA, Cr, Cho, and GABA, as those are the origin of the brain's major spectral features in MRS. In vial 1, I replicated the metabolic profile of healthy brain tissue, while the composition of vial 2 simulated the spectrum characteristic of pathological brain conditions with lower NAA and higher Cho concentrations. The concentrations I chose are listed in table 3.1.

I prepared the first phantom by directly weighing solid compounds using an analytical scale with  $\pm 1$  mg accuracy.

I then dissolved them in PBS, filling up each vial to the brim, the volume being 55 mL. Given the uncertainties introduced by weighing and transfer losses, I estimate the uncertainty in the final metabolite concentrations at  $\pm 10\%$ .

Table 3.1: **Phantom 1:** metabolite concentrations in mM, uncertainties reflect assumed preparation errors.

Metabolite	Vial 1	Vial 2
NAA	$10.75 \pm 1.08$	$2.72 \pm 0.27$
Cr	$7.51 \pm 0.75$	$7.32 \pm 0.73$
Cho	$1.41 \pm 0.14$	$2.72 \pm 0.27$
GABA	$1.11 \pm 0.11$	$1.06 \pm 0.11$

### 3.1.2 Phantom 2 – The GABA Phantom

I built the second phantom in order to establish the measurement of GABA. I made four vials with the NAA, Cr, and Cho characteristic of healthy brain tissue and three vials with the composition characteristic of gliomas, as these are the metabolites that typically pose a challenge in the measurement of GABA due to their relatively strong resonances obscuring the GABA peaks.

In these vials, I varied the GABA concentration from 1 mM – a typical concentration in the brain – to an easily detectable concentration of 10 mM. The metabolite concentrations are summarized in table 3.2.

First, I prepared highly concentrated stock solutions in order to reduce the relative measurement error induced by weighing the metabolites. I prepared these stock solutions by dissolving 0.50 – 1.05 g of solid compound in 50 mL PBS. As before, I measured the masses with an accuracy of  $\pm 1$  mg using a calibrated analytical scale. From these stocks, I pipetted the volumes needed to reach the desired concentrations into the individual vials and adjusted the final volume by filling the vials to 50 mL with PBS. Based on pipetting precision, weighing accuracy, and final volume adjustment, I estimate the uncertainty in the final metabolite concentrations at  $\pm 5\%$ .

Table 3.2: **Phantom 2:** metabolite concentrations in mM, uncertainties reflect assumed preparation errors.

Metabolite	Vial 1	Vial 6	Vial 5	Vial 4	Vial 3	Vial 2	Vial 7
NAA	$12 \pm 0.6$	$12 \pm 0.6$	$12 \pm 0.6$	$12 \pm 0.6$	$3 \pm 0.15$	$3 \pm 0.15$	$3 \pm 0.15$
Cr	$8 \pm 0.4$	$8 \pm 0.4$	$8 \pm 0.4$	$8 \pm 0.4$	$8 \pm 0.4$	$8 \pm 0.4$	$8 \pm 0.4$
Cho	$1.5 \pm 0.08$	$1.5 \pm 0.08$	$1.5 \pm 0.08$	$1.5 \pm 0.08$	$3 \pm 0.15$	$3 \pm 0.15$	$3 \pm 0.15$
GABA	$1 \pm 0.05$	$2 \pm 0.1$	$5 \pm 0.25$	$10 \pm 0.5$	$1 \pm 0.05$	$5 \pm 0.25$	$10 \pm 0.5$

### 3.1.3 Phantom 3 – The 2HG Phantom

The third and final phantom included the metabolite 2HG in addition to NAA, Cr, Cho, and GABA. As explained in subsection 5.2.6, the measurement of 2HG is even more challenging than that of GABA due to its weaker J-coupling. It is a marker of the IDH mutation in gliomas with clinically relevant concentrations ranging from 3 mM to 5 mM.

Because it is usually found in gliomas, I prioritized pathological concentrations and prepared four pathological and two healthy vials. Because the GABA editing target is in the same frequency range as the 2HG editing target – which could complicate 2HG detection – I prepared vials both with and without GABA. The metabolite concentrations in Phantom 3 are listed in table 3.3.

I again prepared stock solutions by dissolving between 38.67 mg and 262.26 mg of each compound in PBS. To prevent microbial growth and allow room-temperature storage, the PBS contained 0.1 mM copper sulfate ( $\text{CuSO}_4$ ). These stock solutions were then mixed in the necessary proportions to prepare the individual vials. Each vial

was filled to approximately 55 ml, with slight overfilling to eliminate air bubbles. This was necessary as this phantom was constructed to lie in the head coil with the vials oriented along the  $B_0$  field direction to align better with the symmetry of the coil.

However, it resulted in a small, uncontrolled volume loss. Considering weighing accuracy, pipetting precision, and solution loss due to overfilling, I estimate the uncertainty in the final concentrations to be  $\pm 7 - 10\%$ .

Table 3.3: **Phantom 3:** metabolite concentrations in mM, uncertainties reflect assumed preparation errors.

Metabolite	Vial 1	Vial 2	Vial 3	Vial 4	Vial 5	Vial 6
NAA	$10 \pm 1$	$1.5 \pm 0.15$	$1.5 \pm 0.15$	$10 \pm 1$	$1.5 \pm 0.15$	$1.5 \pm 0.15$
Cr	$5 \pm 0.5$					
Cho	$1.5 \pm 0.15$	$3 \pm 0.3$	$3 \pm 0.3$	$1.5 \pm 0.15$	$3 \pm 0.3$	$3 \pm 0.3$
GABA	$1.5 \pm 0.15$	0	0	$1.5 \pm 0.15$	$1.5 \pm 0.15$	$1.5 \pm 0.15$
2HG	0	$1.5 \pm 0.15$	$3 \pm 0.3$	$3 \pm 0.3$	$1.5 \pm 0.15$	$3 \pm 0.3$

## 3.2 Measurement Procedure

Before the actual measurements, I acquired localizer scans required for voxel selection. For the CSI sLASER sequence, voxel outlines were not displayed, so I positioned the voxel using a product CSI sequence and then copied the slice selection and shim volume to the actual sequence.

For standard spectroscopy and J-difference editing, I initially used product single-voxel sequences with water suppression by either presaturation or WET, consisting of four pulses. Outer-volume saturation bands were placed around the voxel. With these bands, metabolite-specific chemical shifts produced noticeable CSDEs, especially for NAA, the metabolite farthest from water.

To reduce CSDE and improve localization at ultra-high field, I switched to an sLASER and msLASER sequence developed by Gülin Öz [30] and Dinesh Deelchand [31] and provided by the University of Minnesota under a C2P agreement. In these sequences, water suppression was achieved with VAPOR and 1D outer volume suppression was applied automatically with a slab thickness of 80 mm and a slab position offset of 7 mm.

$B_0$  shimming was performed using the automatic Advanced routine, and, if necessary, further improved by repeating the DESS Standard and DESS Advanced routines using the manual adjustments task card until sufficient homogeneity was reached.

All measurements used the vendor-provided TrueForm mode for  $B_1$  field distribution, which is equivalent to circularly polarized distribution, meaning that all eight transmit coils are combined to provide the same field as a single virtual coil.

During the project, the third-order shim coil became unavailable due to hardware failure and was removed from the shimming routine. As a result, achieving sufficient  $B_0$  homogeneity became more challenging, which occasionally limited spectral quality.

## 3.3 Water Suppression

In the course of this project, I mainly used three different water suppression methods: in the initial measurement with the product PRESS sequence, three options were offered: weak water suppression, spectral water suppression, and water saturation. Weak water suppression could not achieve sufficient suppression in the phantoms. Spectral water suppression refers to a WET sequence consisting of four pulses, but it was not available for the corresponding mPRESS sequence. Water saturation most likely refers to presaturation (see subsection 2.8.4). This method caused an inversion of the metabolite peaks, which I corrected by phase correction.

As the mPRESS sequence, originally developed for 1.5 T, caused a significant CSDE at 7 T, I instead used the sLASER and msLASER sequences, where water suppression was achieved with VAPOR.

The different water suppression methods, applied in the same cubic voxel with side length 18 mm, a water suppression bandwidth of 135 Hz, and scaled to Cr-CH<sub>3</sub> peak height, are compared in figure 3.2. For spectral water suppression in the product sequence, the bandwidth was specified in ppm and was set to 0.5 ppm. The VAPOR sequence requests a water suppression delta frequency, which I set to -0.16 ppm. All spectra were sampled over 2048 data points with TR= 3 s, TE= 68 ms, and an excitation flip angle of 90°. 64 averages were acquired over a bandwidth of 2200 Hz.

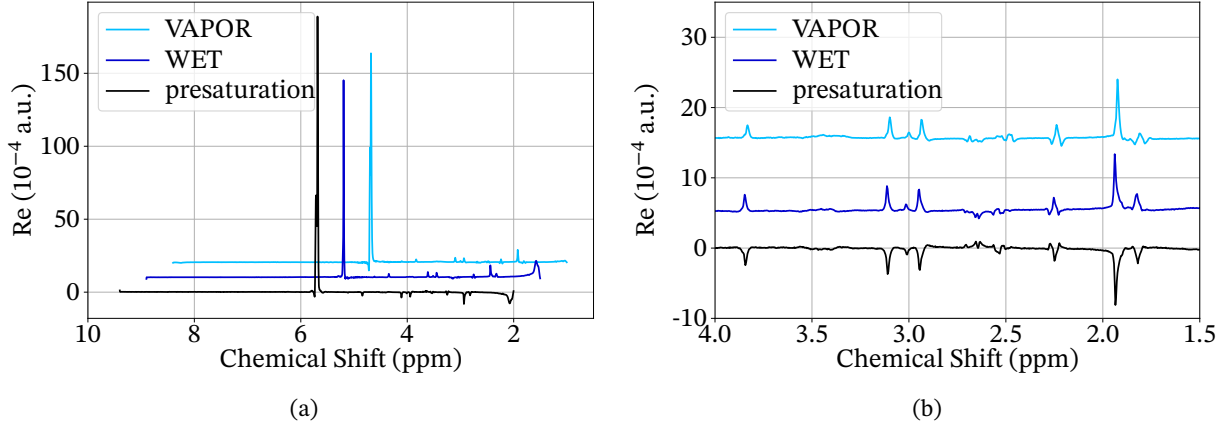


Figure 3.2: **Comparison of water suppression methods:** presaturation (black) and WET (blue) measured with the Siemens PRESS sequence and VAPOR (light blue) with the sLASER sequence; **(a)** whole spectrum and **(b)** zoom on metabolite peaks; offset and scaled to the Cr-CH<sub>3</sub> amplitude.

### 3.4 Temperature Dependence of the Water Resonance Frequency

Temperature effects play an important role in MRS, since frequency shifts relative to the water resonance frequency can cause frequency-selective pulses to miss their target. I solved this problem by measuring the current shift with a simple product sequence prior to the editing sequences.

As explained in subsection 2.2.6, the chemical shift of other compounds is determined in reference to the water peak. However, the water resonance frequency is temperature dependent, causing the water peak in pure water to shift by  $-0.0103 \pm 0.00006 \text{ ppm}/^\circ\text{C}$  [32].

This especially impacted measurements in the GABA phantom, as it was kept in a refrigerator at approximately 4 – 6 °C to extend its durability despite the absence of CuSO<sub>4</sub>. During the measurement time of approximately

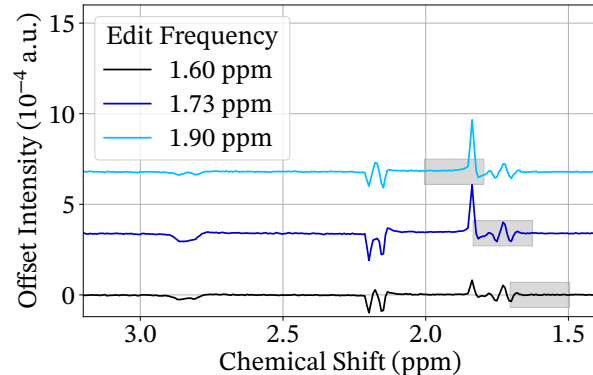


Figure 3.3: **Temperature dependence of the edit frequency:** three difference spectra acquired at approximately 16 °C with three different edit frequencies; 1.9 ppm (light blue), 1.73 ppm (blue) and 1.6 ppm (black); the edit bandwidth visualized with a gray background; the calculated edit frequency clearly covers the editing target the best.

two hours, the temperature rose to room temperature. This caused a significant shift of the peak positions with respect to values reported in the literature, where the chemical shifts are usually given at body temperature ( $37^{\circ}\text{C}$ ). Additionally, the temperature might vary by up to  $15^{\circ}\text{C}$  between measurements, and removing the phantom from the scanner and remeasuring the temperature for each measurement would cause significant time loss. This especially affected the edit sequence, where the frequency range to be suppressed has to be entered in reference to the water peak, and the chemical shift of the water peak has to be accounted for in order to obtain good suppression of the editing target.

I realized this by first running a simple SVS sequence before each measurement to roughly determine the shift of the NAA peak from the expected chemical shift of 2.01 ppm. For this measurement, I chose vial 1 with high NAA and low GABA concentration, assuming that the temperature does not vary too strongly throughout the phantom. Then, I calculated the edit frequency with the determined shift.

With this method, I exploited the fact that the NAA resonance remains unaffected by temperature change as described in Corbett, Laptook, and Weatherall [32] and gives the strongest peak in my control phantom. While this method is far from being exact, as the temperature might still vary slightly during the two measurements, causing an additional shift, the determined edit frequency is close enough for the editing target to be well within the edit bandwidth of 62 Hz for a  $B_0$  field of 7 T.

Figure 3.3 shows the difference spectra acquired at approximately  $16^{\circ}\text{C}$  with three different edit frequencies: the standard edit frequency of 1.9 ppm (light blue) valid for in vivo measurements, the calculated edit frequency of 1.73 ppm (blue) and – for comparison – a third lower edit frequency of 1.6 ppm (black). The edit bandwidth is visualized with a gray background, although one has to keep in mind that the actual suppressed bandwidth does not have well-defined edges. It shows that the GABA resonance found at 1.89 ppm during in vivo measurements is best suppressed with the calculated edit frequency, resulting in the strongest GABA signal at the detection target.

For the construction of the 2HG phantom, I avoided the temperature instabilities by adding  $\text{CuSO}_4$  to prevent microbial growth so the phantom could be stored at room temperature. This way, I only had to measure the shift at room temperature once.

# Chapter 4

## Data Processing

I quantitatively analyzed the  $^1\text{H}$ -MRS spectra in Python (version 3.13.2) by fitting models consisting of individually parameterized peaks and a baseline. The evaluation code and one example fit are available at [33].

### 4.1 Fitting Routine

To account for phase shifts during acquisition, I used a two-step fitting procedure. In the first step, the model spectrum was fitted to the data with zero- and first-order phases included as free parameters. The acquired spectrum was then corrected using the fitted phase values. In the second step, I refitted the baseline and peaks without phase parameters, since the phase-corrected spectrum was expected to approximate a pure absorption spectrum.

This procedure was implemented as follows. Given a complex peak-plus-baseline model with Voigt or Lorentzian peaks  $P(k)$  and a baseline  $B(\omega)$ , the model prior to phase application is

$$M(\omega) = \sum_k P(k) + B(\omega). \quad (4.1)$$

To this complex model, zero- and first-order phase terms ( $\phi_0$  and  $\phi_1$ ) are applied as

$$M_\phi(\omega, \phi_0, \phi_1) = M(\omega) \cdot e^{i(\phi_0 + \phi_1 \cdot 2\pi\omega)}, \quad (4.2)$$

where the exponential factor applies a frequency-dependent rotation in the complex plane, with  $\omega$  denoting frequency. For the rotation in the complex plane, I wrote the Python function `apply_phase(spec, freq, ph0, ph1)`. The fit objective then matches the real part of  $M_\phi$  to the measured real spectrum using the `scipy.optimize.curve_fit` function. Optionally, user-defined frequency regions (e.g., containing peaks not being fitted) may be excluded, in which case the fit is performed using `scipy.optimize.least_squares`.

In the second fitting step, the peak-plus-baseline model is refitted to the corrected spectrum with phase fitting disabled (`with_phase=False`).

### 4.2 Baseline

I modeled the baseline using one of two smooth function families: Chebyshev polynomials or cubic splines. The baseline parameters were fitted together with the line shape and phase parameters using least-squares. Both baselines are smooth, low-frequency models intended to capture insufficient water suppression, background and macro-molecular contributions without fitting narrow peaks.

The choice between Chebyshev and spline is dataset-dependent: Chebyshev is compact and fast while the spline can adapt locally where the background changes unevenly. In most cases, both yielded the same result, but occasionally, I observed edge roll-off with the Chebyshev baseline whereas the cubic spline remained stable at the spectrum ends thanks to its boundary conditions. I therefore preferred the spline in most fits.

### 4.2.1 Chebychev-polynomial Baseline

Chebyshev polynomials are numerically stable on  $[-1, 1]$ . Therefore, the frequency axis  $\omega$  is first affinely normalized to

$$\tilde{\omega} = 2 \cdot \frac{\omega - \omega_{min}}{\omega_{max} - \omega_{min}} - 1. \quad (4.3)$$

The baseline is then evaluated as a Chebyshev series

$$B_{cheb}(\omega) = \sum_{k=0}^K c_k T_k(\tilde{\omega}), \quad (4.4)$$

where  $T_k$  is the Chebyshev polynomial of degree  $k$  and  $c_k$  are the coefficients to be fitted. I implemented this using NumPy's `chebval` for efficient and stable evaluation on the normalized grid. [34] The polynomial order  $K$  is given by `len(coeffs) - 1`. Higher orders allow more flexibility but risk absorbing true spectral structure; I kept  $K$  modest and checked residuals.

### 4.2.2 Cubic-spline Baseline

As an alternative with localized flexibility, I used a natural cubic spline. With  $n$  denoting the number of spline control points ("knots"), chosen uniformly across the spectral domain, this gives:

$$w_i = w_{min} + \frac{i - 1}{n - 1} (w_{max} - w_{min}), \quad i = 1, \dots, n. \quad (4.5)$$

The coefficients  $c_i$  represent the baseline values at these knot locations. The cubic spline  $S(w)$  interpolates the pairs  $(w_i, c_i)$  with natural boundary conditions,  $S''(w_{min}) = S''(w_{max}) = 0$ , which avoids over-constraining the ends and reduces edge oscillations. I implemented this with SciPy's `CubicSpline` with `bc_type='natural'`, which sets the second derivative at both endpoints to zero, making the curve straight at the boundaries. [35] The baseline is then  $B_{spline} = S(w)$  and the number of knots is given by `n=len(coeffs)`. More knots increase flexibility but also the chance of over-fitting; I used a small to moderate  $n$  (3 – 5 knots) and verified the residuals remained structureless.

## 4.3 Peak Modeling

In addition to the baseline, my fit model included the peaks. Traditionally, MRS spectra are modeled as Lorentzian peaks. However, as discussed in section 2.4, a Voigt profile often yields better results as it also accounts for inhomogeneity. As the Voigt profile fits both  $\sigma$  and  $\gamma$ , the Voigt peak model has one more parameter per peak than the Lorentz peak model. Consequently, if both models provide the same fit quality, the Lorentz model is preferable because it uses fewer parameters, reducing the risk of overfitting.

To compare the two profiles, I chose a variety of spectra from different measurements, with wide range of SNR, concentrations, and measurement methods. I then fitted NAA, Cr, and Cho with both models and computed the mean squared residual between the data and the fit to compare.

As only the peak regions are relevant to quantification, only the residuals in these regions were considered. The residuals within that mask were squared and averaged to yield a mean squared error (MSE) for each spectrum. To enable comparison between spectra, I normalized the residuals to the Cr-CH<sub>3</sub> peak height. To test the limits of the fit, I did not exclude any regions despite of the high GABA concentration in some of the spectra.

Table 4.1: **Overview of the spectra fitted to compare Voigt and Lorentz peaks:** for each index, subject, region, sequence and voxel side length are listed; all voxels were cubic; the special column gives additional information on why the spectra were chosen for the comparison.

Index	Subject	Region	Special	Sequence	Voxel (mm)
1	GABA phantom	vial 1	high NAA, low GABA	sLASER	18
2	GABA phantom	vial 1	long TR	sLASER	18
3	GABA phantom	vial 1	small voxel	sLASER	12
4	volunteer 3	brain	anterior cingulate / medial frontal WM	msLASER	30
5	volunteer 3	brain	anterior cingulate / medial frontal WM	msLASER	20
6	GABA phantom	vial 3	low SNR, strong phase distortion	mPRESS	10
7	volunteer 1	brain	posterior cingulate / medial parietal WM	mPRESS	20
8	GABA phantom	vial 2	low NAA, high GABA	mPRESS	15
9	GABA phantom	vial 1	high NAA, low GABA	mPRESS	15
10	GABA phantom	vial 3	low NAA, low GABA	mPRESS	15

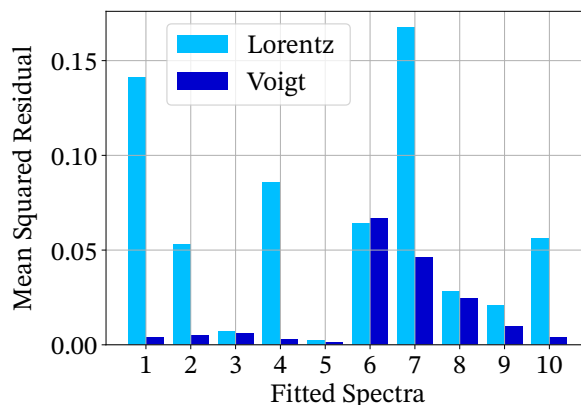


Figure 4.1: **Comparison of Lorentz and Voigt fit:** mean squared residual of the fit with Lorentz peaks (light blue) and with Voigt peaks (blue); residuals given in units of the Cr amplitude to ensure comparability.

The results are displayed as grouped bar plots in figure 4.1, showing Cr-CH<sub>3</sub>-normalized MSEs for Lorentzian and Voigt fits side by side for each spectrum.

In some of the spectra, the initial fit failed, distorting the corrected spectrum. For the Voigt model, this happened with spectra 6,7 and 8. Spectrum 6 had very low SNR; for spectrum 7, a good fit could be obtained by excluding regions and in spectrum 8, the phase fit was challenging without exclusions due to the high GABA content. In spite of that, spectrum 9 with equally high GABA content produced a relatively good fit, although the fitted Cr-CH<sub>3</sub> peak also included GABA.

For the Lorentz model, the fit failed for all the aforementioned spectra, and additionally for spectra 1, 2, 4 and slightly for 10, showing that the Voigt fit is more reliable.

The individual fits may be found in the appendix in figure A.4. With the exception of spectrum 6, where neither method produced a satisfactory fit, the Voigt model consistently gives a better outcome.

In any case, in the fit with the Voigt profile, the Gaussian broadening can always be set to  $\sigma = 0$ , rendering the profile purely Lorentzian. Therefore, I decided to use the Voigt profile in the remainder of this project.

## 4.4 Phase Correction

The acquired complex spectrum generally exhibits a residual frequency-dependent phase due to timing offsets caused by gradient delays, eddy currents, and phased-array coil combination. To recover absorption-mode line shapes and avoid bias in peak quantification, I modeled and corrected the phase with a zero-order (global) and first-order (linear) term. The effect of the global and linear phase on two modeled Lorentzian peaks of different amplitudes is shown in figure 4.2. I parameterized the phase shift as

$$\phi(\omega) = \phi_0 + \phi_1 \cdot 2\pi\omega, \quad (4.6)$$

where  $\phi_0$  is the zero-order phase in radians and  $\phi_1$  the first-order phase in rad/Hz.

I fitted the phase in the first fitting step, corrected the spectrum, and then fitted only the baseline and peaks to the phase-corrected spectrum.

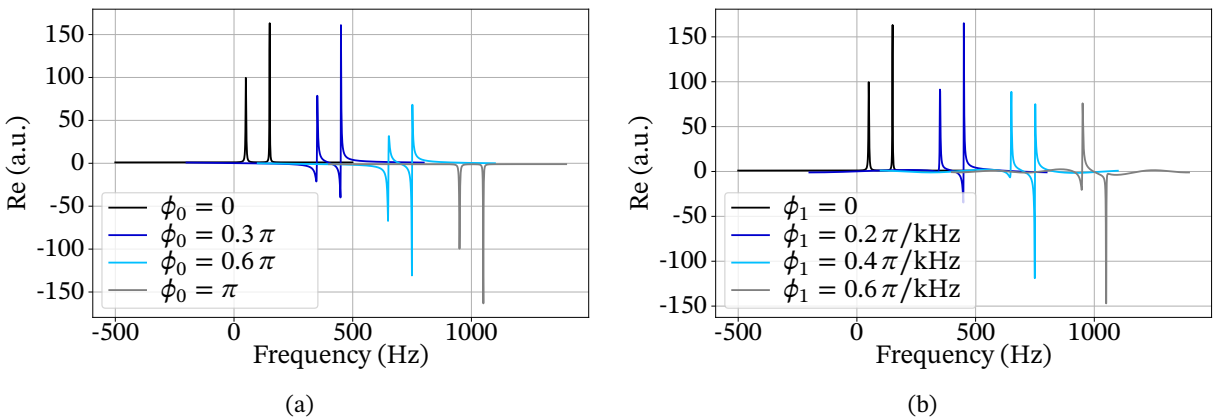


Figure 4.2: **Phase shift:** Effect of zero- (a) and first- (b) order phase shift on two simulated peaks.

## 4.5 Parallelization

To speed up the fitting of several spectra, I implemented task parallelism using `joblib.Parallel` (backend: `loky`) with `n_jobs=4`. The main process constructed a list of records and dispatched them to worker processes; one worker handled one record at a time by calling the fit helper function.

Inside each worker, I used a serial loop over a small grid of initial phase offsets ( $\text{ph0}$  deltas). For each record, I ran the first-stage fit for each delta, selected the candidate with the lowest residual norm, phase-corrected the spectrum, and then performed the second-stage fit. To avoid oversubscription, execution was restricted to a single inner thread.

I adapted the parallelization strategy from code generously provided by Köppel [36], originally developed for evaluating muscle chemical exchange saturation transfer (CEST) experiments.

## 4.6 $T_1$ Decay Correction

As explained in subsection 2.3.1, after excitation, the longitudinal relaxation of each metabolite recovers according to its  $T_1$  relaxation time. Since  $T_1$  is a metabolite-specific constant, this leads to  $T_1$  weighting if – due to time constraints – TR is not chosen long enough for a full recovery. This effect needs to be corrected during post processing. The measured signal depends on the flip angle,  $T_1$ , and TR as

$$S_{\text{meas}} = S_{T_2} \sin \theta \cdot \left( \frac{1 - e^{-TR/T_1}}{1 - \cos \theta \cdot e^{-TR/T_1}} \right). \quad (4.7)$$

The  $T_1$  correction only becomes negligible when

$$1 - e^{-TR/T_1} \approx 1, \quad (4.8)$$

which is the case when  $TR \geq 5T_1$ , at which point 99.3% of the signal is recovered. For the in vivo literature  $T_1$  values given in subsection 2.3.1, this would require a TR of about 10 s, resulting in long measurement times.

## 4.7 $T_2$ Decay Correction

In addition to longitudinal relaxation, transverse relaxation also has to be corrected to make the peak areas comparable between different resonances. From equation (2.17), the signal at  $t = 0$  can be computed:

$$S_{T_2} = S_{\text{meas}} \cdot e^{TE/T_2}. \quad (4.9)$$

This yields the total relaxation correction factor

$$S_0 = S_{\text{meas}} \left( \frac{1 - \cos \theta \cdot e^{-TR/T_1}}{1 - e^{-TR/T_1}} \right) \cdot e^{TE/T_2}. \quad (4.10)$$

## 4.8 Signal-to-Noise Ratio

The reliability of any metabolite ratio is limited by SNR, the contrast between a metabolite peak and the background noise. For each spectrum, I quantified SNR as the maximum signal in a narrow peak window divided by the noise standard deviation estimated from a peak-free window. In unedited spectra, I used Cr-CH<sub>3</sub> as a reference peak and in the edited difference spectra the peak enhanced through editing. I chose this simple, reproducible definition as it does not depend on model fits. Before SNR calculation, the spectra were phase cor-

rected and the baseline was subtracted.

The drawback is that even for pure noise, the computed SNR is counterintuitively not zero or one.

The pure noise SNR can be estimated by assuming pure white noise with  $N$  sampling points in the peak window in a Gaussian distribution with variance  $\sigma^2$ . According to van Handel [37], the maximum of such a normal distribution for  $N \rightarrow \infty$  scales with  $\sigma\sqrt{2\ln(N)}$ , which would lead to an  $\text{SNR} \approx \sqrt{2\ln(N)}$ . For a peak window with  $N = 30$ , the SNR of a random distribution might therefore lie around 2.7. Therefore, I discarded all spectra with SNR below 4.

## 4.9 Quality of the Fit

To estimate the quality of the fit, I computed the residuals to quantify how well the model reproduces the data. I also computed the estimated standard errors of the parameters using the covariance matrix returned by `curve_fit`. For fits with excluded regions, `least_squares` was used directly instead of `curve_fit` and the covariance matrix was approximated following the method of the `curve_fit` function in `scipy.optimize` ([38]) as

$$\hat{\Sigma} = \hat{\sigma}^2(J^\top J)^{-1}, \quad (4.11)$$

where  $J$  is the Jacobian of the residuals at the optimum and  $\hat{\sigma}^2 = ||r||^2/(n - p)$  is the residual variance estimate with the residual vector  $r$ , the number of fitted data points  $n$  and the number of free parameters  $p$ .

The standard deviations relative to the parameter estimates correspond to what is reported as Cramér-Rao Lower Bounds (CRLB) by LCModel [39], although here the variance is estimated from a user-defined signal free spectral region.

As the percentage standard deviations were below 2% for all fitted areas, I deemed the residuals the more significant measure of fit quality.

## 4.10 Comparison to LCModel

To obtain a first impression of the validity of my fitting approach, I compared the results to those obtained with the widely used LCModel algorithm for one representative spectrum. I chose a spectrum acquired with mPRESS at the beginning of the project, since the basis sets of NAA, Cr and Cho in mPRESS at  $TE = 68$  ms are automatically provided in the LCModel installation, while no suitable basis set for GABA or the sLASER sequence was at hand. Consequently, GABA is not included in this comparison.

Figure 4.3 shows the fit from my method (a) and from LCModel (b). The quantitative results are listed in table 4.2. Metabolite ratios are reported relative to Cr, in the case of my method to Cr-CH<sub>3</sub> with T<sub>1</sub> and T<sub>2</sub> correction applied, while LCModel reported tCr and tCho. For this single spectrum, the NAA/Cr and Cho/Cr ratios agree with LCModel within about 6%.

The global phase  $\phi_0$  is also in good agreement between the two fits. The linear phase shows a large relative deviation (over 100%), but its absolute value is very small. Thus, both fits yield values in the same order of magnitude, and such large percentage differences are not unexpected in this case.

It should be noted that the LCModel spectra were simulated for in vivo conditions, which may contribute to systematic differences between the two approaches.

Although this comparison is limited to one spectrum, it indicates that the metabolite ratios obtained with my method are in reasonable agreement with LCModel, while systematic differences remain, particularly in phase estimates.

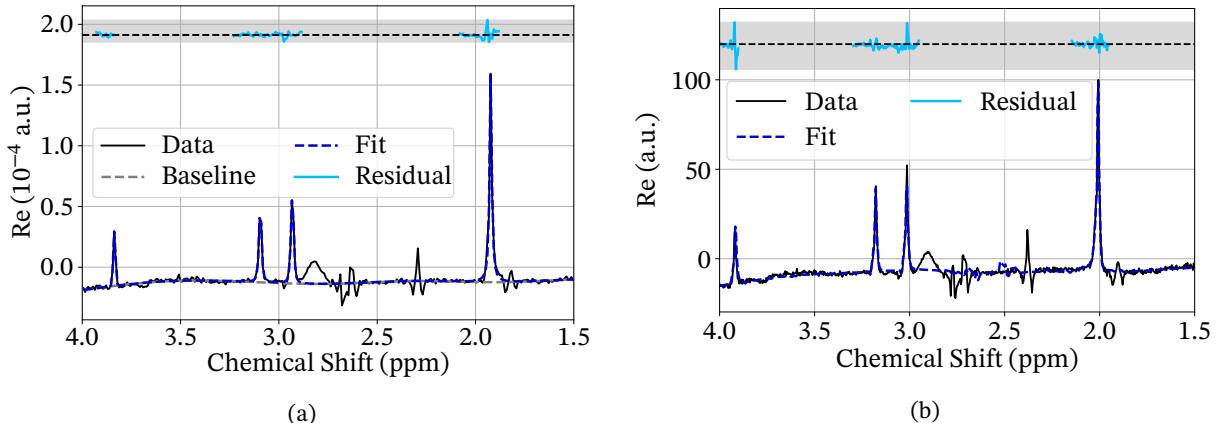


Figure 4.3: **Comparison to LCModel**: phase-corrected spectrum (black) with the fit (blue), baseline (gray) and residuals (light blue) obtained from **(a)** my method and **(b)** LCModel.

Table 4.2: **Comparison to LCModel:** NAA/Cr and Cho/Cr ratio and global and linear phase obtained with my approach and with LCModel for the same spectrum; for my approach, the ratios are given in units of Cr-CH<sub>3</sub> and T<sub>1</sub> and T<sub>2</sub> corrected; the last column gives the deviation from LCModel for each parameter

Ratio	My Fit	LCModel	Deviation
NAA / Cr	2.028	2.140	-5%
Cho / Cr	0.318	0.300	6%
$\phi_0(\pi)$	1	-0.97	3%
$\phi_1(\pi/\text{ppm})$	0.08	-0.05	-165%

# Chapter 5

## Measurements

Before the actual measurements, several preliminary measurements had to be performed. First, I had to figure out which voxel size I could safely choose inside the vials in my phantoms without compromising quantification by some peaks being shifted outside the vial.

As the exact pulse shape of my sequences is unknown, I had to estimate the CSDE caused by a given pulse duration based on measurement. I only performed this measurement for the sLASER sequence in a phantom, as the frequency offset – and therefore the CSDE – between water and metabolites unaffected by temperature is smaller *in vivo*.

Then, as discussed in subsection 2.3.4, the relaxation times in the phantoms had to be measured to enable accurate quantification. Finally, the actual measurements of NAA, Cr, Cho and GABA in the GABA phantom and *in vivo* could be realized. Although *in vivo* 2HG measurements were planned, I could only measure 2HG in the 2HG phantom as the patients with gliomas who could potentially have shown elevated 2HG withdrew from participation.

### 5.1 Estimation of the Chemical Shift Displacement Error in Field Direction

The sLASER sequence localizes the voxel adiabatically in two spatial directions, which reduces the CSDE significantly. Therefore, the only CSDE to be considered in this sequence is the shift in the spatial direction selected by the excitation pulse. As this pulse is not adiabatic, the CSDE might be considerable, especially for NAA, the resonance with the largest frequency offset.

In the original 3 T sequence described by Deelchand et al. [31], the R-value, which governs the dependence of the CSDE on pulse duration, can be chosen for each measurement. However, in the version I used, only the pulse duration was selectable. To estimate the R-value of the pulse, I therefore measured the CSDE at different excitation pulse durations.

**Methods** The 2HG phantom respects coil symmetry by positioning the vials along the direction of the magnetic field, so a shift in that direction only moves the metabolite voxels in the vial and does not alter the measured concentrations.

The GABA phantom, however, could not be laid in the coil, causing the chemical shift displacement to move individual metabolite voxels partially outside their vial or even into another vial. This provided me with the opportunity to estimate the dependence of the chemical shift on pulse duration. As explained in subsection 2.6.1,

the CSDE is proportional to the inverse of the bandwidth:

$$\Delta r_{CSDE} = \frac{\Delta\nu}{BW} \cdot \Delta r_{Slice} \quad (5.1)$$

The bandwidth, in turn, is proportional to the inverse of the pulse duration according to

$$BW = \frac{R}{\tau} \quad (5.2)$$

with the R-value given by the exact pulse shape. In order to estimate this constant, I oriented the GABA phantom so that the chemical shift occurred within the plane orthogonal to the axis of the cylindrical vial (radius  $r = 14$  mm). I chose a voxel with a side length equal to the inscribed square of the circle (side length  $s = \sqrt{2r}$ ), centered on the vial, with its edges aligned with the CSDE axis, the z axis. At the water center frequency, this voxel was fully contained by the circle, and just tangent at the midpoints, maximizing the sensitivity of the NAA volume fraction to small displacements.

Changes in the NAA peak area reflect the overlap between the square voxel and the circular vial as the NAA voxel shifts along z by

$$\Delta z_{CSDE}(\tau) = \frac{s \cdot \Delta\nu}{R} \cdot \tau \quad (5.3)$$

with the water-frequency separation  $\Delta\nu = \Delta\delta\nu_0/10^6$ . The chemical shift between NAA and water at room temperature was  $\Delta\delta = 2.74$ . To estimate the time-bandwidth product, I fitted the measured fractions to the analytic circle-square overlap model.

The overlapping area between the square voxel centered at  $d$  with the x-range  $[x_1, x_2] = [\delta - r/\sqrt{2}, \delta + r/\sqrt{2}]$  and the circular vial can be calculated as:

$$A(d) = \int_{x_1}^{x_2} \max(0, \min(\sqrt{2r}, 2\sqrt{r^2 - x^2})) dx. \quad (5.4)$$

The overlap fraction is

$$F(\delta) = \frac{A(\delta)}{2r^2}. \quad (5.5)$$

Assuming that the square is not completely outside the circle, the strip at position  $x$  contributes the chord height with

$$C(x) = 2\sqrt{r^2 - x^2}. \quad (5.6)$$

The anti-derivative of that expression is

$$G(x) = x\sqrt{r^2 - x^2} + r^2 \arcsin \frac{x}{r}, \quad (5.7)$$

so there are three cases: if the voxel lies fully inside the vial, the overlap is  $F(d) = 1$ . If the voxel has been shifted outside the vial, there is no overlap. And if the voxel partly overlaps with the vial the sides, where the contribution is limited by the circle, and the middle, where the contribution is limited by the square, have to be separated:

$$A(\delta) = A_{\text{middle}} + A_{\text{left}} + A_{\text{right}}, \quad (5.8)$$

$$A_{\text{middle}} = \sqrt{2}r \left[ \min\{x_2, b\} - \max\{x_1, -b\} \right]_+, \quad (5.9)$$

$$A_{\text{left}} = \left[ G(\min\{x_2, -b\}) - G(\max\{x_1, -r\}) \right]_+, \quad (5.10)$$

$$A_{\text{right}} = \left[ G(\min\{x_2, r\}) - G(\max\{x_1, b\}) \right]_+. \quad (5.11)$$

For the measurement, I chose a 20 mm  $\times$  20 mm  $\times$  20 mm voxel in the first vial with low GABA concentration

to avoid contaminating the NAA fit by the GABA resonance at 1.89 ppm. To keep the calculation simple, I oriented the GABA phantom so that a shift in z direction would not shift the NAA voxel into another vial, which allowed a shift of approximately 50% of the voxel depth. However, I still chose moderate bandwidths to avoid the inhomogeneous field at the water-air interface at the border of the phantom.

Keeping TE and all other parameters fixed, I repeated the semi-LASER acquisitions for varying excitation pulse durations  $\tau \in \{1480, 1760, 2000, 2240, 2480, 2760\}$ . I started with  $\tau = 1480$  to ensure that the minimal excitation pulse duration achieved the desired flip angle of  $78^\circ$ , the Ernst Angle of NAA for the chosen TR of 3 s.

I sampled the spectra with 2200 Hz over 2048 points with dwell time  $454.6 \mu\text{s}$  and VAPOR water suppression

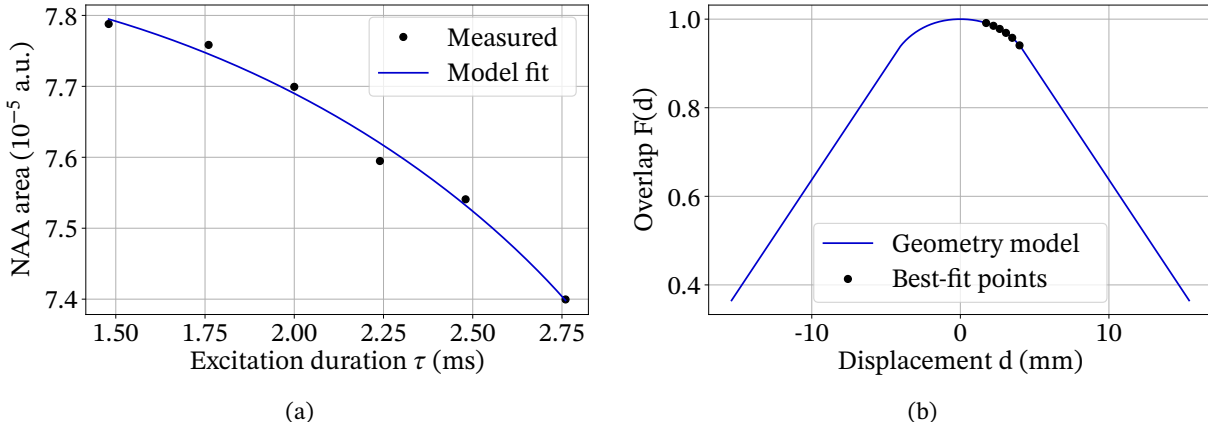


Figure 5.1: **CSDE fit:** (a) measured NAA areas (black) with scaled model (blue) derived in section 5.1 and (b) geometric CSDE model; black markers are the best-fit points obtained from (a); overlaying them shows where the solution lies in the design space and checks physical plausibility.

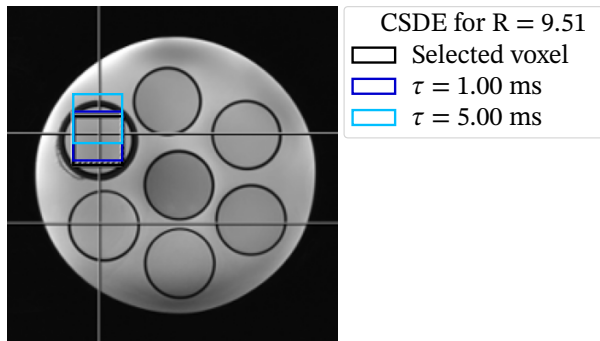


Figure 5.2: **Resulting CSDE:** selected voxel (black) with the actually measured NAA voxel for  $\tau = 1.00$  ms (blue) and  $\tau = 5.00$  ms (light blue), calculated with the measured R-value of 9.19.

with a bandwidth of 135 Hz and a water suppression delta frequency of 0.14 ppm. The spectra were averaged over 64 acquisitions and TE was 68 ms. I then fitted the peaks with special attention to the NAA peak while ignoring  $T_1$  and  $T_2$  effects, as they do not influence the comparison of the same metabolite measured at the same TR and TE.

**Result** The resulting NAA areas with the model scaled to fit the data are shown in figure 5.1a. The fits of the individual spectra are shown in the appendix in figure A.1. The fit yielded an R-value of 9.19. Figure 5.1b supports the physical plausibility of the fit with a plot of the best-fit points overlaying the overlap model calculated in section 5.1. With the obtained R-value I calculated the CSDE for NAA in the experiment and plotted the measured NAA voxels for  $\tau = 1.00$  ms and  $\tau = 5.00$  ms in figure 5.2.

**Discussion** The experiment showed that the CSDE does indeed depend on the excitation pulse duration  $\tau$  and that moderate  $\tau$  have low impact. In Deelchand et al. [31], the R-value for the 3 T measurement was chosen as 6.8, while the pulse shape was not mentioned. According to de Graaf [1, chap. 5], the measured R-value of 9.19 is within the realistic range of a SLR pulse.

Choosing a higher R-value for the 7 T implementation of the sequence is reasonable, as it reduces the stronger CSDE at higher field strengths.

While the model scales convincingly to the data, there are limitations that need to be considered: In the model, I assumed that the vials are perpendicular to the  $B_0$  field. However, as the vials are not perfectly aligned within the phantom and the phantom was only visually aligned in the coil, that is not exactly the case, which might cause a small error. Additionally, the slice profile is idealized in the model: Real RF pulses have finite transition bands and mild asymmetries, and off-resonance of NAA relative to water can change both the effective flip angle and the displacement. In spite of choosing moderate excitation pulse durations to avoid the  $B_0$  and  $B_1$  inhomogeneities at the water-air border, there might still be variations and gradient non-linearity that vary the spatial localization across the voxel.

Still, the fit provides a good estimate. It shows that if the excitation pulse duration is chosen just sufficient to achieve the desired flip angle, a percentage CSDE of approximately 10% is to be expected. Of course, the minimal excitation pulse duration depends on the individually calculated SAR limit. The calculated chemical shifts for the measured pulse duration range is listed in table 5.1. Therefore, in the GABA phantom, a voxel side length of 18 mm should not cause large errors in quantification due to the metabolite voxels being shifted outside the vial, while still being large enough to give good SNR.

Table 5.1: **Percentage CSDE** for different excitation durations  $\tau$ .

$\tau$ (ms)	1.5	1.8	2.0	2.2	2.5	2.8
CSDE	13.12	15.60	17.73	19.85	21.98	24.46

## 5.2 Phantom Measurements

As discussed in section 4.6 and section 4.7, it is necessary to perform  $T_1$  and  $T_2$  correction on the measured peak areas to allow comparison between metabolites. While many studies have been carried out to determine the metabolite-specific relaxation constants *in vivo*, the values in my phantoms may differ considerably (see subsection 2.3.4). Therefore, I measured these constants directly in my phantoms.

### 5.2.1 Measurement Challenges in the 2HG Phantom

While spectra acquired with phantom 2 were of high quality, spectra from phantom 3 exhibited severe baseline artifacts, which compromised quantification. The ripple artifact was present in every acquisition, but its exact shape and amplitude varied between measurements. I observed two main issues (see figure 5.3a):

Firstly, ripple artifacts appeared close to the water resonance, extending to approximately 3.5 ppm. With more averages, this ripple evolved into a frequency-dependent oscillation, increasing in frequency closer to the water resonance and strongly distorting the baseline. Secondly, in some spectral regions near the water resonance, the ripple amplitude exceeded that of the metabolite peaks, completely obscuring them.

As shown in figure 5.3b, those artifacts disappeared when the water suppression RF pulses were turned off. Therefore, they are likely linked to the water suppression sequence. Artificial ripples could only be reproduced intentionally by applying unrealistically short excitation pulses that were clipped by SAR limits, which the sequence warned about before scanning (see figure 5.3c). Those ripples then extended across the entire spectrum, suggesting that the issue may arise from clipped RF pulses during water suppression, which are not properly registered by the sequence.

I tested various sequence modifications, including adjustments of the VAPOR water suppression delays seven and eight, changes in the excitation flip angle, softening the gradient pulses, and prolongation of the acquisition delay. None of these adjustments eliminated the ripple artifacts. Increasing the echo time reduced the visible ripple amplitude but simultaneously attenuated the metabolite signals, making this approach impractical for quantification.

Since spectra acquired from phantom 2 only occasionally showed weak ripples outside the metabolite region, the stronger artifacts must be linked to properties that differ between the two phantoms.

The original phantom 3 differed from phantom 2 in several aspects: the orientation in the coil was changed, metabolite concentrations were adjusted, an additional metabolite (2HG) was included, and 0.1 mM copper sulfate (Copper(II) sulfate pentahydrate, Carl Roth, Karlsruhe, Germany; Cat.No. P024.1, CAS 7758-99-8) was added to prevent microbial growth.

Furthermore, I modified the vial fixation: in phantom 2, the vials were embedded in epoxy resin (BrilliantShine GlasKlar Epoxid Kunsthars Gießharz 750 ml, GTIN: 4031396140922) with less surrounding water, whereas in phantom 3 epoxy was applied only in the vial lids to prevent air bubbles.

To rule out the orientation in the coil, I put the phantom in a new container similar to that of phantom 2, which did not solve the problem. The most likely culprits are therefore either the copper sulfate and the epoxy resin. However, the measured relaxation times do not differ greatly from phantom 2 and conductivity was also not changed significantly.

As the exact origin of these artifacts could not be determined within the scope of this work, I tried to reduce the ripple during post processing by applying apodization to the FID before Fourier transformation. However, neither an exponential nor a shifted or unshifted sine-bell window was helpful, as the peaks were always weakened by the same factor as the ripple. Due to time constraints, I therefore decided to proceed with the phantom measurements.

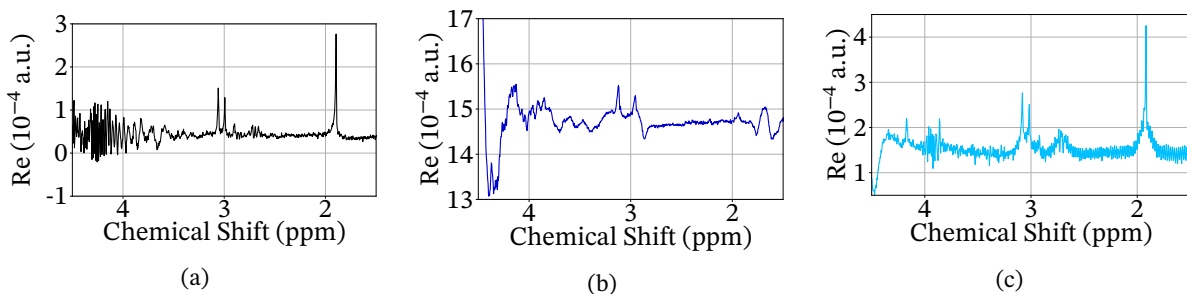


Figure 5.3: **Ripple in phantom 3:** (a) example spectrum with ripple, (b) spectrum without water suppression and (c) ripple caused by RF clipping.

## 5.2.2 Longitudinal Relaxation

First, I measured longitudinal relaxation, which characterizes the recovery of the net magnetization along the main magnetic field.  $T_1$  is a fundamental parameter influencing both contrast and quantification in MRS.

**Methods** For the GABA phantom, I measured the longitudinal relaxation by acquiring several spectra with the sLASER sequence, varying TR while keeping TE constant at 68 ms. Prior to the measurement, the phantom was heated to room temperature. Each acquisition used 64 averages, 2048 sampling points, and a dwell time of 454.6  $\mu$ s. I chose a voxel of  $18 \times 18 \times 18$  mm<sup>3</sup> in vial 1 with low GABA concentration. In this voxel, I investigated eight TR values from the minimal possible 1810 ms to 10000 ms, where  $T_1$  decay should be negligible. To simplify calculations, I kept the flip angle constant at 90°. Excitation and refocusing pulse durations were set to the minimum required for the chosen angles. Water suppression was achieved with VAPOR (bandwidth 135 Hz, delta position of -0.016 ppm). I fitted the spectra, extracted the metabolite areas, and then fitted them to the

longitudinal relaxation model described in subsection 2.3.1. The individual fits may be found in the appendix in figure A.2.

For a flip angle of 90°, the longitudinal magnetization is given by

$$M_z(\text{TR}) = M_0 \left(1 - e^{-\text{TR}/T_1}\right), \quad (5.12)$$

where  $M_0$  denotes the equilibrium magnetization, TR the repetition time, and  $T_1$  the longitudinal relaxation time.

I repeated the same measurement for the 2HG phantom, this time with 10 TR values between 1810 ms and 10000 ms. The spectral fits were more challenging due to baseline oscillations in the 2HG phantom, resulting in higher standard deviations of the fitted areas over  $T_1$ . The individual fits are shown in figure A.3.

**Result** Figure 5.4a shows the fit result for the two Cr peaks and the NAA and Cho peak in the GABA phantom. With the exception of the Cr-CH<sub>3</sub> peak, fits are of good quality with low standard deviations. The reduced reliability is due to the Cr-CH<sub>2</sub> peak's proximity to water, making it most affected by residual unsuppressed water. The results for the 2HG phantom (excluding the Cr-CH<sub>2</sub> peak) are shown in figure 5.4b.

The Cr-CH<sub>2</sub> peak was excluded because it was too obscured by baseline oscillations to be reliably identified, and the  $T_1$  constants of the other metabolites were determined with lower reliability than in the GABA phantom, quantified by higher standard deviations.

While the NAA fit yielded a small standard deviation, quantification became less reliable for peaks closer to water, as the baseline oscillations were likely caused by imperfect water suppression. The resulting decay constants and their standard deviations are listed in table 5.2, together with the in vivo literature values from table 2.1.

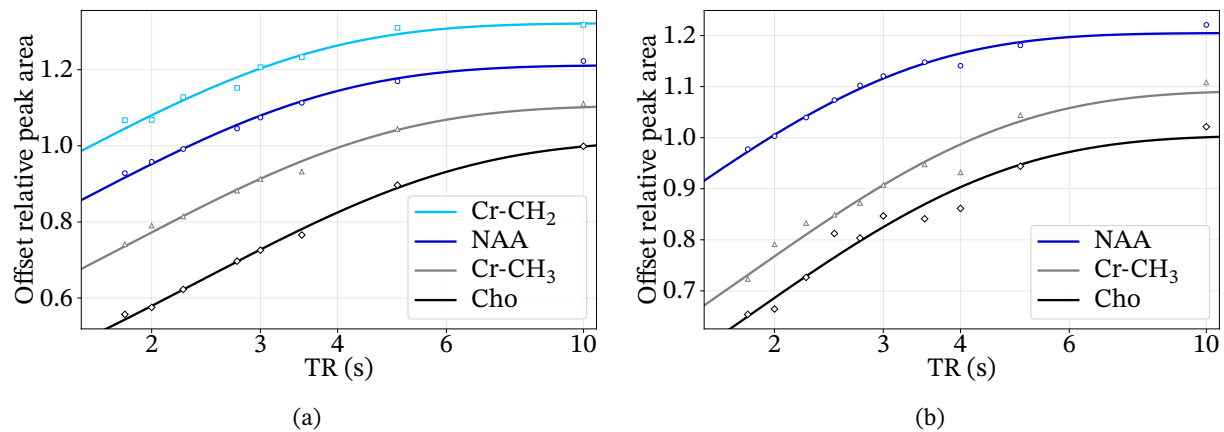


Figure 5.4: **T<sub>1</sub> fit:** measured peak areas and fit of Cr-CH<sub>2</sub> (light blue), NAA (blue), Cr-CH<sub>3</sub> (gray) and Cho in (a) the GABA phantom and (b) the 2HG phantom.

Table 5.2: **Comparison of T<sub>1</sub> relaxation times** between in vivo literature values at 7 T from table 2.1 and the phantom measurements; literature values are the average of WM and GM from table 2.1; errors of the measured values give the standard deviation of the non-linear least-squares fit.

Metabolite	In vivo (s)	GABA Phantom (s)	2HG Phantom (s)
NAA	$1.87 \pm 0.06$	$1.483 \pm 0.034$	$1.240 \pm 0.036$
Cr-CH <sub>2</sub>	$1.12 \pm 0.05$	$1.409 \pm 0.063$	-
Cr-CH <sub>3</sub>	$1.76 \pm 0.05$	$1.819 \pm 0.060$	$1.777 \pm 0.098$
Cho	$1.42 \pm 0.09$	$2.398 \pm 0.051$	$1.754 \pm 0.111$

**Discussion** The experiment showed the expected increased signal intensity for longer TR. Having taken into account the numerous differences between the human brain and my phantoms, I expected the  $T_1$  constants to be longer in my phantoms than in vivo (see subsection 2.3.4). However, this was only observed for Cr and Cho, with the measured  $T_1$  of Cho in the GABA phantom 69% higher than in vivo. This unexpectedly long  $T_1$  can likely be attributed to the absence of macro-molecular and membrane interactions that shorten relaxation in vivo.

In contrast, the longitudinal recovery of NAA in my phantoms was faster than in vivo. This may reflect the restricted mobility of NAA in vivo due to neuronal compartmentalization.

In the 2HG phantom, NAA showed the smallest standard deviation, consistent with its large chemical shift separation from water. This demonstrates the effect of copper sulfate that reduces NAA  $T_1$  by 27% compared to the GABA phantom.

The effect was smaller for Cr and may be even larger for Cho, although in this case, variations between measurement sets introduced greater uncertainty in the determined Cho  $T_1$ . This result should therefore be interpreted with caution. These findings highlight the necessity of applying phantom-specific  $T_1$  correction to ensure accurate metabolite quantification.

### 5.2.3 Transverse Relaxation

Like longitudinal relaxation, transverse relaxation might differ considerably from established in vivo values in my phantoms. Therefore, it is essential to determine  $T_2$  relaxation times in order to ensure accurate interpretation of the acquired spectra.

**Methods** To determine  $T_2$ , I used a debug loop type implemented in the sLASER sequence that acquires several spectra with varying TE within a given range. For the GABA phantom, I acquired 20 spectra with TEs evenly spaced between 68 ms and 1018 ms in an  $18 \times 18 \times 18$  mm<sup>3</sup> voxel. Each acquisition was averaged 32 times with 2048 sampling points, the dwell time was 454.6  $\mu$ s, and bandwidth 2200 Hz. I chose a flip angle of 81°, close to the Ernst angle for all metabolites of interest at the chosen TR of 3 s. Water was again suppressed with VAPOR with a frequency shift of -0.16 ppm, as the phantom was heated to room temperature before the measurement. Excitation and refocusing pulse durations were set to the minimum for the chosen angles.

I repeated the same measurement for the 2HG phantom with an increased number of averages (32) and TE values ranging from 48 ms to 1188 ms to facilitate the more challenging fit due to baseline oscillation.

I then fitted the individual spectra (see figure A.5 and figure A.6) and modeled them using the  $T_2$  decay equation from subsection 2.3.3:

$$M_{xy}(t) = M_{xy}(0) \cdot e^{-t/T_2}. \quad (5.13)$$

**Result** As in the  $T_1$  measurement, the Cr-CH<sub>2</sub> peak was too noisy for reliable fitting. This time, the problem also affected the GABA phantom, because at very long TEs (> 1 s) water suppression was insufficient. Correcting this would have required adapting water suppression for long TEs, which the debug loop type does not support. In phantom 3, the Cr-CH<sub>2</sub> peak was effectively lost in baseline oscillations. The results for the other three peaks are shown in figure 5.5 and the resulting concentrations with standard deviations, are listed in table 5.3, alongside averaged in vivo literature values (motor cortex/occipital lobe) from table 2.2.

Table 5.3: **Comparison of  $T_2$  relaxation times** between in vivo literature values at 7 T from table 2.2 and phantom 2 measurements; literature values are the average of occipital lobe and motor cortex from table 2.2.

Metabolite	In vivo (ms)	Phantom 2 (ms)	Phantom 3 (ms)
NAA	$150.0 \pm 4.2$	$893.8 \pm 37.4$	$866.4 \pm 15.8$
Cr-CH <sub>3</sub>	$104.0 \pm 1.8$	$721.0 \pm 78.1$	$542.6 \pm 73.0$
Cho	$145.5 \pm 4.7$	$599.4 \pm 30.9$	$691 \pm 169.4$

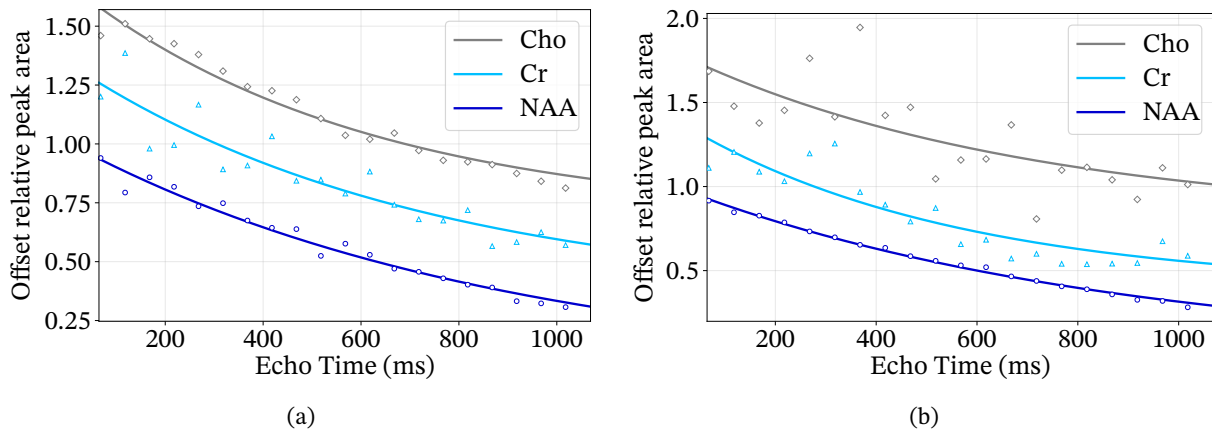


Figure 5.5:  **$T_2$  fit:** measured peak areas and fit of Cr-CH<sub>3</sub> (light blue), NAA (blue) and Cho (gray) in (a) phantom 2 and (b) phantom 3

**Discussion** The measurement confirmed that the peak areas decrease exponentially with TE.

As expected, the measured  $T_2$  constants were much longer than in vivo (see table 5.3). In phantom 2, Cr-CH<sub>3</sub> had the fastest transverse decay, but even then only 10.7% of the signal had decayed after 68 ms, the TE in most of my measurements. The NAA signal with the longest decay had lost 7.3% at that time. This means that the difference between the metabolites and therefore  $T_2$  decay correction is not significant in my measurements. This is fortunate as in the 2HG phantom, only NAA produced a good fit with slightly shorter  $T_2$  than in phantom 2. Cr-CH<sub>3</sub> and Cho deviated strongly from exponential decay due to baseline oscillation and insufficient water suppression. Since  $T_2$  is much larger than TE, slightly lower values than in the GABA phantom can be assumed or  $T_2$  correction omitted.

#### 5.2.4 SVS of NAA, Cr and Cho

After characterizing the relaxation properties of the phantoms, I proceeded to analyze the phantom measurements. First, I measured the peak areas of NAA and Cho from a single voxel in vial 1 of the GABA phantom relative to the Cr-CH<sub>3</sub> resonance and compared the resulting ratios to the nominal concentrations.

**Concentration Discrepancy** However, the quantification turned out to be challenging: even after  $T_1$  and  $T_2$  correction, the NAA/Cr-CH<sub>3</sub> and Cho/Cr-CH<sub>3</sub> ratios were systematically overestimated. Nevertheless, the results were internally consistent: the ratio of the two Cr peaks – which must logically be one when accounting for the number of contributing protons – was measured correctly with the improved localization of the sLASER sequence and  $T_1$  correction. Likewise, the NAA/Cho ratio was consistently close to the nominal value. These discrepancies indicated that the actual Cr concentration was likely lower than intended.

**Methods** To investigate this, I compared the determined ratios of several measurements at different dates and fitted the optimal Cr concentration. The measurement parameters and corresponding dates are listed in table 5.4. Figure 5.6 shows the comparison of the determined NAA/Cr-CH<sub>3</sub> Cho/Cr-CH<sub>3</sub> and Cr-CH<sub>3</sub>/Cr-CH<sub>2</sub> ratios. The individual fits are provided in the appendix (see figure A.7).

**Result** The first two measurements were performed with the mPRESS sequence and presaturation, which resulted in smaller Cr-CH<sub>2</sub> peaks. However, they show that the NAA/Cr and Cho/Cr ratios deviated from the nominal values from the beginning.

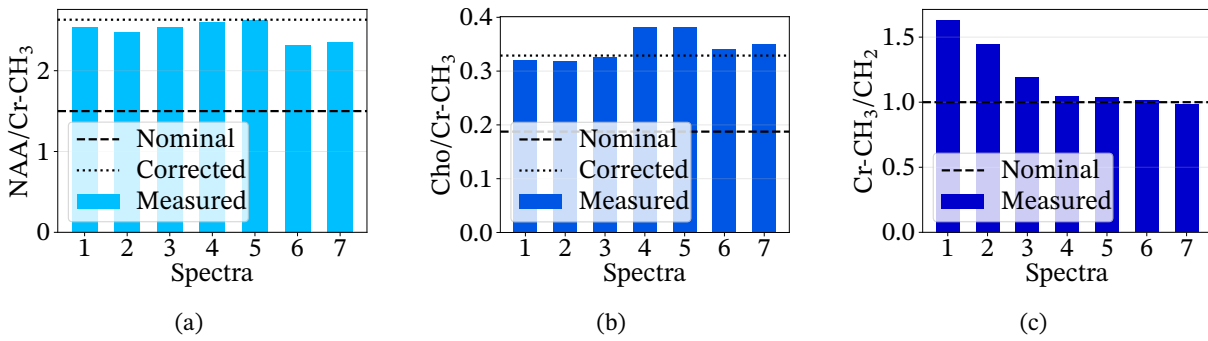


Figure 5.6: **SVS measurements in phantom 2:** comparison of different measurements; **(a)** ratio of NAA and Cr-CH<sub>3</sub>, **(b)** ratio of Cho and Cr-CH<sub>3</sub> and **(c)** ratio of Cr-CH<sub>3</sub> and Cr-CH<sub>2</sub>; the ratio given by the nominal Cr concentration (8 mM) is plotted, along with the ratio given by the best-fit Cr concentration (4.57 mM).

Table 5.4: **Overview of the spectra** fitted to compare concentration ratios in vial 1 of phantom 2. For each spectrum, TR, TE, number of averages, sequence, voxel side length, dwell time, excitation flip angle, vector size and date of acquisition are listed. All voxels were cubic.

	Spectra						
	1	2	3	4	5	6	7
TR (s)	2	2	3	3	3	2	10
TE (ms)	68	68	68	68	68	68	68
Averages	32	32	32	64	64	64	64
Sequence	mPRESS	mPRESS	sLASER	sLASER	sLASER	sLASER	sLASER
Voxel (mm)	15	15	18	20	20	18	18
Dwell Time ( $\mu$ s)	400	400	454.6	454.6	454.6	454.6	454.6
Flip Angle (°)	90	90	81	78	78	90	90
Vector Size	1024	1024	2048	2048	2048	2048	2048
Date	16.05.25	16.05.25	31.08.25	08.08.25	08.08.25	26.08.25	26.08.25

This suggests that the Cr concentration may not have been measured correctly in phantom preparation, indicating an actual concentration closer to 4.57 mM.

**Discussion** Even with the corrected Cr concentration, the ratios still varied across measurements. This might be due to the fact that even with the low GABA concentration, the Cr-CH<sub>3</sub> peak may have been partially reduced by overlap with an inverted GABA resonance, depending on J-coupling. As the measurements were taken at the same TE, this effect should, however, only have minor impact.

### 5.2.5 SVS J-Difference Editing of GABA

In addition to conventional SVS, I measured GABA with J-difference editing. The GABA resonances are all multiplets overlapping with stronger singlets and its in vivo concentration is low, making detection particularly challenging. As discussed in section 2.9, this method enables detection of the GABA resonance at 3.02 ppm by acquiring two spectra: one in which coupling partner at 1.89 ppm is selectively suppressed and one in which J-coupling is not hindered. For  $TE \approx (2J)^{-1}$ , this results in a maximum multiplet in the difference spectrum.

**Methods** The measurement was realized in phantom 2 with the msLASER sequence. In most vials, the GABA concentration was chosen very high to facilitate correct identification of the metabolite. However, such high GABA concentrations overshadow the Cr-CH<sub>3</sub> peak that is conventionally used as an internal reference. I therefore selected the two vials with the lowest GABA concentration for this measurement, vial 1 with high NAA and low Cho, representing healthy brain tissue, and vial 3 with low NAA and high Cr, mimicking glioma-like spectra. I acquired 2048 data points over a bandwidth of 2000 with 64 averages at  $TE = 68$  ms and  $TR = 3000$  ms with

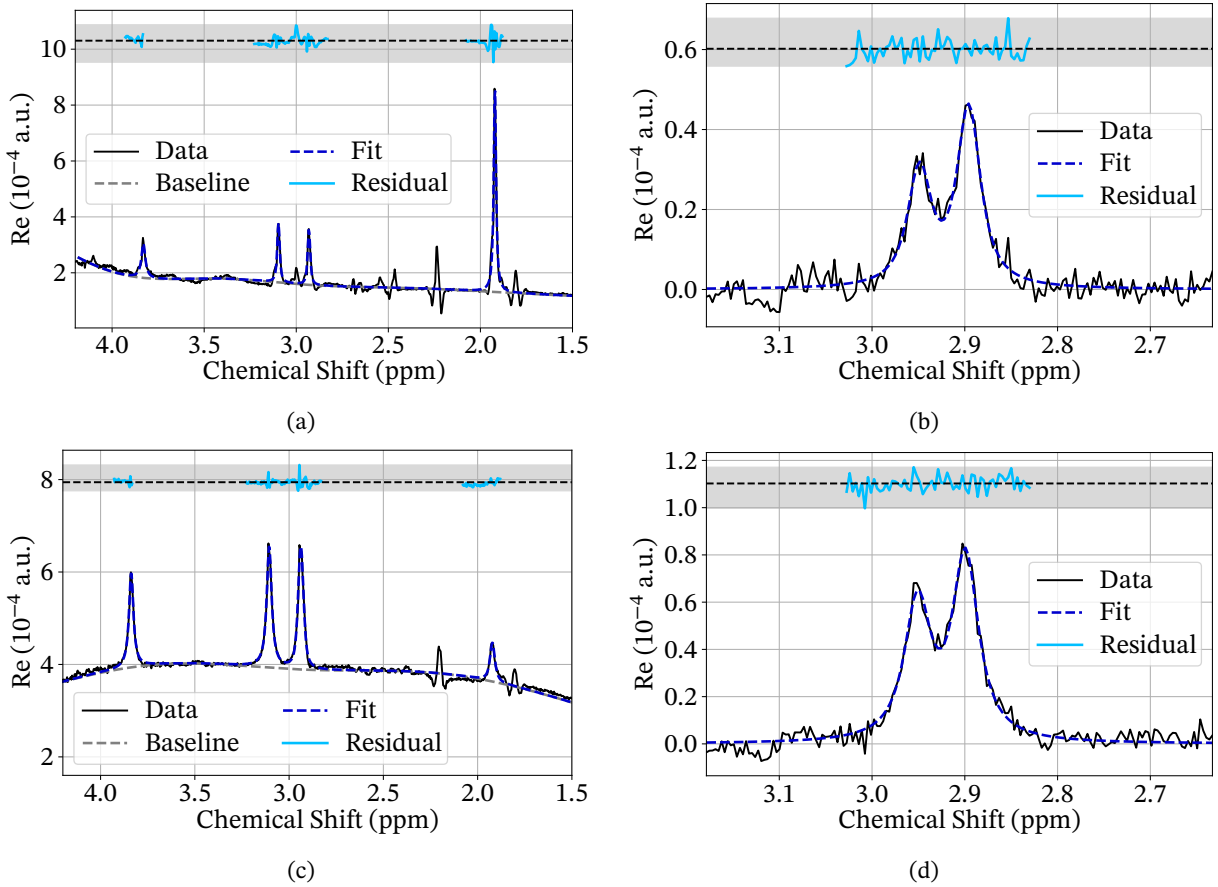


Figure 5.7: **GABA measurement in phantom 2, vials 1 and 3** (a) edit-off spectrum ( $\text{SNR} = 46.3$ ) and (b) difference spectrum ( $\text{SNR} = 20.4$ ) with fit (blue) and residuals (light blue) in vial 1; the GABA fit was done without a baseline, as it is automatically subtracted in the difference; (c) edit-off spectrum ( $\text{SNR} = 54.0$ ) and (d) difference spectrum ( $\text{SNR} = 29.1$ ) in vial 3 with fit (blue) and residuals (light blue).

the corresponding optimal flip angle for GABA,  $81^\circ$ , in a  $18 \times 18 \times 18\text{mm}^3$  voxel. The edit frequency was set to 1.73 ppm for the edit-ON spectrum as the phantom was at room temperature and to 9.00 ppm for the edit-OFF spectrum. The editing bandwidth was 150 Hz, as this led to a shorter editing pulse duration, allowing the desired TE. Water suppression was achieved with VAPOR over a bandwidth of 135 Hz with a shift of  $-0.16$  ppm. The center of all other pulses was shifted by  $-1.7$  ppm to optimize the GABA signal. In vial 1,  $B_0$  Shimming yielded a FWHM of 7.6 Hz in vial 1 and 13.7 Hz in vial 3.

**Result** Figure 5.7 (a) and (b) show the acquired edit-OFF and difference spectra in vial 1 with the fit and residuals. Panels (c) and (d) display the corresponding spectra from vial 3. The resulting metabolite ratios are summarized in table 5.5. In vial 1, the previously determined corrected Cr concentration was used for ratio calculation. In vial 3, however, the Cr concentration is close to the nominal one, supporting that the measured areas are accurate but the Cr concentration in the first vial was off. The ratios were  $T_1$  and  $T_2$  corrected using the experimentally determined values for NAA, Cr, and Cho. As the relaxation times for GABA could not be measured, I assumed values similar to those the other metabolites:  $T_1 = 1.6$  s and  $T_2 = 800$  ms.

**Discussion** The experiment showed that J-difference editing allows the separation of GABA in the difference spectrum. However, in contrast to the expected editing loss (see section 2.9), the measured GABA signal was substantially higher than the expected one with deviations of 93 % in vial 1 and 160 % in vial 3.

It is also interesting to note that the spectra were acquired at different  $B_0$  shims, which resulted in the expected

Table 5.5: **Comparison of nominal and measured concentrations** in units of Cr-CH<sub>3</sub>; Cr concentration corrected to 4.57 mM for vial 1.

Ratio	Vial 1			Vial 3		
	Nominal	Measured	Deviation	Nominal	Measured	Deviation
NAA/Cr-CH <sub>3</sub>	2.626	3.321	26%	0.375	0.286	-23%
Cho/Cr-CH <sub>3</sub>	0.328	0.407	24%	0.375	0.401	7%
Cr-CH <sub>3</sub> /Cr-CH <sub>2</sub>	1	1.42	42%	1	1.02	2%
GABA/Cr-CH <sub>3</sub>	0.5263	1.02	93%	0.31	0.84	160%

smaller peaks in the edit-OFF spectrum of vial 1. However, in the difference spectrum, the peaks seem to have roughly the same width. The wing-like distortions may be due to small residual frequency or phase drifts between the edit-ON and -OFF spectra. This also explains the overestimation of the GABA-to-Cr-CH<sub>3</sub> ratio. Alternatively, the overestimation could stem from unexpectedly high T<sub>1</sub> or unexpectedly low T<sub>2</sub> for GABA in the phantom.

### 5.2.6 SVS of 2HG

Despite the unexplained ripple in phantom 3 (see subsection 5.2.1), I proceeded with the detection of 2HG. As the measurement target of detecting 2HG with J-difference editing at 4.02 ppm was completely obscured by the ripple, which did not cancel in the difference spectrum, I therefore focused on detecting the resonance at 2.25 ppm without J-difference editing.

As summarized in Shams et al. [40], the sLASER sequence is more robust against field inhomogeneities and measurement artifacts, which is why they recommend it for clinical application. The difficulty is that the signal at 2.25 ppm overlaps with GABA, preventing unambiguous attribution to 2HG. For this reason, a comparison between the ratios measured with sLASER and msLASER would have been more informative.

**Methods** Where possible, I followed the parameter choices of Emir et al. [41], who compared 2HG detection using sLASER and msLASER and recommended sLASER for clinical implementation because of its robustness against field inhomogeneities and measurement artifacts. Accordingly, I used a TR of 5 s, a TE of 110 ms and an excitation flip angle of 90°. I acquired 64 averages over 2048 sampling points in an 18 × 18 × 18 mm<sup>3</sup> voxel placed in vial 6 of phantom 3, which contained NAA and Cho concentrations mimicking glioma tissue, a low GABA concentration and a higher 2HG concentration (3 mM). Water suppression was performed with VAPOR (bandwidth 135 Hz, frequency shift -0.12 ppm).

**Result** The acquired spectrum is shown in figure 5.8, along with the fit and the residuals. The double peak at 2.25 ppm (observed at 2.18 ppm due to the water resonance shift) is small but clearly visible.

The fitted areas were then T<sub>1</sub> and T<sub>2</sub> corrected using the values measured for phantom 3 when available and reliable. As the T<sub>1</sub> of Cr-CH<sub>2</sub> and 2HG could not be determined, I assumed the T<sub>1</sub> of Cr-CH<sub>2</sub> to be slightly lower than in phantom 1, consistent with the behavior of the other peaks, and set T<sub>1</sub> = 1.4 s. For 2HG, I inferred from in vivo literature values reported for glutamate and chose T<sub>1</sub> = 1.78 s, close to Cr-CH<sub>2</sub>.

I proceeded similarly with the T<sub>2</sub> values. Here, only the T<sub>2</sub> of NAA could be determined with acceptable certainty, giving a slightly faster decay than in phantom 2. Therefore, I set T<sub>2</sub> = 0.7 s for both Cr peaks and 2HG and T<sub>2</sub> = 0.69 for Cho since that fit contained several outliers but yielded a plausible estimate. In any case, the spectrum was acquired at long TR and transversal relaxation is slow in the phantoms, so the precise choice of values has little impact. Table 5.6 lists the thus determined concentration ratios. In spite of the ripple, the ratios of NAA, Cho and Cr-CH<sub>2</sub> to Cr-CH<sub>3</sub> are quite accurate. The concentration ratio of 2HG, however, is underestimated by 53% of the nominal one. This is not surprising as the 2HG resonance nearly disappears in the noise.

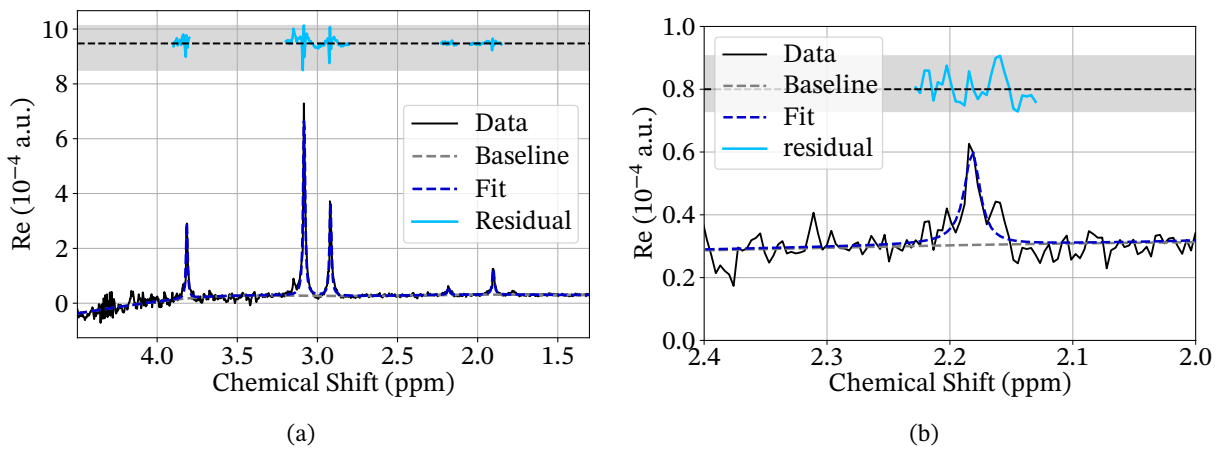


Figure 5.8: **2HG measurement in phantom 3, vial 6:** acquired spectrum (black), with fit (blue), baseline (gray) and residuals (light blue); **(a)** whole spectrum and **(b)** zoom on 2HG region; SNR of the Cr-CH<sub>3</sub> peak was 36.5 not considering the ripple.

Table 5.6: **Comparison of nominal and measured concentration** in units of Cr-CH<sub>3</sub>; T<sub>1</sub> and T<sub>2</sub> corrected

Ratio	Nominal	Measured	Deviation
NAA / Cr-CH <sub>3</sub>	0.3	0.28	-7%
Cho / Cr-CH <sub>3</sub>	0.6	0.65	8%
Cr-CH <sub>3</sub> / Cr-CH <sub>2</sub>	1	1.004	0.4%
2HG / Cr-CH <sub>3</sub>	0.3	0.14	-53%

**Discussion** The measured 2HG resonance lies close to the GABA resonance at 2.28 ppm. Although the GABA concentration in this vial (1.5 mM) was smaller than that of 2HG (3 mM), and GABA exhibits faster T<sub>2</sub> decay, it cannot be ruled out that part of the peak in fact stems from GABA.

### 5.3 In Vivo Measurements

The phantom measurements were challenging due to unknown phantom properties such as relaxation and due to the fact water suppression had been optimized for in vivo use. In addition, the GABA phantom contained unrealistically high GABA concentrations. Phantoms were nevertheless essential to verify concentration ratios, but the measurement is less challenging and more accurate in vivo. I therefore performed measurements on three healthy volunteers. This section presents the results for one of the volunteers (male, 24 years).

#### 5.3.1 SVS of NAA, Cr and Cho

First, I acquired SVS spectra with the msLASER sequence, one with a large voxel ( $30 \times 30 \times 30 \text{ mm}^3$ ) in the left hemisphere (see figure 5.9a and figure 5.9b) to ensure accurate GABA detection and one with a smaller voxel ( $20 \times 20 \times 20 \text{ mm}^3$ ) in the right hemisphere (see figure 5.10a and figure 5.10b). Both were placed in the anterior cingulate and largely dominated by white matter.

**Methods** In each voxel, I acquired an edit-OFF and edit-ON spectrum with the msLASER sequence at TR= 3 s with 64 averages over 2048 data points and bandwidth 2200 Hz.

Because of SAR limits, the excitation and refocusing pulse duration could not be shortened enough to achieve a TE below 70.48 ms. Reaching this TE could only be achieved by broadening the edit bandwidth from the usual 62 Hz to 150 Hz. Further increasing the edit bandwidth would have risked contaminating the difference spectrum.

Water and fat were suppressed with VAPOR water suppression over a bandwidth of 135 Hz. The water suppression frequency was not shifted, as the measurement was performed at body temperature. The fat suppression frequency shift was set to  $-3.4$  ppm. Accordingly, 1.9 ppm was chosen as the edit target frequency for the edit-ON and 9.0 ppm for the edit-OFF spectrum.

The fitted areas were relaxation corrected with the white matter literature  $T_1$  values from table 2.1 and the occipital lobe  $T_2$  values from table 2.2.

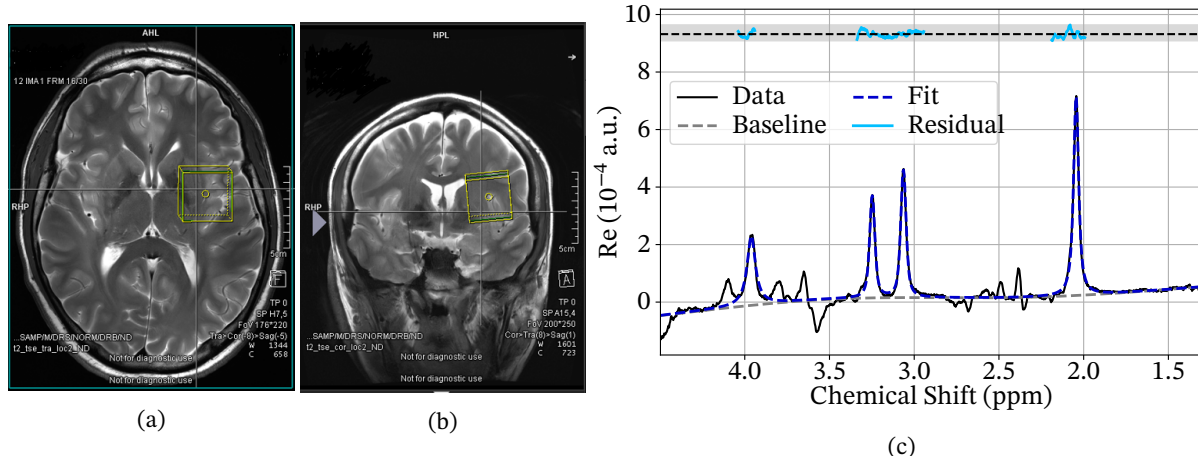


Figure 5.9: **First SVS measurement in vivo:** transversal (a) and coronal (b) view of the voxel selected in  $T_2$ -weighted localizer images with the resulting fitted spectrum (c).

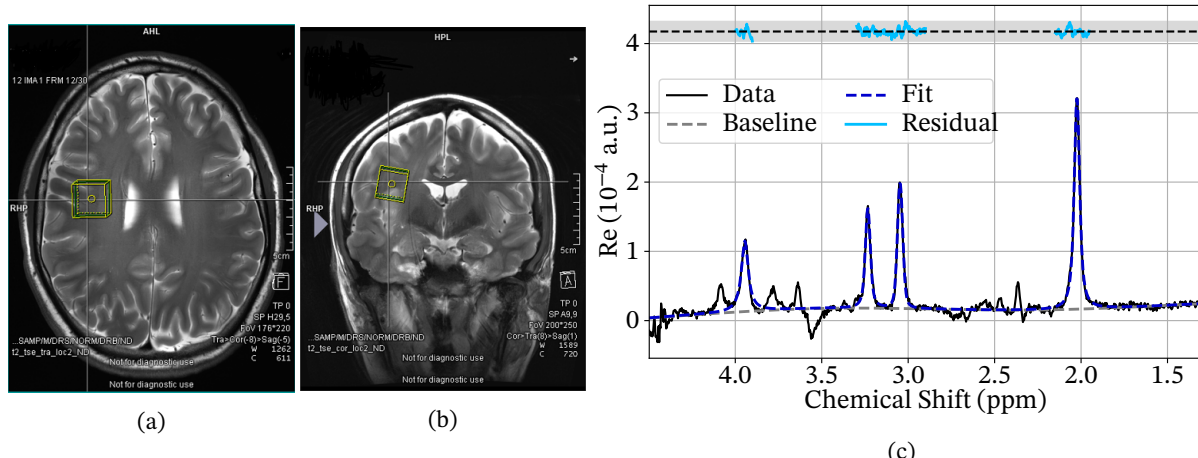


Figure 5.10: **Second SVS measurement in vivo:** transversal (a) and coronal (b) view of the voxel selected in  $T_2$ -weighted localizer images with the resulting fitted spectrum (c).

**Result** Figure 5.9c and figure 5.10c show the acquired edit-off spectra along with fit and residuals. As expected, the residuals in the peak areas are significantly smaller than in previous phantom experiments, as the pulses are more symmetric. Of course, several smaller resonances such as glutamate, glutamine and GABA are ignored in the fit, causing the Cr-CH<sub>2</sub> peak to be overestimated. The determined areas and the SNR of the Cr-CH<sub>3</sub> peak are printed in table 5.7.

**Discussion** Since the two spectra were acquired in similar, though contralateral, brain regions, the metabolite ratios are expected to be similar. This expectation was confirmed by the measurements. The NAA/Cr and Cho/Cr ratios fall within the expected range that for healthy brain tissue. The Cr-CH<sub>2</sub> peak is overestimated, resulting in a ratio larger than one. This could be corrected including the overlapping peaks in the model.

Table 5.7: **In vivo concentration ratios:** measured ratios of the two spectra after  $T_1$  correction with white matter values from table 2.1 and  $T_2$  correction with occipital lobe values from table 2.2; spectrum, voxel side length (mm) of the cubic voxel, concentration ratios of the  $\text{Cr}-\text{CH}_3$  peak and SNR are given.

Spectrum	Voxel	NAA	Cho	$\text{Cr}-\text{CH}_3$	SNR
1	30	1.35	0.18	1.45	86.34
2	20	1.71	0.19	1.39	66.4

### 5.3.2 J-Difference Editing of GABA

In the same measurement, I also acquired edit-ON spectra to detect GABA.

**Result** The phase-corrected difference spectra together with the corresponding fits and residuals for both measurements are shown in figure 5.11. The resulting concentrations expressed relative to  $\text{Cr}-\text{CH}_3$ , as well as the SNR of the GABA multiplet in the difference spectrum are summarized in table 5.8.

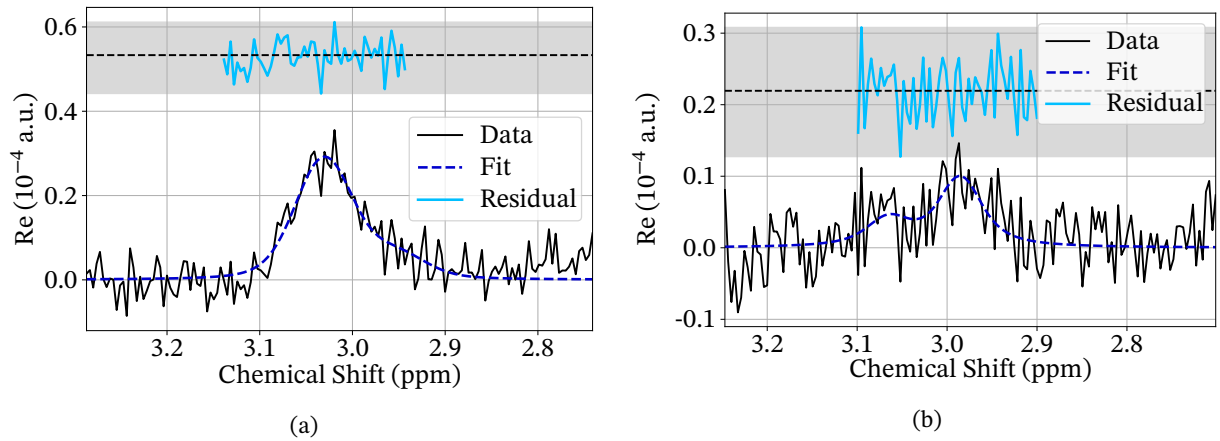


Figure 5.11: **GABA measurement in the two in vivo spectra:** difference spectra in the bigger (SNR = 9.86) (a) and smaller (SNR = 4.12) (b) voxel with the fit (blue) and residuals (light blue). The GABA fit was done without a baseline, as it is automatically subtracted in the difference.

Table 5.8: **In vivo concentration ratios:** measured ratios of the two spectra after  $T_1$  correction with white matter values from table 2.1 and  $T_2$  correction with occipital lobe values from table 2.2; spectrum, voxel side length (mm) of the cubic voxel, concentration ratios of the  $\text{Cr}-\text{CH}_3$  peak and SNR are given.

Spectrum	Voxel	GABA	SNR
1	30	0.12	9.86
2	20	0.13	4.12

**Discussion** Both measurements yielded the same ratio, even though the SNR for the smaller voxel was only just above the tolerable limit. However, as the residuals seemed to be free of structure, I still considered this result reliable. The determined in vivo concentrations fall within the expected range for healthy brain tissue. Evidently, editing was not hindered by the deviation of 2.48 ms from the optimal TE.

### 5.3.3 CSI of NAA, Cr and Cho

After the successful single-voxel measurements in vivo, I proceeded with multi-voxel spectroscopy on the same volunteer. This enables the simultaneous acquisition of spectra from multiple spatial locations, providing higher SNR compared to separate SVS spectra covering the same region acquired in the same measurement time.

**Methods** I acquired 2D CSI data in a healthy volunteer (male, 24 years) using an msLASER localized sequence with TR= 3020 ms and TE= 70.28 ms. The excitation flip angle was set to 72°, and the refocusing flip angle to 180°. Since the sequence was already long for a volunteer measurement, only 3 averages could be acquired. Water and lipids were suppressed with VAPOR (bandwidth 135 Hz). I chose an axial slice of thickness 20 mm; the field of view (FOV) was 180 × 160 mm<sup>2</sup> (A-P × R-L) with an 8 × 8 phase encoding matrix.

As the Cr concentration in the volunteer was unknown, I evaluated the NAA and Cho areas in units of the concentration in their voxel, weighted by the contributing protons and excluding all sub-voxels with a Cr-CH<sub>3</sub> SNR below four. The SNR map is plotted in figure 5.12c. I then plotted the resulting concentration ratios as colormaps and overlaid them on a T<sub>2</sub>-weighted localizer image from the acquisition. The individual fits are provided in the appendix in figure A.8.

**Result** The result is shown in figure 5.12. The heatmap of SNR distribution shows that the signal intensities form a cross-shaped pattern, with central voxels showing higher signals, while corner voxels are not being plotted due to low SNR, which appears anatomically unrealistic.

This pattern likely arises from the point-spread function of the finite 2D CSI grid, which causes the intensities to be sinc modulated after the 2D Fourier transformation automatically performed by the scanner. The sinc shaped sidelobes of the rectangular k-space sampling produce stronger contributions along the central axes. This effect may be mitigated by applying a Hanning window in k-space, which suppresses the side lobes of the point spread function and reduces the side lobes of the cross pattern. However, this also leads to a loss of spatial resolution and signal intensity – unfortunate given that the SNR is already relatively low due to the small number of averages. The sequence provides an option to apply a Hanning filter, but time constraints prevented optimization of the filter percentage.

The observed intensity distribution might also result from imperfect localization. In the CSI msLASER sequence, only the shim volume is displayed during planning, while the actual voxel grid is not shown. I therefore planned the acquisition using a product CSI sequence and copied the parameters. I then verified that shim and measurement volume were aligned in position and orientation. While this confirmed that the measurement was performed in the correct location, the absence of a displayed voxel grid still raises doubts.

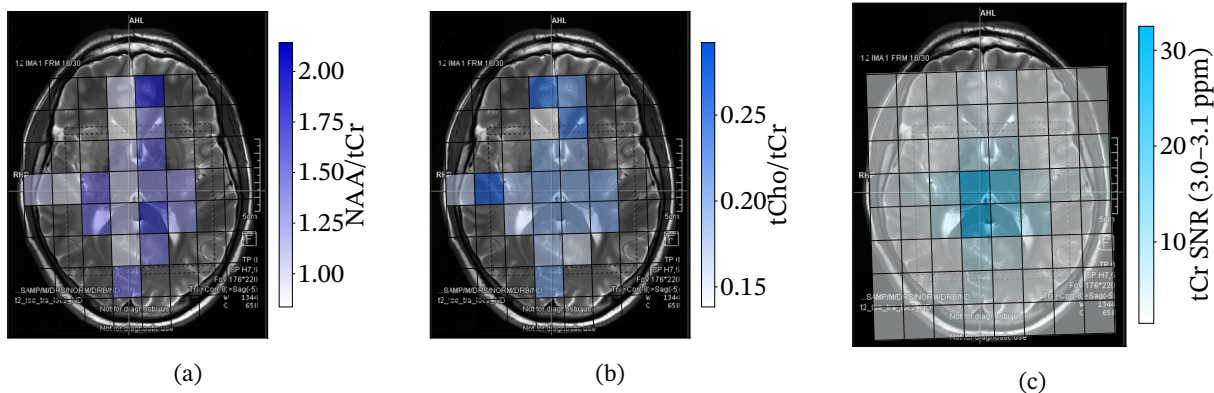


Figure 5.12: **CSI measurement in vivo:** distribution of (a) NAA and (b) Cho in units of Cr-CH<sub>3</sub> in their voxel and (c) SNR with the peak window it was calculated in; spectra with SNR below 4 were excluded from the ratio comparison.

**Discussion** The heatmaps show varying NAA and Cho ratios across the brain, with NAA at approximately 1.5 – 2.5 times and Cho at 0.1 – 0.3 times the Cr concentration. This lies within the expected range, but to reveal anatomical detail, a much higher resolution would be required – at the cost of reduced SNR. While this might still be acceptable in the high-intensity central region, the outer regions would completely fall below the SNR threshold. Although longer TR and additional averages could improve the situation, the present measurement

already exceeded 20 min, making this approach unsuitable for clinical use.

### 5.3.4 CSI of GABA

In the same measurement, I also acquired edit-ON spectra for GABA detection, using an edit bandwidth of 150 Hz with pulses centered at 1.9 ppm (edit-ON) and 9.0 ppm (edit-OFF).

**Result** The resulting SNR of the GABA multiplet in the difference spectrum and its ratio to Cr-CH<sub>3</sub> are shown in figure 5.13. Due to the limited number of averages and the small sub-voxels, only very few voxels reached sufficient SNR for quantification.

Those few voxels that did reach sufficient SNR showed implausible variation of GABA content between neighboring voxels and some yielded overall unrealistically high GABA concentrations. The individual fits are plotted in figure A.9.

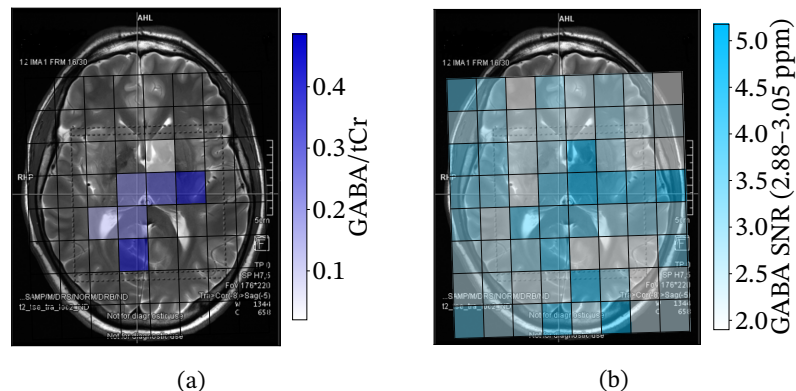


**Figure 5.13: CSI measurement in vivo:** distribution of (a) GABA in units of Cr in its voxel and (b) SNR with the peak window it was calculated in; spectra with SNR below 4 were excluded from the ratio comparison.

**Discussion** This confirms that the GABA concentration in the brain is too low for the multiplet to be detected reliably with CSI at clinically acceptable measurement times, even when using J-difference editing. If only a single spectrum had to be acquired instead of two, each average would take significantly less time, allowing both the number of averages and the TR to be increased. This would markedly improve the SNR of NAA, Cr, and Cho. In combination with a Hanning filter, this could enable the acquisition of more informative CSI maps for these metabolites.

# Chapter 6

## Conclusion and Outlook

In this project, I investigated several MRS detection methods for metabolites in the human brain at 7 T with a peak-based quantification workflow. The preliminary phantom measurements intended for practice and calibration turned out to be the main source of difficulty.

In the GABA phantom, a compounding error in mixing one vial led to concentration ratios that differed from the intended values, initially causing confusion. Nevertheless, the resulting ratios were internally consistent and stable across measurements, indicating that the measurement and post-processing pipeline was reliable.

Further complications arose from phantom properties deviating from well-known *in vivo* conditions. In particular, temperature-dependent chemical shifts and unknown relaxation times introduced the need for separate measurements before meaningful quantification was possible.

With these in hand, NAA, Cr-CH<sub>3</sub>, and Cho were reliably detected in conventional spectra and GABA was measured using spectral editing. The edited GABA concentrations tended to be higher than expected, which is probably due to slight frequency or phase misalignment between edit-ON and edit-OFF acquisitions.

In the final 2HG phantom, an unexplained artifact obscured the resonances intended as the measurement target. Conventional (non-edited) detection of 2HG was still possible, although the concentration could not be determined precisely due to low SNR and the fact that part of the detected signal might originate from GABA.

These problems did not occur in the final *in vivo* SVS measurements, where the ratios of NAA, Cr, Cho, and GABA fell within realistic ranges for healthy tissue. One notable limitation emerged: modeling each resonance as an isolated peak without strong overlap proved too simple for exact quantification of the overlapping Cr-CH<sub>2</sub> resonance.

Finally, I also explored CSI. The maps yielded reasonable results for the singlet resonances (NAA, Cr-CH<sub>3</sub>, and Cho), but snr was limited and intensity exhibited a cross pattern. This artifact may have been caused either by sinc modulation through rectangular k-space sampling or a slice-positioning error due to a bug in the sequence. The first issue could be mitigated by a strong k-space window (e.g., Hanning) and extending the acquisition time at the cost of spatial resolution and scan time. For GABA, even with J-difference-editing, the low subvoxel-wise SNR and doubled acquisition time render CSI impractical for clinical use.

In the case of 2HG, *in vivo* measurements had been planned but could not be realized during the time of this thesis since the metabolite is only present in low-grade gliomas, making it difficult to find potential candidates. Overall, the simple peak-modeling approach proved effective for the core metabolites and demonstrated that even without a full basis-set tool chain, robust quantification at 7 T is feasible. For exact quantification, basis-set fitting would likely yield higher accuracy, as it takes the entire spectrum into account rather than modeling individual peaks, making it the more reliable approach.

The overestimation of GABA in spectral editing could be mitigated through frequency alignment between sub-spectra, which would suppress the wings in the difference spectra.

For CSI, the initial maps already showed reasonable results for singlet resonances, and further improvements may be achieved through k-space filtering and longer acquisition times.

Finally, the ripple artifact observed in the 2HG phantom represents a technical anomaly the origin of which could not be identified within the scope of this project. Future work may explore its cause, for example by attempting to reproduce the effect in the GABA phantom, constructing alternative phantoms without copper sulfate or epoxy, or testing post-processing strategies with model FIDs. While not critical for metabolite quantification, resolving this artifact could provide useful insights into phantom design and spectral reliability.

# List of Figures

2.1	<b>NAA:</b> (a) Line-angle formula sketched with chemfig after de Graaf [1, chap. 2] with the methyl group causing the 2.01 ppm resonance circled and (b) simulated basisset at $TE = 30$ ms by Landheer, Swanberg, and Juchem [2]. . . . .	10
2.2	<b>Cr:</b> (a) Line-angle formula sketched with chemfig after de Graaf [1, chap. 2] with the methyl and methylene group causing the 3.03 ppm and 3.93 ppm resonances circled and (b) simulated basisset at $TE = 30$ ms by Landheer, Swanberg, and Juchem [2]. . . . .	11
2.3	<b>Cho:</b> (a) Line-angle formula sketched with chemfig after de Graaf [1, chap. 2] with the three methyl groups causing the 3.2 ppm resonance circled and (b) simulated basisset at $TE = 30$ ms by Landheer, Swanberg, and Juchem [2]. . . . .	12
2.4	<b>GABA:</b> (a) Line-angle formula sketched with chemfig after de Graaf [1, chap. 2] with the three methylene groups causing the 2.28 ppm, 3.00 ppm and 1.89 ppm resonances circled and (b) simulated basisset at $TE = 30$ ms by Landheer, Swanberg, and Juchem [2]. . . . .	12
2.5	<b>2HG:</b> (a) Line-angle formula sketched with chemfig after de Graaf [1, chap. 2] with the three proton groups causing the 4.01 ppm, 1.90 ppm and 2.25 ppm resonances circled and (b) simulated basisset at $TE = 30$ ms by Landheer, Swanberg, and Juchem [2]. . . . .	13
2.6	<b>Voigt profile:</b> (a) Comparison of Gaussian, Lorentzian and Voigt profiles with normalized amplitude, $\sigma = 1$ and $\gamma = 1$ ; (b) Convergence of the Voigt Profile to a Lorentzian for $\sigma \rightarrow 0$ and Gaussian for $\gamma \rightarrow 0$ ; quantified by the RSMD, calculated as $RSMD = \sqrt{\frac{1}{N} \sum_{i=1}^N (f_i - g_i)^2}$ , where $f_i$ and $g_i$ are the sampled values of the two functions at $N$ points. . . . .	21
2.7	<b>PRESS sequence diagram:</b> RF pulse outlines with slice-select gradients (white) and crusher gradients (gray), figure created with mrseqdia [23] after de Graaf [1, chap. 6]; the spins are excited with a 90° pulse accompanied by a slice-select gradient and refocused with two 180° refocusing pulses, each with a slice-select gradient in one spatial direction and flanked by two crusher gradients in the other. . . . .	25
2.8	<b>LASER sequence diagram:</b> RF pulse outlines with slice-select gradients (white) and crusher gradients (gray), figure created with mrseqdia [23] after de Graaf [1, chap. 6]; the spins are excited with a nonselective 90° pulse and refocused with two pairs of AFP pulses, each with a slice-select gradient in one spatial direction and flanked by two crusher gradients in another. . . . .	25
2.9	<b>Semi-LASER sequence diagram:</b> RF pulse outlines with slice-select gradients (white) and crusher gradients (gray), figure created with mrseqdia [23] after de Graaf [1, chap. 6]; the spins are excited with a slice selective 90° pulse accompanied by a slice-select gradient and refocused with two pairs of AFP refocusing pulses, each with a slice-select gradient in one spatial direction and flanked by two crusher gradients in the other. . . . .	26

2.10	<b>MEGA water suppression:</b> All metabolites including water are excited with a non-selective 90° excitation pulse and are then subjected to two orthogonal magnetic field gradients. While the other metabolites experience only one refocusing pulse between two equal gradients, an additional frequency-selective refocusing pulse (180° (S)) dephases only the water magnetization in the transverse plane; figure created with <code>mrseqdia</code> [23] after de Graaf [1, chap. 6]. . . . .	28
2.11	<b>MEGA PRESS sequence diagram:</b> PRESS sequence with an additional frequency-selective refocusing pulse between each pair of crusher gradients (gray); refocusing cancels only for the selected frequency of the editing target; figure created with <code>mrseqdia</code> [23] after de Graaf [1, chap. 8].	29
2.12	<b>MEGA semi-LASER sequence diagram:</b> sLASER sequence with an additional frequency-selective refocusing pulse between each pair of crusher gradients (gray); refocusing cancels only for the selected frequency of the editing target; figure created with <code>mrseqdia</code> [23] after de Graaf [1, chap. 8].	29
3.1	<b>Sketches of my phantoms:</b> (a) phantom 1 for practicing, (b) phantom 2 for GABA and (c) phantom 3 for 2HG. . . . .	30
3.2	<b>Comparison of water suppression methods:</b> presaturation (black) and WET (blue) measured with the Siemens PRESS sequence and VAPOR (light blue) with the sLASER sequence; (a) whole spectrum and (b) zoom on metabolite peaks; offset and scaled to the Cr-CH <sub>3</sub> amplitude. . . . .	33
3.3	<b>Temperature dependence of the edit frequency:</b> three difference spectra acquired at approximately 16 °C with three different edit frequencies; 1.9 ppm (light blue), 1.73 ppm (blue) and 1.6 ppm (black); the edit bandwidth visualized with a gray background; the calculated edit frequency clearly covers the editing target the best. . . . .	33
4.1	<b>Comparison of Lorentz and Voigt fit:</b> mean squared residual of the fit with Lorentz peaks (light blue) and with Voigt peaks (blue); residuals given in units of the Cr amplitude to ensure comparability. . . . .	37
4.2	<b>Phase shift:</b> Effect of zero- (a) and first- (b) order phase shift on two simulated peaks. . . . .	38
4.3	<b>Comparison to LCModel:</b> phase-corrected spectrum (black) with the fit (blue), baseline (gray) and residuals (light blue) obtained from (a) my method and (b) LCModel. . . . .	41
5.1	<b>CSDE fit:</b> (a) measured NAA areas (black) with scaled model (blue) derived in section 5.1 and (b) geometric CSDE model; black markers are the best-fit points obtained from (a); overlaying them shows where the solution lies in the design space and checks physical plausibility. . . . .	44
5.2	<b>Resulting CSDE:</b> selected voxel (black) with the actually measured NAA voxel for $\tau = 1.00$ ms (blue) and $\tau = 5.00$ ms (light blue), calculated with the measured R-value of 9.19. . . . .	44
5.3	<b>Ripple in phantom 3:</b> (a) example spectrum with ripple, (b) spectrum without water suppression and (c) ripple caused by RF clipping. . . . .	46
5.4	<b>T<sub>1</sub> fit:</b> measured peak areas and fit of Cr-CH <sub>2</sub> (light blue), NAA (blue), Cr-CH <sub>3</sub> (gray) and Cho in (a) the GABA phantom and (b) the 2HG phantom. . . . .	47
5.5	<b>T<sub>2</sub> fit:</b> measured peak areas and fit of Cr-CH <sub>3</sub> (light blue), NAA (blue) and Cho (gray) in (a) phantom 2 and (b) phantom 3 . . . . .	49
5.6	<b>SVS measurements in phantom 2:</b> comparison of different measurements; (a) ratio of NAA and Cr-CH <sub>3</sub> , (b) ratio of Cho and Cr-CH <sub>3</sub> and (c) ratio of Cr-CH <sub>3</sub> and Cr-CH <sub>2</sub> ; the ratio given by the nominal Cr concentration (8 mM) is plotted, along with the ratio given by the best-fit Cr concentration (4.57 mM). . . . .	50
5.7	<b>GABA measurement in phantom 2, vials 1 and 3</b> (a) edit-off spectrum (SNR = 46.3) and (b) difference spectrum (SNR = 20.4) with fit (blue) and residuals (light blue) in vial 1; the GABA fit was done without a baseline, as it is automatically subtracted in the difference; (c) edit-off spectrum (SNR = 54.0) and (d) difference spectrum (SNR = 29.1) in vial 3 with fit (blue) and residuals (light blue). . . . .	51

5.8	<b>2HG measurement in phantom 3, vial 6:</b> acquired spectrum (black) with fit (blue), baseline (gray) and residuals (light blue); <b>(a)</b> whole spectrum and <b>(b)</b> zoom on 2HG region; SNR of the Cr-CH <sub>3</sub> peak was 36.5 not considering the ripple. . . . .	53
5.9	<b>First SVS measurement in vivo:</b> transversal <b>(a)</b> and coronal <b>(b)</b> view of the voxel selected in T <sub>2</sub> -weighted localizer images with the resulting fitted spectrum <b>(c)</b> . . . . .	54
5.10	<b>Second SVS measurement in vivo:</b> transversal <b>(a)</b> and coronal <b>(b)</b> view of the voxel selected in T <sub>2</sub> -weighted localizer images with the resulting fitted spectrum <b>(c)</b> . . . . .	54
5.11	<b>GABA measurement in the two in vivo spectra:</b> difference spectra in the bigger (SNR = 9.86) <b>(a)</b> and smaller (SNR = 4.12) <b>(b)</b> voxel with the fit (blue) and residuals (light blue). The GABA fit was done without a baseline, as it is automatically subtracted in the difference. . . . .	55
5.12	<b>CSI measurement in vivo:</b> distribution of <b>(a)</b> NAA and <b>(b)</b> Cho in units of Cr-CH <sub>3</sub> in their voxel and <b>(c)</b> SNR with the peak window it was calculated in; spectra with SNR below 4 were excluded from the ratio comparison. . . . .	56
5.13	<b>CSI measurement in vivo:</b> distribution of <b>(a)</b> GABA in units of Cr in its voxel and <b>(b)</b> SNR with the peak window it was calculated in; spectra with SNR below 4 were excluded from the ratio comparison. . . . .	57
A.1	<b>CSDE fits:</b> acquired spectrum (black) with fit (blue), baseline (gray) and residuals (light blue); excitation pulse duration given above. . . . .	67
A.2	<b>T<sub>1</sub> fits in the GABA phantom:</b> acquired spectrum (black) with fit (blue), baseline (gray) and residuals (light blue); TR given above. . . . .	68
A.3	<b>T<sub>1</sub> Fits in the 2HG phantom:</b> Acquired spectrum (black) with fit (blue), baseline (gray) and residuals (light blue); TR given above. . . . .	69
A.4	<b>Profile comparison fits:</b> acquired spectrum (black) with fit (blue), baseline (gray) and residuals (light blue); Peak model and index given above. . . . .	70
A.5	<b>T<sub>2</sub> fits in the GABA phantom:</b> acquired spectrum (black) with fit (blue), baseline (gray) and residuals (light blue); GABA was ignored in the fit as the transversal relaxation is complicated by j-modulation and therefore T <sub>2</sub> could not be determined; TE given above. . . . .	71
A.6	<b>T<sub>2</sub> fits in the 2HG phantom:</b> acquired spectrum (black) with fit (blue), baseline (gray) and residuals (light blue); GABA was ignored in the fit as the transversal relaxation is complicated by J-modulation and therefore T <sub>2</sub> could not be determined; TE given above. . . . .	72
A.7	<b>SVS fits of NAA, Cr and Cho:</b> Acquired spectrum (black) with fit (blue), baseline (gray) and residuals (light blue). . . . .	73
A.8	<b>CSI fits in vivo:</b> acquired spectrum (black with fit (blue), baseline (gray) and residuals (light blue); row and column in the scanner output given above. . . . .	74
A.9	<b>GABA CSI fits in vivo:</b> Acquired spectrum (black with fit (blue), baseline (gray) and residuals (light blue); row and column in the scanner output given above. . . . .	78

# List of Tables

2.1	<b>T<sub>1</sub> in vivo relaxation times:</b> Literature values at 7 T in occipital WM and GM. . . . .	17
2.2	<b>T<sub>2</sub> relaxation times at:</b> Literature values in the occipital lobe and motor cortex at 7 T. . . . .	18
3.1	<b>Phantom 1:</b> metabolite concentrations in mM, uncertainties reflect assumed preparation errors.	31
3.2	<b>Phantom 2:</b> metabolite concentrations in mM, uncertainties reflect assumed preparation errors.	31
3.3	<b>Phantom 3:</b> metabolite concentrations in mM, uncertainties reflect assumed preparation errors.	32
4.1	<b>Overview of the spectra fitted to compare Voigt and Lorentz peaks:</b> for each index, subject, region, sequence and voxel side length are listed; all voxels were cubic; the special column gives additional information on why the spectra were chosen for the comparison. . . . .	37
4.2	<b>Comparison to LCModel:</b> NAA/Cr and Cho/Cr ratio and global and linear phase obtained with my approach and with LCModel for the same spectrum; for my approach, the ratios are given in units of Cr-CH <sub>3</sub> and T <sub>1</sub> and T <sub>2</sub> corrected; the last column gives the deviation from LCModel for each parameter . . . . .	41
5.1	<b>Percentage CSDE</b> for different excitation durations $\tau$ . . . . .	45
5.2	<b>Comparison of T<sub>1</sub> relaxation times</b> between in vivo literature values at 7 T from table 2.1 and the phantom measurements; literature values are the average of WM and GM from table 2.1; errors of the measured values give the standard deviation of the non-linear least-squares fit. . . . .	47
5.3	<b>Comparison of T<sub>2</sub> relaxation times</b> between in vivo literature values at 7 T from table 2.2 and phantom 2 measurements; literature values are the average of occipital lobe and motor cortex from table 2.2. . . . .	48
5.4	<b>Overview of the spectra</b> fitted to compare concentration ratios in vial 1 of phantom 2. For each spectrum, TR, TE, number of averages, sequence, voxel side length, dwell time, excitation flip angle, vector size and date of acquisition are listed. All voxels were cubic. . . . .	50
5.5	<b>Comparison of nominal and measured concentrations</b> in units of Cr-CH <sub>3</sub> ; Cr concentration corrected to 4.57 mM for vial 1. . . . .	52
5.6	<b>Comparison of nominal and measured concentration</b> in units of Cr-CH <sub>3</sub> ; T <sub>1</sub> and T <sub>2</sub> corrected . . . . .	53
5.7	<b>In vivo concentration ratios:</b> measured ratios of the two spectra after T <sub>1</sub> correction with white matter values from table 2.1 and T <sub>2</sub> correction with occipital lobe values from table 2.2; spectrum, voxel side length (mm) of the cubic voxel, concentration ratios of the Cr-CH <sub>3</sub> peak and SNR are given. . . . .	55
5.8	<b>In vivo concentration ratios:</b> measured ratios of the two spectra after T <sub>1</sub> correction with white matter values from table 2.1 and T <sub>2</sub> correction with occipital lobe values from table 2.2; spectrum, voxel side length (mm) of the cubic voxel, concentration ratios of the Cr-CH <sub>3</sub> peak and SNR are given. . . . .	55

# Bibliography

- [1] Robin A. de Graaf. *In Vivo NMR Spectroscopy: Principles and Techniques*. 3rd ed. John Wiley & Sons, Ltd, 2019. ISBN: 9781119382461. DOI: 10.1002/9781119382461. URL: <https://onlinelibrary.wiley.com/doi/10.1002/9781119382461>.
- [2] Karl Landheer, Kelley M. Swanberg, and Christoph Juchem. “Magnetic resonance Spectrum simulator (MARSS), a novel software platform for fast and computationally efficient basis set simulation”. In: *NMR in Biomedicine* 34.e4129 (2021), e4129. DOI: 10.1002/nbm.4129. URL: <https://onlinelibrary.wiley.com/doi/full/10.1002/nbm.4129>.
- [3] Deanna L. Taylor et al. “Investigation into the Role of N-Acetylaspartate in Cerebral Osmoregulation”. In: *Journal of Neurochemistry* 65.1 (1995), pp. 275–281. DOI: 10.1046/j.1471-4159.1995.65010275.x. URL: <https://doi.org/10.1046/j.1471-4159.1995.65010275.x>.
- [4] Amedeo F. Jr. D’Adamo and Frank M. Yatsu. “Acetate Metabolism in the Nervous System. N-Acetyl-L-Aspartic Acid and the Biosynthesis of Brain Lipids”. In: *Journal of Neurochemistry* 13.10 (1966), pp. 961–965. DOI: 10.1111/j.1471-4159.1966.tb10292.x. URL: <https://doi.org/10.1046/j.1471-4159.1995.65010275.x>.
- [5] Amedeo F. Jr. D’Adamo and Ann P. D’Adamo. “Acetyl Transport Mechanisms in the Nervous System. The Oxoglutarate Shunt and Fatty Acid Synthesis in the Developing Rat Brain”. In: *Journal of Neurochemistry* 15.4 (1968), pp. 315–323. DOI: 10.1111/j.1471-4159.1968.tb11616.x.
- [6] R. D. Blakely and J. T. Coyle. “The neurobiology of N-acetylaspartyglutamate”. In: *International Review of Neurobiology*. Ed. by J. R. Smythies and R. Bradley. Vol. 30. International Review of Neurobiology. New York: Academic Press, 1988, pp. 39–100. DOI: 10.1016/S0074-7742(08)60046-X. URL: [https://doi.org/10.1016/S0074-7742\(08\)60046-X](https://doi.org/10.1016/S0074-7742(08)60046-X).
- [7] Ashley D. Harris et al. “Normalizing data from GABA-edited MEGA-PRESS implementations at 3 Tesla”. In: *Magnetic Resonance Imaging* 42.8 (2017). PMCID: PMC5581667, pp. 8–15. DOI: 10.1016/j.mri.2017.04.013. URL: <https://www.ncbi.nlm.nih.gov/pmc/articles/PMC5581667/>.
- [8] Lijing Xin et al. “Proton  $T_1$  relaxation times of metabolites in human occipital white and gray matter at 7 T”. In: *Magnetic Resonance in Medicine* 69.4 (2013), pp. 931–936. DOI: 10.1002/mrm.24352. URL: <https://doi.org/10.1002/mrm.24352>.
- [9] Yan Li et al. “T1 and T2 Metabolite Relaxation Times in Normal Brain at 3T and 7T”. In: *Journal of Molecular Imaging & Dynamics* S1 (2012). Open Access, p. 002. ISSN: 2155-9937. DOI: 10.4172/2155-9937.S1-002. URL: <https://doi.org/10.4172/2155-9937.S1-002>.
- [10] Nicholas A. J. Puts, Peter B. Barker, and Richard A. E. Edden. “Measuring the longitudinal relaxation time of GABA in vivo at 3 Tesla”. In: *Journal of Magnetic Resonance Imaging* 37.4 (2012), pp. 798–802. DOI: 10.1002/jmri.23817. URL: <https://doi.org/10.1002/jmri.23817>.
- [11] Małgorzata Marjańska et al. “Localized  $^1\text{H}$  NMR spectroscopy in different regions of human brain in vivo at 7 T: T2 relaxation times and concentrations of cerebral metabolites”. In: *NMR in Biomedicine* 25.2 (Feb. 2012), pp. 332–339. DOI: 10.1002/nbm.1754. URL: <https://doi.org/10.1002/nbm.1754>.

- [12] Jarunee Intrapromkul et al. “Determining the in vivo transverse relaxation time of GABA in the human brain at 7T”. In: *Journal of Magnetic Resonance Imaging* 38.5 (2013), pp. 1224–9. DOI: 10.1002/jmri.23979. URL: <https://doi.org/10.1002/jmri.23979>.
- [13] N. Bloembergen, E. M. Purcell, and R. V. Pound. “Relaxation Effects in Nuclear Magnetic Resonance Absorption”. In: *Phys. Rev.* 73 (7 Apr. 1948), pp. 679–712. DOI: 10.1103/PhysRev.73.679. URL: <https://link.aps.org/doi/10.1103/PhysRev.73.679>.
- [14] Johan Qvist et al. “Rotational dynamics in supercooled water from nuclear spin relaxation and molecular simulations”. In: *The Journal of Chemical Physics* 136.20 (May 28, 2012), p. 204505. DOI: 10.1063/1.4720941.
- [15] C. D. J. Sinclair et al. “Quantitative magnetization transfer in in vivo healthy human skeletal muscle at 3 T”. In: *Magnetic Resonance in Medicine* 64.6 (Dec. 2010), pp. 1739–1748. DOI: 10.1002/mrm.22562. URL: <https://doi.org/10.1002/mrm.22562>.
- [16] J. Glover. *MRI Questions and Answers*. Educational resource on magnetic resonance imaging. 2025. URL: <https://mriquestions.com/> (visited on 08/22/2025).
- [17] Kalaivani Thangavel and Emine Saritas. “Aqueous paramagnetic solutions for MRI phantoms at 3 T: A detailed study on relaxivities”. In: *Turkish Journal of Electrical Engineering & Computer Sciences* 25 (Jan. 2017), pp. 2108–2121. DOI: 10.3906/elk-1602-123.
- [18] Gisela E. Hagberg and Klaus Scheffler. “Effect of r1 and r2 relaxivity of gadolinium-based contrast agents on the T1-weighted MR signal at increasing magnetic field strengths”. In: *Contrast Media and Molecular Imaging* 8 (Nov. 2013), pp. 456–465. DOI: 10.1002/cmmi.1565.
- [19] I. Marshall et al. “Use of Voigt lineshape for quantification of in vivo  $^1\text{H}$  spectra”. In: *Magnetic Resonance in Medicine* 37.5 (May 1997), pp. 651–657. DOI: 10.1002/mrm.1910370504. PMID: 9126938. URL: <https://pubmed.ncbi.nlm.nih.gov/9126938/> (visited on 09/07/2025).
- [20] Jan Hellwig and Klaus Neymeyr. “On the uniqueness of continuous and discrete hard models of NMR-spectra”. In: *Journal of Mathematical Chemistry* 63.1 (2025), pp. 267–296. ISSN: 1572-8897. DOI: 10.1007/s10910-024-01673-x. URL: <https://doi.org/10.1007/s10910-024-01673-x>.
- [21] J. J. Olivero and R. L. Longbothum. “Empirical fits to the Voigt line width: A brief review”. In: *Journal of Quantitative Spectroscopy and Radiative Transfer* 17.2 (1977), pp. 233–236. ISSN: 0022-4073. DOI: 10.1016/0022-4073(77)90161-3. URL: <https://www.sciencedirect.com/science/article/pii/0022407377901613>.
- [22] Paul A. Bottomley. “Spatial localization in NMR spectroscopy in vivo”. In: *Annals of the New York Academy of Sciences* 508.1 (1987), pp. 333–348. DOI: 10.1111/j.1749-6632.1987.tb32915.x.
- [23] Max Diefenbach. *mrseqdia: LaTeX/TikZ package for MR pulse sequence diagrams*. LaTeX package file `mrseqdia.sty`. 2018.
- [24] Michael Garwood and Lance DelaBarre. “The return of the frequency sweep: Designing adiabatic pulses for contemporary NMR”. In: *Journal of Magnetic Resonance* 153.2 (2001), pp. 155–177. DOI: 10.1006/jmre.2001.2340.
- [25] Tom W. J. Scheenen et al. “Short echo time  $^1\text{H}$ -MRSI of the human brain at 3T with minimal chemical shift displacement errors using adiabatic refocusing pulses”. In: *Magnetic Resonance in Medicine* 59.1 (2008), pp. 1–6. DOI: 10.1002/mrm.21302.
- [26] A. Haase et al. “ $^1\text{H}$  NMR chemical shift selective (CHESS) imaging”. In: *Physics in Medicine & Biology* 30.4 (Apr. 1985), p. 341. DOI: 10.1088/0031-9155/30/4/008. URL: <https://dx.doi.org/10.1088/0031-9155/30/4/008>.

- [27] R. J. Ogg, R. B. Kingsley, and J. S. Taylor. “WET, a T1- and B1-insensitive water-suppression method for in vivo localized  $^1\text{H}$  NMR spectroscopy”. In: *Journal of Magnetic Resonance, Series B* 104.1 (1994), pp. 1–10. DOI: 10.1006/jmrb.1994.1048.
- [28] I. Tkáč et al. “In vivo  $^1\text{H}$  NMR spectroscopy of rat brain at 1 ms echo time”. In: *Magnetic Resonance in Medicine* 41.4 (1999), pp. 649–656. DOI: 10.1002/(SICI)1522-2594(199904)41:4<649::AID-MRM2>3.0.CO;2-G.
- [29] M. Mescher et al. “Solvent suppression using selective echo dephasing”. In: *Journal of Magnetic Resonance, Series A* 123.2 (1996), pp. 226–229. DOI: 10.1006/jmra.1996.0242.
- [30] Gülin Öz and Ivan Tkáč. “Short-echo, single-shot, full-intensity  $^1\text{H}$  MRS for neurochemical profiling at 4T: Validation in the cerebellum and brainstem”. In: *Magnetic Resonance in Medicine* 65.4 (2011), pp. 901–910. DOI: 10.1002/mrm.22708.
- [31] Dinesh K. Deelchand et al. “Across-vendor standardization of semi-LASER for single-voxel MRS at 3T”. In: *NMR in Biomedicine* 34.5 (2021), e4218. DOI: 10.1002/nbm.4218.
- [32] Ronald Corbett, Abbot Laptook, and Paul Weatherall. “Noninvasive Measurements of Human Brain Temperature Using Volume-Localized Proton Magnetic Resonance Spectroscopy”. In: *Journal of Cerebral Blood Flow & Metabolism* 17.4 (1997). PMID: 9143218, pp. 363–369. DOI: 10.1097/00004647-199704000-00001. URL: <https://doi.org/10.1097/00004647-199704000-00001>.
- [33] Johanna Link. *Bachelor’s Thesis Magnetic Resonance Spectroscopy*. Version 1.0. Accessed 2025-10-02. 2025. URL: [https://github.com/Johannaeve/bachelors\\_thesis\\_mrs.git](https://github.com/Johannaeve/bachelors_thesis_mrs.git).
- [34] NumPy Developers. *numpy.polynomial.chebyshev.chebval — NumPy v2.3 Manual*. <https://numpy.org/doc/stable/reference/generated/numpy.polynomial.chebyshev.chebval.html>. Accessed: 2025-10-01. 2025.
- [35] SciPy Developers. *scipy.interpolate.CubicSpline — SciPy v1.12.2 Reference Guide*. <https://docs.scipy.org/doc/scipy/reference/generated/scipy.interpolate.CubicSpline.html>. Accessed: 2025-10-01. 2025.
- [36] Simon Köppel. “A New Quantification Approach for Chemical Exchange Saturation Transfer MRI”. Manuscript in preparation. MA thesis. Friedrich-Alexander-Universität Erlangen-Nürnberg, 2025.
- [37] Ramon van Handel. *Probability in High Dimension. APC 550 Lecture Notes*. Princeton University. Dec. 21, 2016. URL: <https://web.math.princeton.edu/~rvan/APC550.pdf> (visited on 09/17/2025).
- [38] SciPy Developers. *scipy.optimize.curve\_fit — SciPy v1.11.3 Manual*. 2023. URL: [https://docs.scipy.org/doc/scipy/reference/generated/scipy.optimize.curve\\_fit.html](https://docs.scipy.org/doc/scipy/reference/generated/scipy.optimize.curve_fit.html) (visited on 09/17/2025).
- [39] Stephen W. Provencher. *LCModel & LCMgui User’s Manual*. Version 6.3-1R. Accessed: 2025-09-17. Feb. 2021. URL: <https://s-provencher.com/pub/LCModel/manual/manual.pdf>.
- [40] Zahra Shams et al. “Comparison of 2-Hydroxyglutarate Detection With sLASER and MEGA-sLASER at 7T”. In: *Frontiers in Neurology* 12 (2021), p. 718423. DOI: 10.3389/fneur.2021.718423. URL: <https://doi.org/10.3389/fneur.2021.718423>.
- [41] Uzay E. Emir et al. “Non-invasive quantification of 2-hydroxyglutarate in human gliomas with IDH1 and IDH2 mutations”. In: *Cancer Research* 76.14 (2016), pp. 3870–3879. DOI: 10.1158/0008-5472.CAN-15-1610. URL: <https://doi.org/10.1158/0008-5472.CAN-15-1610>.

## Appendix A

### Individual Fits

The following figures show the acquired spectra with the corresponding fits and residuals.

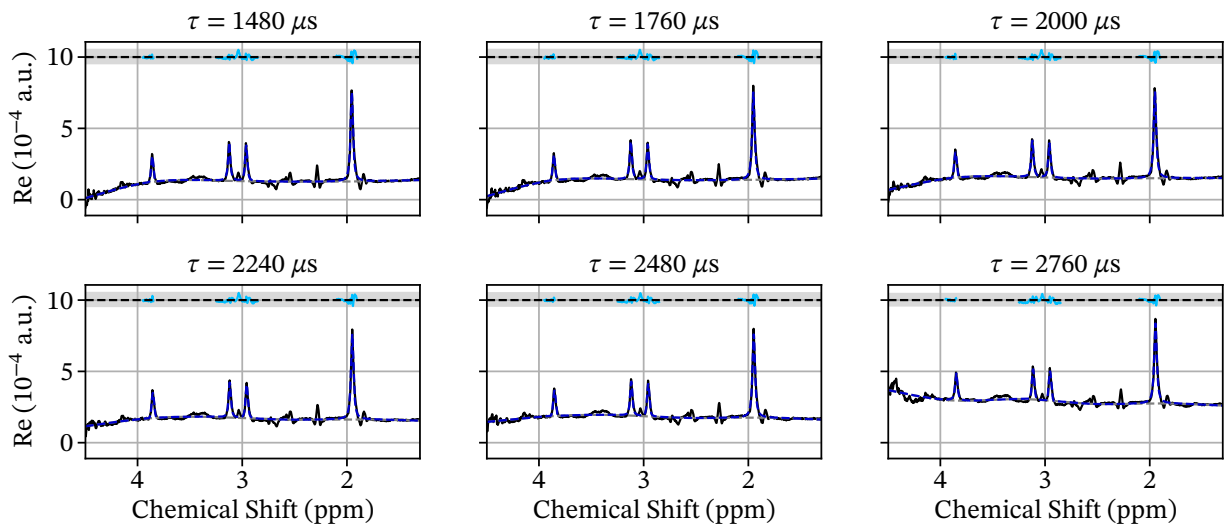


Figure A.1: **CSDE fits:** acquired spectrum (black) with fit (blue), baseline (gray) and residuals (light blue); excitation pulse duration given above.

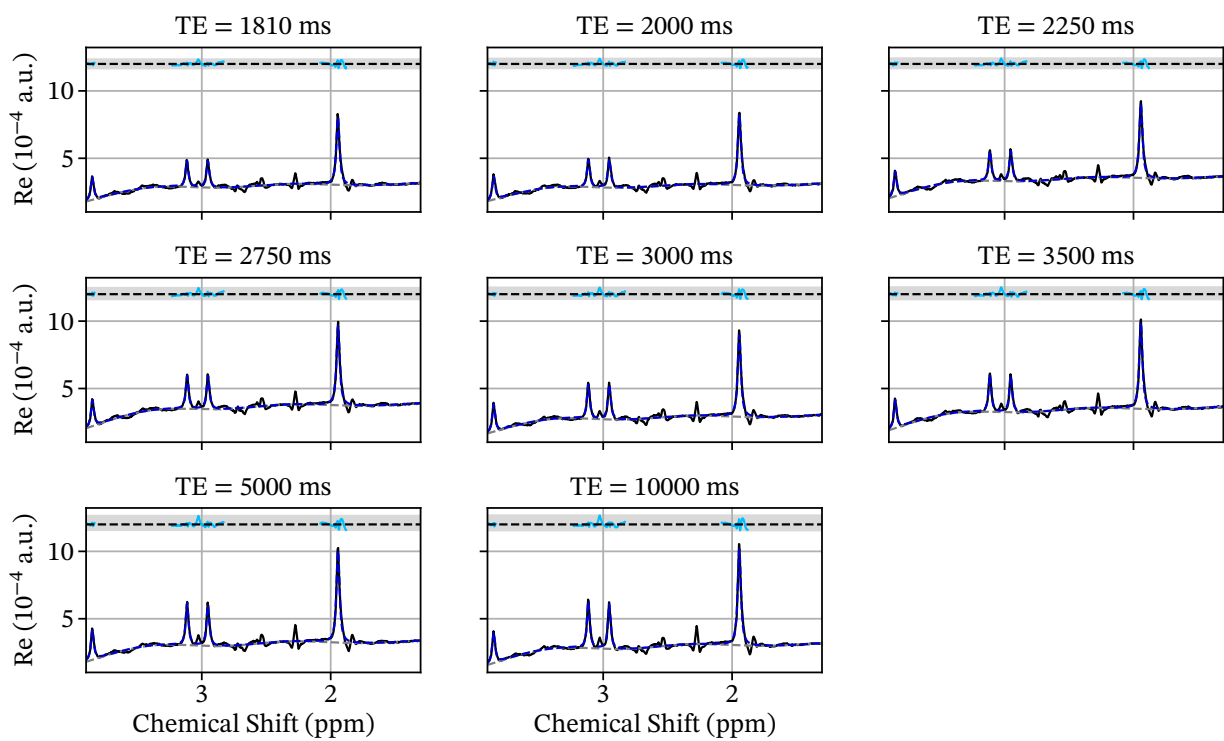


Figure A.2:  **$T_1$  fits in the GABA phantom:** acquired spectrum (black) with fit (blue), baseline (gray) and residuals (light blue); TR given above.

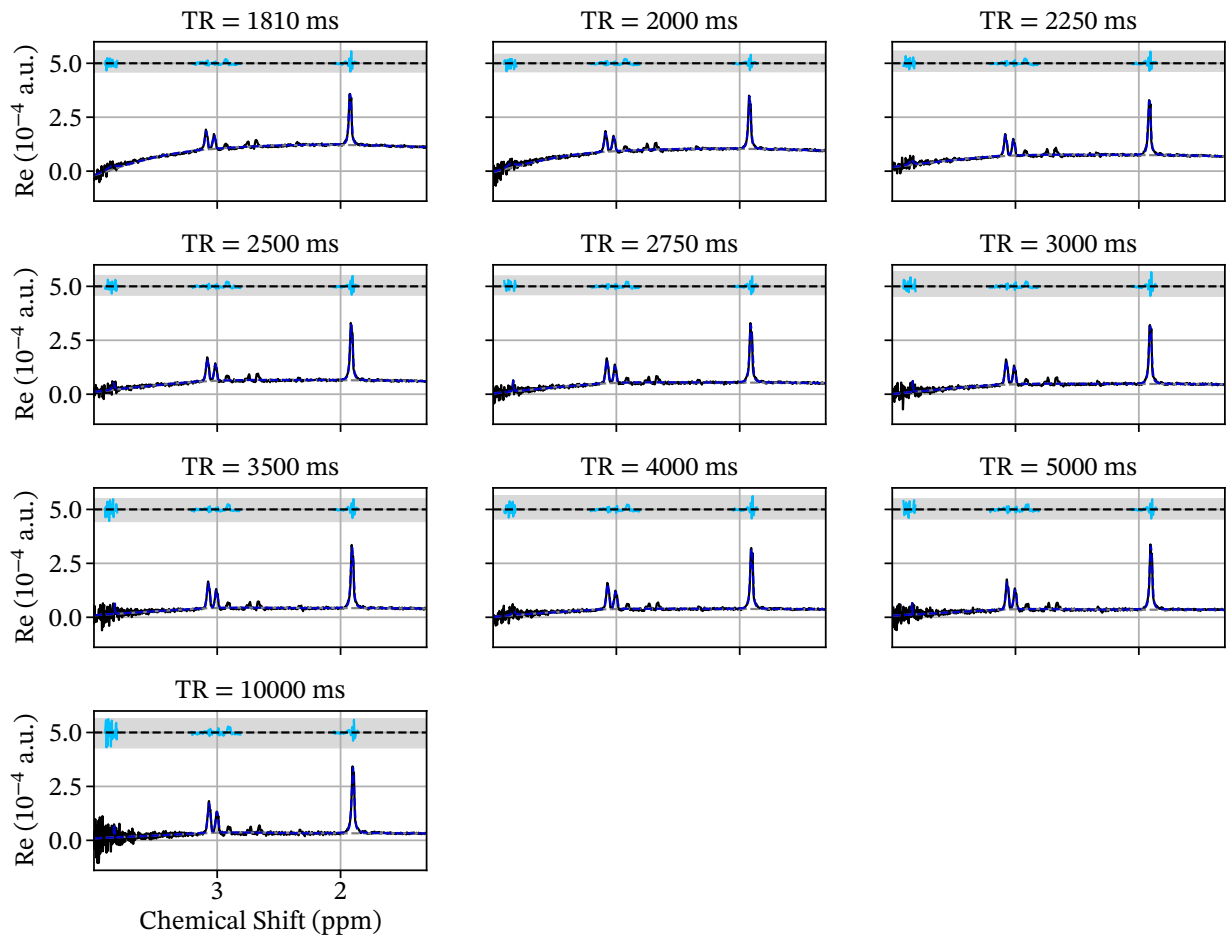


Figure A.3:  **$T_1$  Fits in the 2HG phantom:** Acquired spectrum (black) with fit (blue), baseline (gray) and residuals (light blue); TR given above.

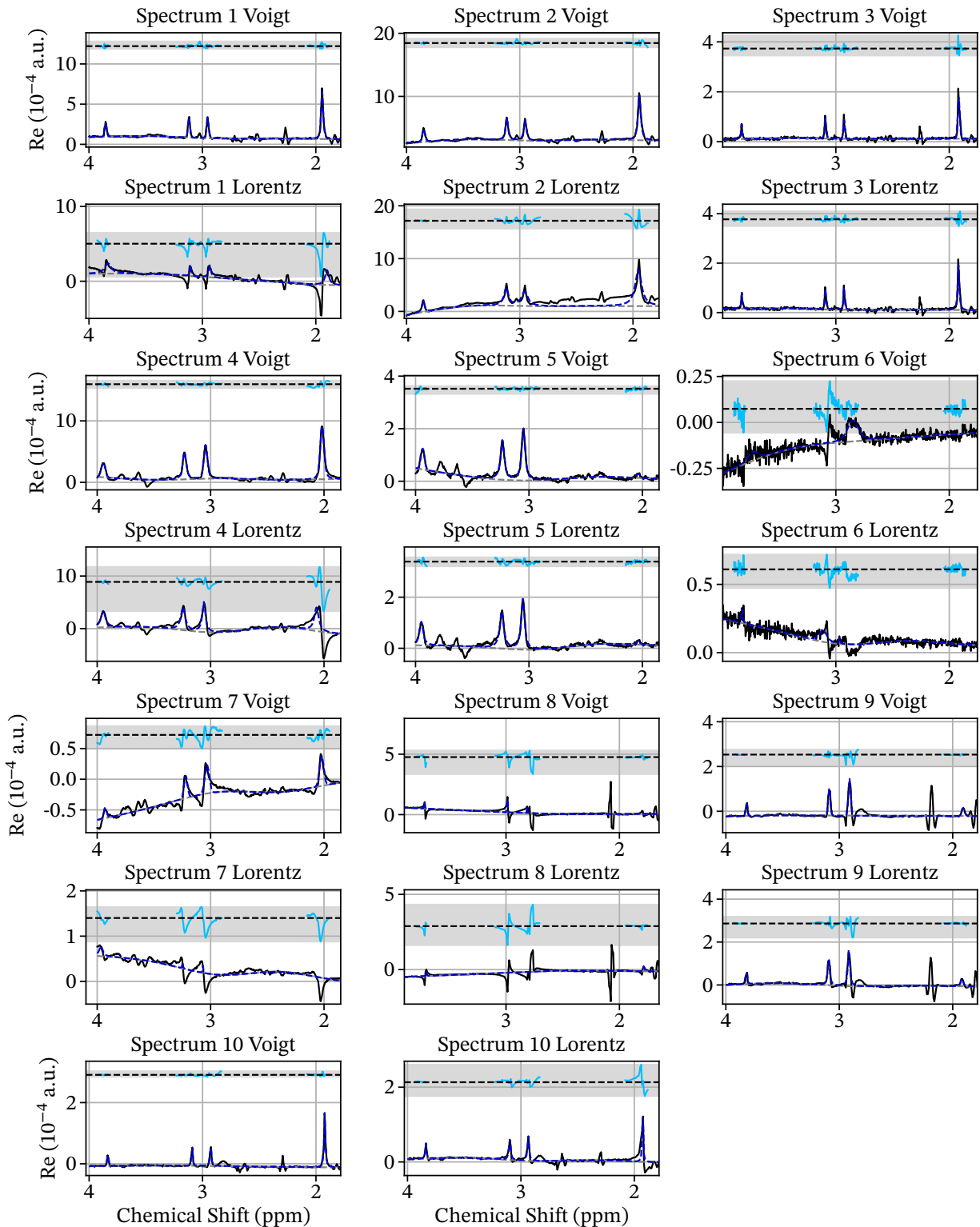
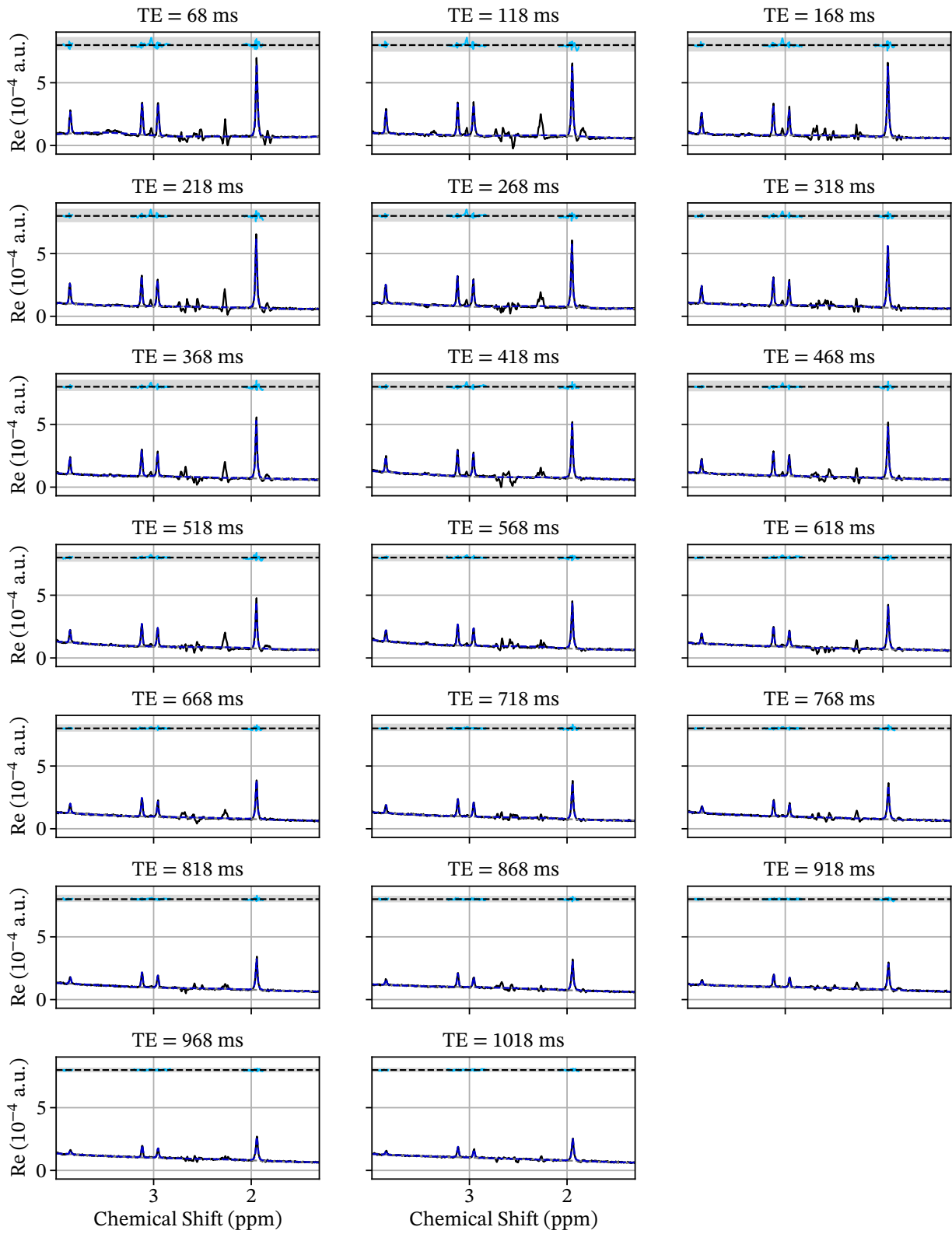
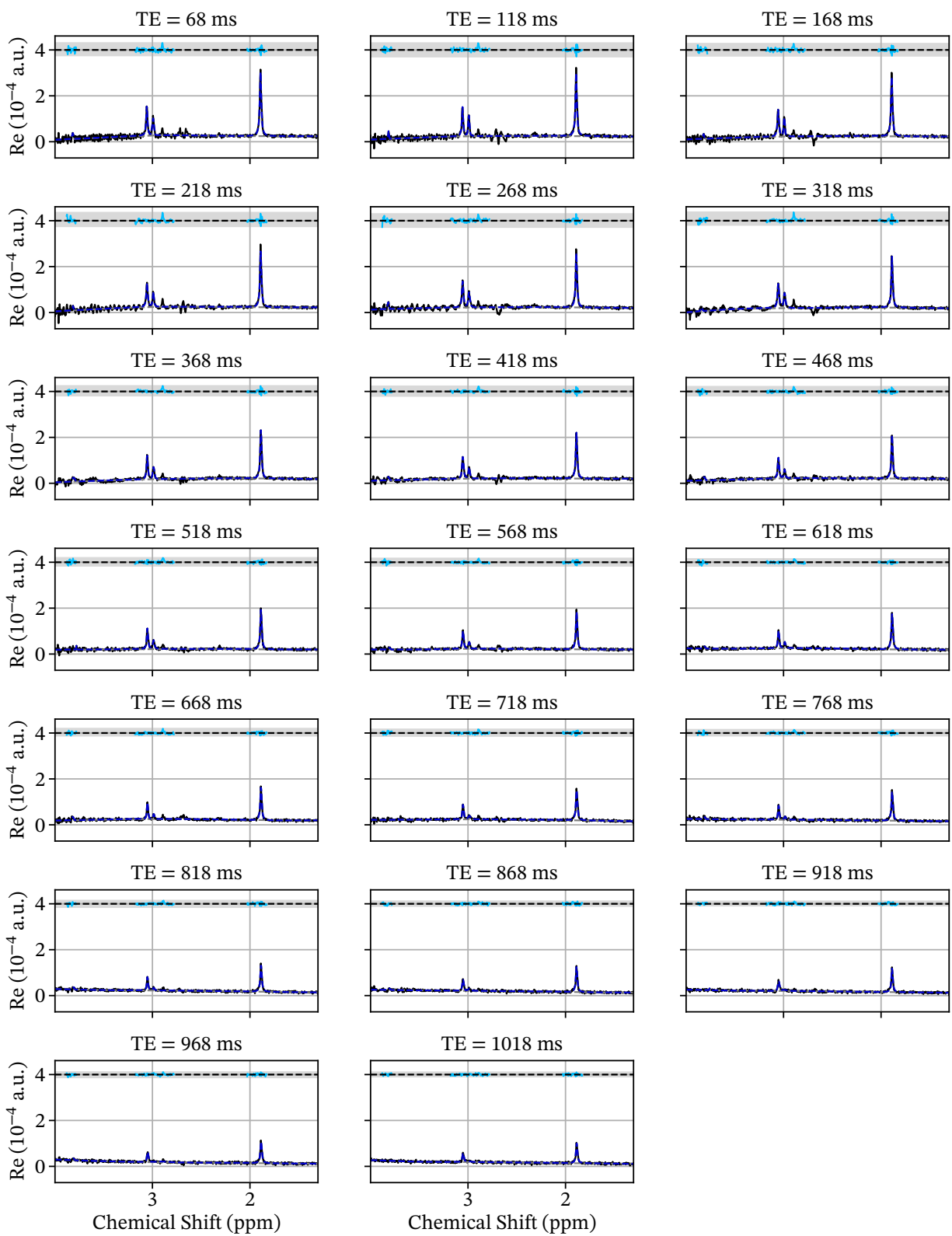


Figure A.4: **Profile comparison fits:** acquired spectrum (black) with fit (blue), baseline (gray) and residuals (light blue); Peak model and index given above.



**Figure A.5:  $T_2$  fits in the GABA phantom:** acquired spectrum (black) with fit (blue), baseline (gray) and residuals (light blue); GABA was ignored in the fit as the transversal relaxation is complicated by j-modulation and therefore  $T_2$  could not be determined; TE given above.



**Figure A.6:  $T_2$  fits in the 2HG phantom:** acquired spectrum (black) with fit (blue), baseline (gray) and residuals (light blue); GABA was ignored in the fit as the transversal relaxation is complicated by J-modulation and therefore  $T_2$  could not be determined; TE given above.

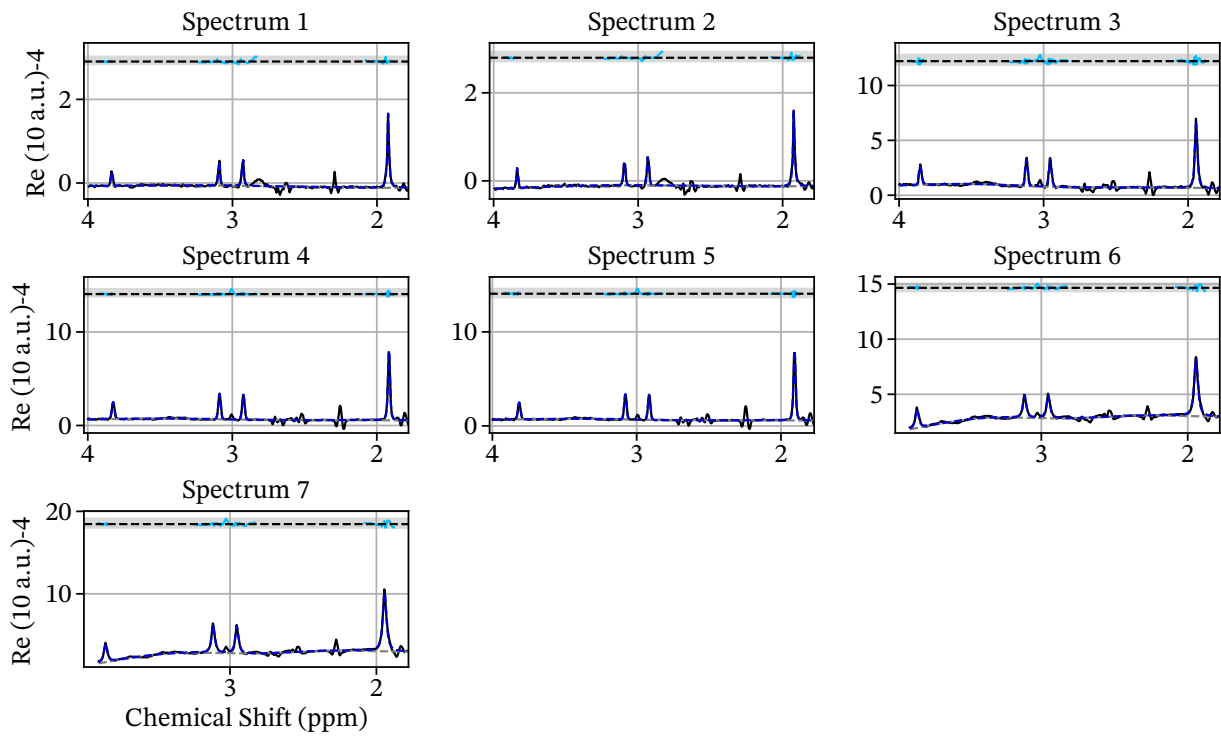


Figure A.7: **SVS fits of NAA, Cr and Cho:** Acquired spectrum (black) with fit (blue), baseline (gray) and residuals (light blue).

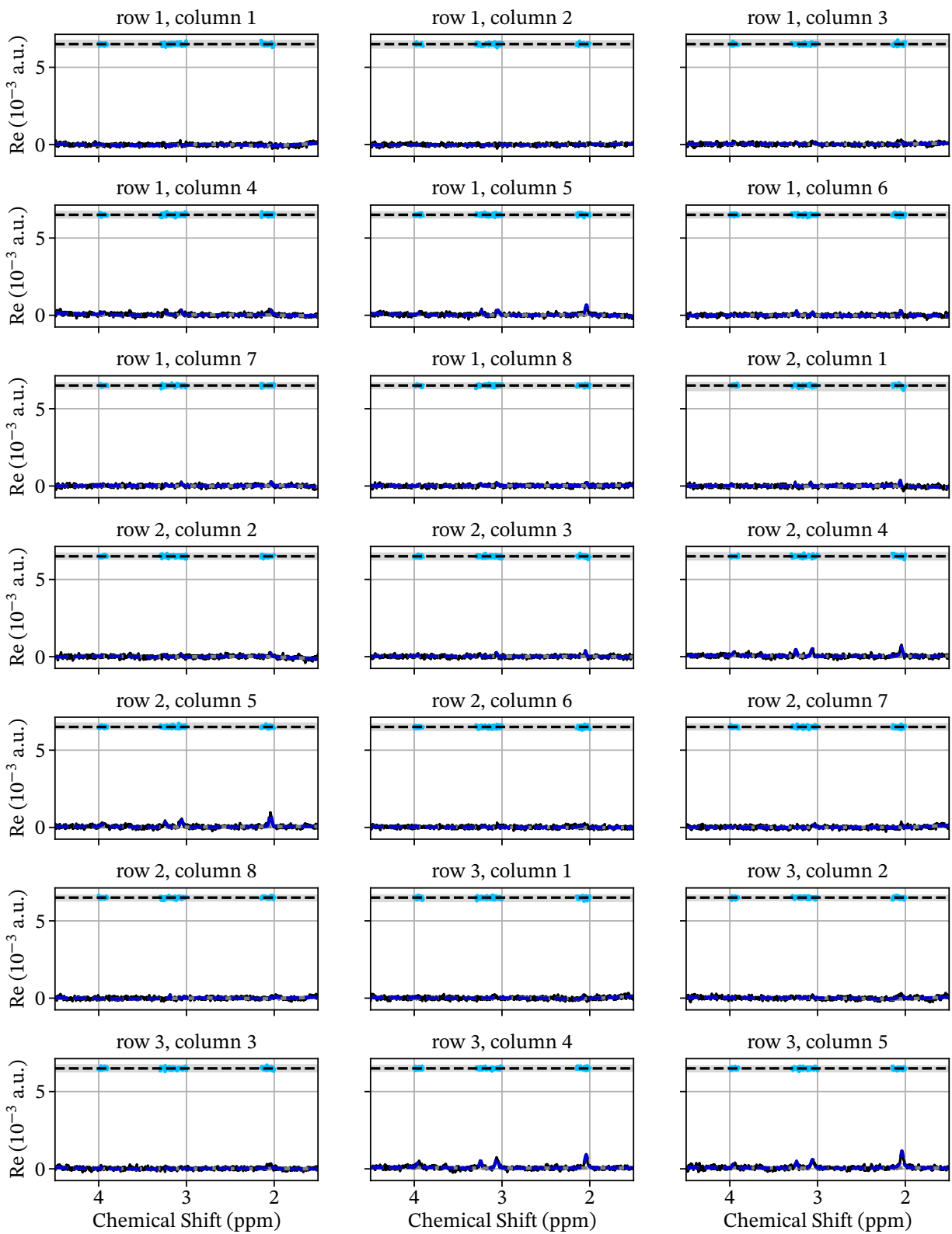


Figure A.8: **CSI fits in vivo:** acquired spectrum (black with fit (blue), baseline (gray) and residuals (light blue); row and column in the scanner output given above.

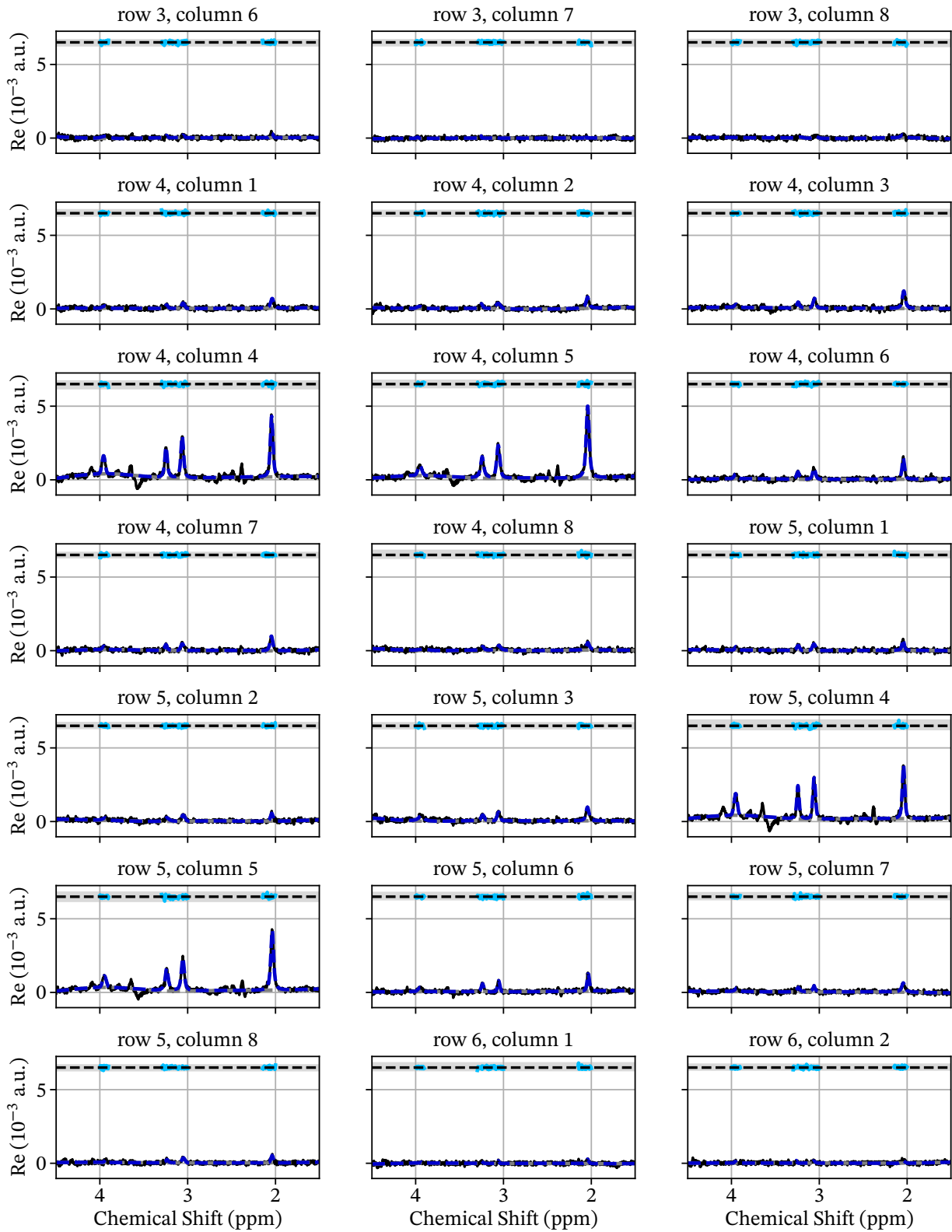


Figure A.8: **CSI fits *in vivo* (continued).**

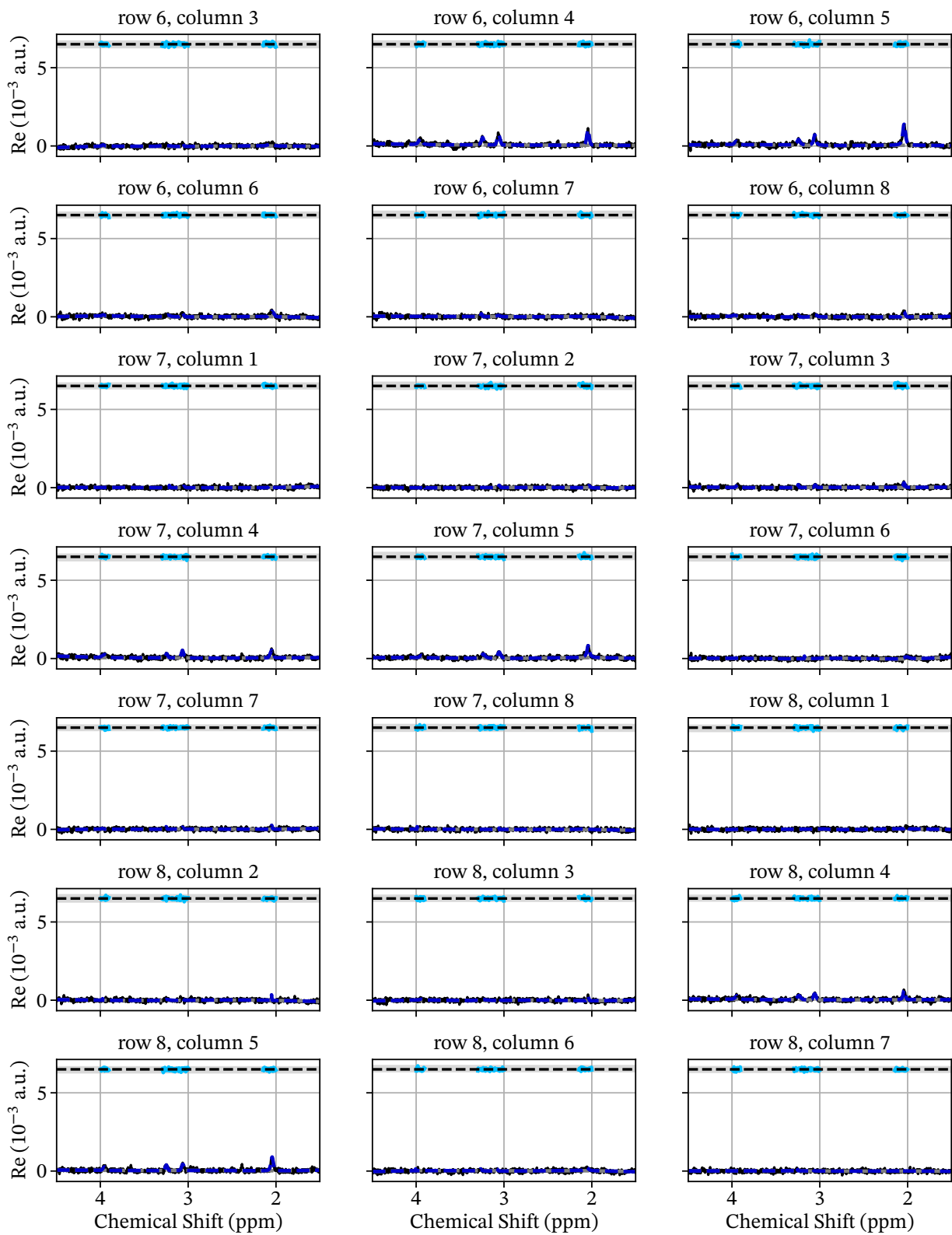


Figure A.8: CSI fits *in vivo* (continued).

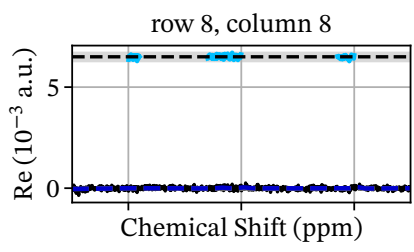


Figure A.8: **CSI fits *in vivo* (continued).**

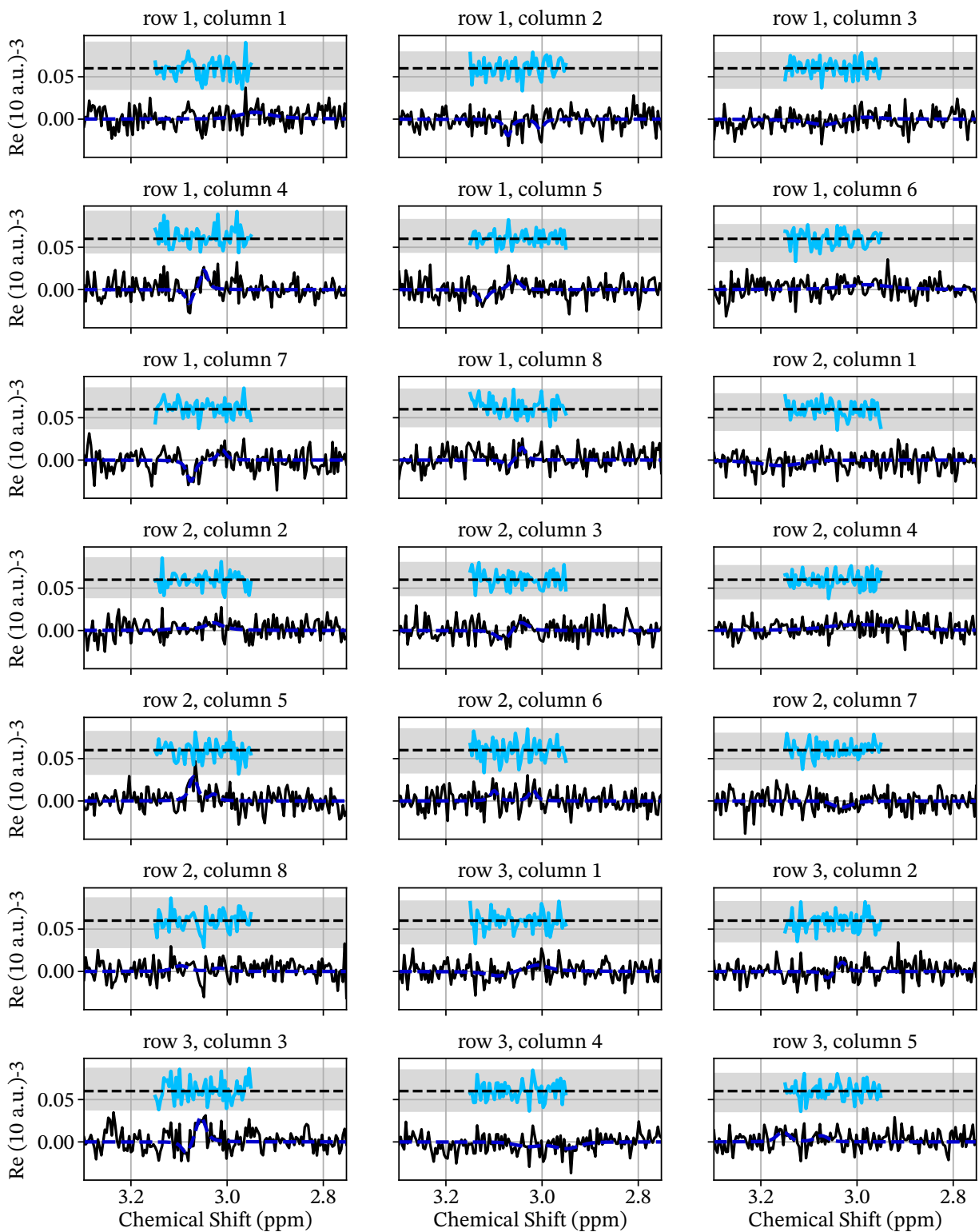


Figure A.9: **GABA CSI fits in vivo:** Acquired spectrum (black with fit (blue), baseline (gray) and residuals (light blue); row and column in the scanner output given above.

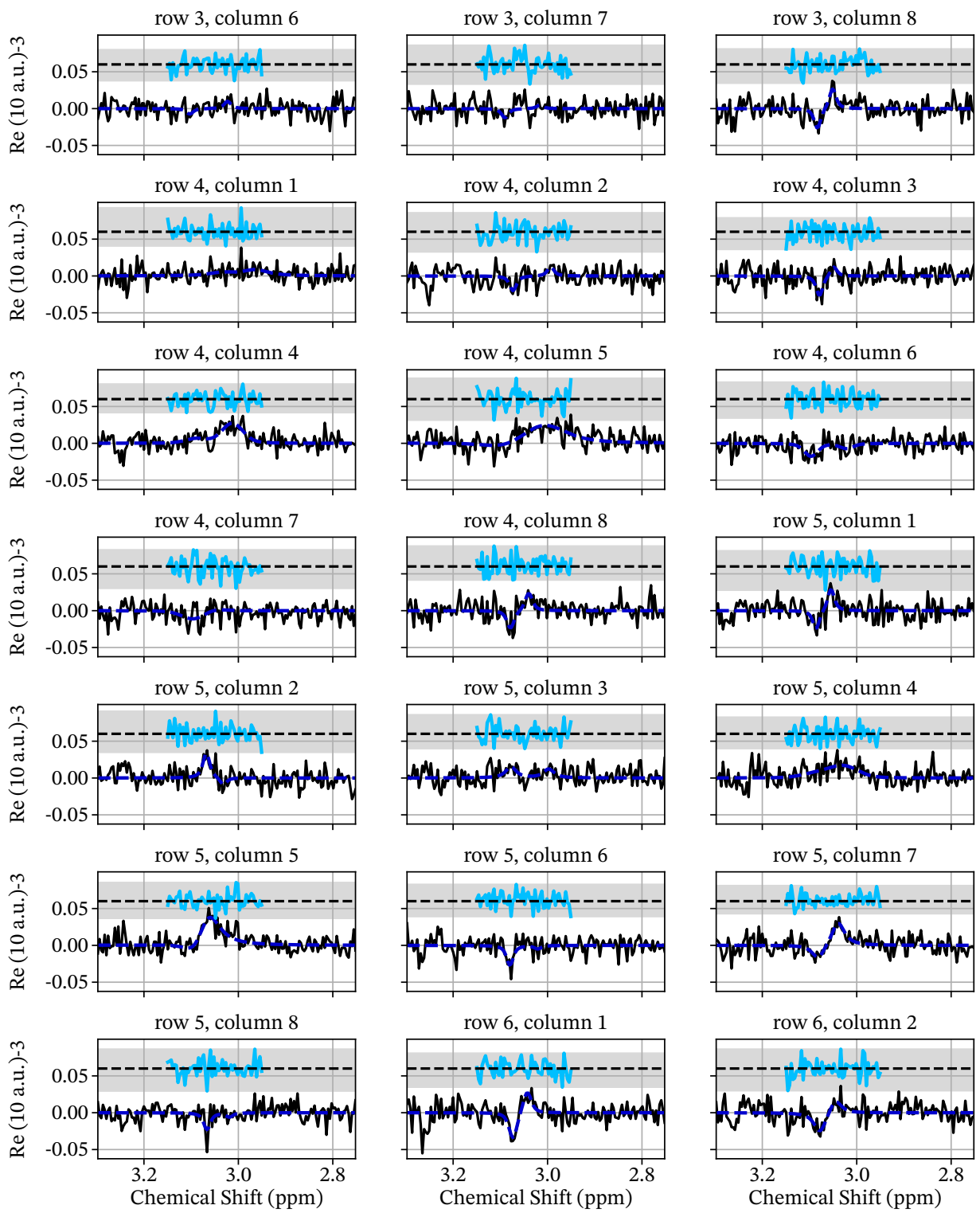


Figure A.9: **GABA CSI fits in vivo (continued).**

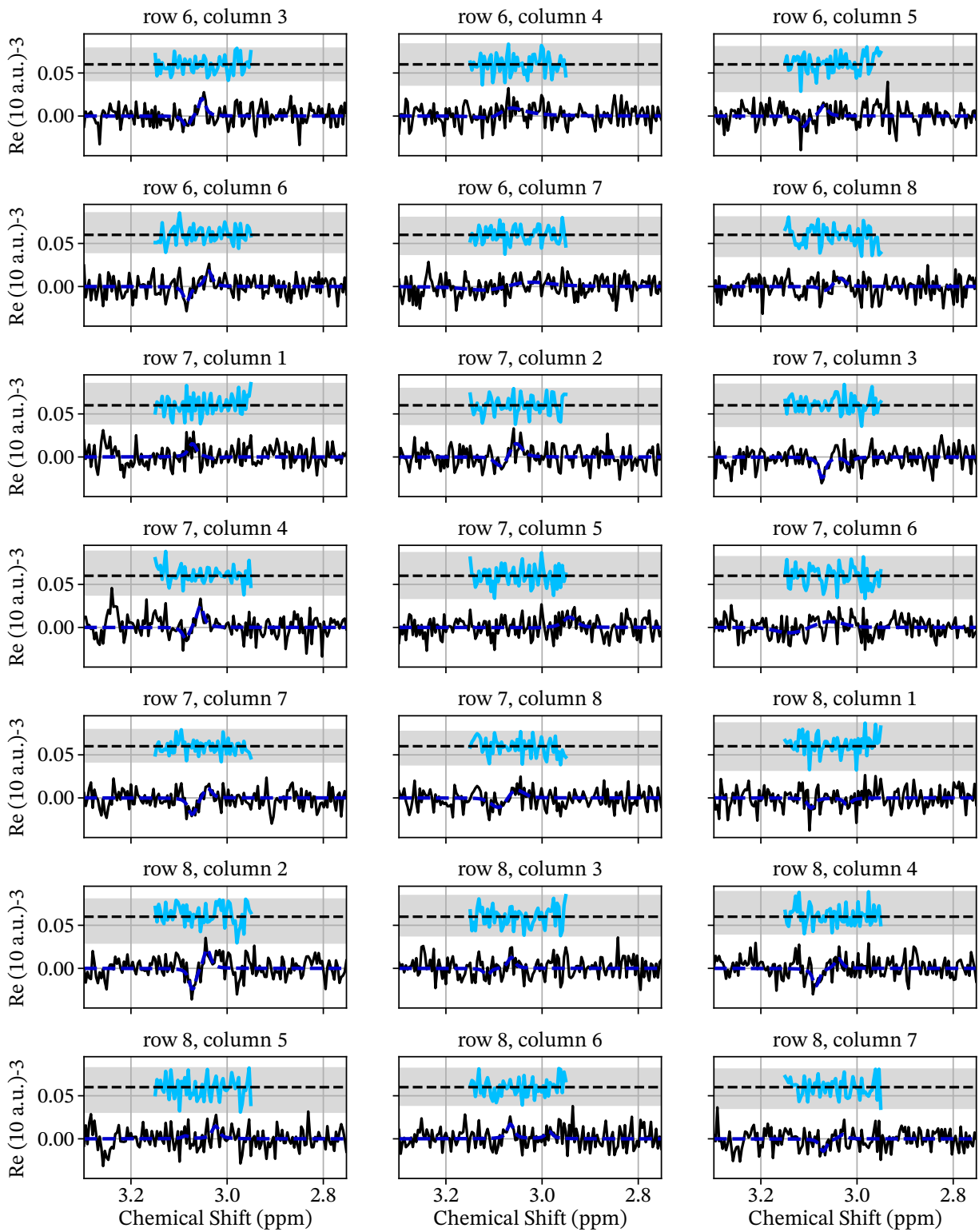


Figure A.9: **GABA CSI fits in vivo (continued).**

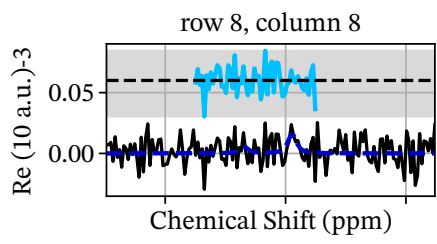


Figure A.9: GABA CSI fits *in vivo* (continued).

# **Declaration of Tools Used**

Besides the literature I cited in the bibliography, I made occasional use of the AI-based language model ChatGPT 5 (OpenAI). Its role was limited to supportive tasks, such as identifying possible literature, refining formulations and assisting with proofreading of grammar, orthography, and punctuation, as well as improving the presentation of plots.

The conception of writing the main text, the selection and evaluation of sources, as well as all scientific arguments, results and conclusions are entirely my own responsibility.

Sequence diagrams were created with the LaTex package `mrseqdia` (a Tikz translation of Mark J.White's MetaPost macros, using trapezoidal pulse notation after T.A. Wilkinson).

## **Bestätigung der Nutzung von künstlicher Intelligenz**

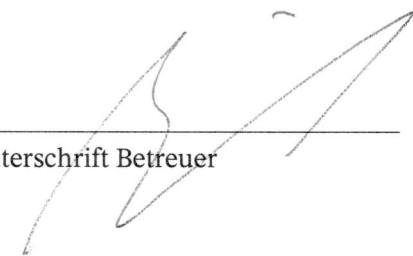
Hiermit bestätige ich, Moritz Zaiss, als Betreuer der Bachelorarbeit von Johanna Link (Matrikelnummer 23003367) mit dem Titel “*Magnetic Resonance Spectroscopy With and Without J-difference Editing*”, dass ich den folgenden Wortlaut unter dem Abschnitt “*Declaration of Tools Used*” in dieser Arbeit gelesen habe und damit einverstanden bin:

Besides the literature I cited in the bibliography, I made occasional use of the AI-based language model ChatGPT 5 (OpenAI). Its role was limited to supportive tasks, such as identifying possible literature, refining formulations and assisting with proofreading of grammar, orthography, and punctuation, as well as improving the presentation of plots.

The conception of writing the main text, the selection and evaluation of sources, as well as all scientific arguments, results and conclusions are entirely my own responsibility.

Erlangen, den 29.9.2025

Unterschrift Betreuer



**Prof. Dr. rer. nat. Moritz Zaiss**

W2-Professor für multimodale Bildgebung in der klin. Forschung  
Universitätsklinikum Erlangen  
Neuroradiologisches Institut  
Henkestrasse 91, 91052 Erlangen  
[Moritz.Zaiss@uk-erlangen.de](mailto:Moritz.Zaiss@uk-erlangen.de)

# Eigenständigkeitserklärung

Hiermit versichere ich, Johanna Evelyn Link, Matrikelnummer 23003367, die vorgelegte Arbeit selbstständig und ohne unzulässige Hilfe Dritter sowie ohne Hinzuziehung nicht offengelegter und insbesondere nicht zugelassener Hilfsmittel angefertigt zu haben. Die Arbeit hat in gleicher oder ähnlicher Form noch keiner anderen Prüfungsbehörde vorgelegen und wurde auch von keiner anderen Prüfungsbehörde bereits als Teil einer Prüfung angenommen.

Die Stellen der Arbeit, die andere Quellen im Wortlaut oder dem Sinn nach entnommen wurden, sind durch Angaben der Herkunft deutlich gemacht. Dies gilt auch für Zeichnungen, Skizzen, bildliche Darstellungen sowie für Quellen aus dem Internet.

Mir ist insbesondere bewusst, dass die Nutzung künstlicher Intelligenz verboten ist, sofern diese nicht ausdrücklich als Hilfsmittel von den Prüfenden zugelassen wurde. Dies gilt insbesondere für solche Programme, die anstelle meiner Person die Aufgabestellung der Prüfung bzw. Teile derselben bearbeiten könnten, zum Beispiel Chatbots (wie ChatGPT) und andere hierzu geeignete Methoden. Des Weiteren ist mir bekannt, dass die gemeinsame Bearbeitung der Aufgabenstellung mit anderen Personen oder mithilfe sozialer oder anderer Medien eine unzulässige Hilfe Dritter im o.g. Sinne darstellt, wenn nicht ausdrücklich Gruppenarbeit vorgesehen ist. Das Korrekturlesen der Arbeit durch Dritte mit dem Ziel, sprachliche Mängel zu beheben, ist zulässig.

Verstöße gegen die o.g. Regeln sind als Täuschung bzw. Täuschungsversuch zu qualifizieren und führen zu einer Bewertung der Prüfung mit "nicht bestanden". Bei mehrfach oder auch besonders drastischen Regelverstößen sind weiterführende Sanktionen durch den Prüfungsausschuss möglich.

---

Ort, Datum

---

Eigenhändige Unterschrift

# Danksagung

Zunächst möchte ich mich ganz herzlich bei meiner Betreuerin Dr. Angelika Mennecke bedanken. Sie hatte stets ein offenes Ohr für meine Fragen, hat meine Arbeit mit großem Engagement begleitet und das Korrekturlesen übernommen.

Meinem offiziellen Betreuer Prof. Dr. Moritz Zaiss danke ich für die Betreuung sowie die hilfreichen Antworten auf meine Fragen.

Besonders danke ich Simon Köppel, der mir bei der Implementierung der Parallelisierung geholfen und meine Arbeit ebenfalls kritisch gegengelesen hat.

Ein großer Dank gilt auch dem Personal der Neuroradiologie des Uniklinikums Erlangen, insbesondere Ludwig Singer, der unermüdlich versucht hat, Versuchspersonen für die 2HG-Messungen zu gewinnen.

Darüber hinaus möchte ich mich bei den freiwilligen Versuchspersonen bedanken, die diese Arbeit überhaupt erst möglich gemacht haben.